An Investigation of Rheo-NMR Techniques to Improve the Capture of Residual Dipolar Couplings

Ben Munro

A thesis submitted in partial fulfillment of the

requirement for the award of the Degree of

Master of Science

in Chemistry

INSTITUTE OF FUNDAMENTAL SCIENCES

MASSEY UNIVERSITY

Palmerston North, New Zealand

2015

For Scarlett & Delilah Munro

Abstract

Residual Dipolar Couplings (RDCs) are an increasingly important structural restraint that can be used to help generate high quality structural models of proteins by Nuclear Magnetic Resonance (NMR) methods. They are captured with the aid of an alignment medium that imposes some anisotropy to the protein's tumbling. Current methods for the capture of multiple sets of these couplings are tedious, expensive, and do not always result in unique sets being captured. This thesis set out to investigate whether multiple RDC sets could be captured from a single sample by controllably shearing the liquid crystal alignment medium used.

Initial experiments focused on the ability to controllably realign a number of different nematic phase liquid crystals. These experiments found that controlling the director angle of the liquid crystal is possible, and that a number of stable alignments can be achieved through the application of different shear stresses.

The application of RDCs to small molecules is a very young field that is still developing and finding potential uses. In this thesis a small molecule system of (+)-isopinocampheol ((+)-IPC) was investigated with RDCs being collected from this molecule within a liquid crystal phase with the director at a number of different orientations relative to the external magnetic field. The fitting of these captured RDCs to a structural model of the (+)-IPC was not able to generate a high quality fit for any of the RDC sets collected, leading to some puzzling results. It is hypothesized that inhomogeneity of the alignment phase was responsible for these difficulties.

As the application of RDCs is so heavily dominated by protein structure studies, a small protein was investigated. The protein of choice, ubiquitin, has been heavily investigated in the past, and is often used as a demonstrator protein for new NMR techniques. This work presents several RDC data sets measured from ubiquitin which were successfully captured at a variety of different director orientations of the alignment media. These RDC sets were all successfully fitted to a previously known X-Ray crystallographic structure of ubiquitin, and unique alignment tensors for each RDC data set were extracted.

Finally, structure calculations were carried out incorporating these captured ubiquitin RDC data sets with the goal of investigating how the variation in the ensembles of structures generated was modified. The results from these calculations showed that the addition of RDC data (over and above NOE constraints) to the simulated annealing process results in ensembles of higher quality structures being obtained. However, the addition of multiple sets of RDC data (collected with different director alignments) did not appear to cause any further improvement.

Acknowledgments

I would like to thank the following people and organizations for their contributions to this project:

First of all I could not go past acknowledging the help and support that both of my supervisors, Dr. Pat Edwards, and Dr. Bill (M.A.K.) Williams have provided throughout the course of this project.

The Ministry of Business, Innovation, and Employment provided funding for this investigation through the grant: New NMR Technologies.

Dr. Elena Harjes for her discussions and help around the application of RDC data to structure calculations.

Dr. Robin Dykstra & Magritek for providing equipment and discussion surrounding the control of both shear motors.

Terry Southern, Geoff Hunter & Beta Solutions for their support and development of the second generation shear motor used in this project.

Dr. Petrik Galvosas, Tim Brox, Dr. Brad Douglas, & the Victoria University Magnetic Resonance group for invaluable discussions about the effect of shear on liquid crystal systems, as well as development of the second generation shear cell and help with developing the control mechanisms for the shear motors.

Dr. Jane Allison for her explanations of the processes involved in extracting an alignment tensor from our RDC data.

David Nixon for providing computationally calculated structural models of (+)-IPC.

IFS Faculty and Admin staff for their support and help.

My children, Scarlett & Delilah for always providing a worthwhile distraction.

And finally my partner Rebecca Fox, for her unwavering support, for putting up with my late nights working, and her immense help throughout my chemotherapy and writing of this thesis.

Contents

List of Figures

List of Tables

Nomenclature

(+)-IPC (1S, 2S, 3S, 5R)-(+)-Isopinocampheol

1D One Dimension

2D Two Dimensions

3D Three Dimensions

B_{eff} Effective Magnetic Field

CD Circular Dichroism

COSY Correlation Spectroscopy

CTAB Cetyltrimethylammonium Bromide

D Dipolar Coupling

FID Free Induction Decay

HSQC Hetronuclear Single Quantum Coherence

I Spin Quantum Number

INEPT Insensitive Nuclei Enhanced by Polarization Transfer

IPAP In-phase Anti-phase Heteronuclear Single Quantum Correlation Spectroscopy

K Degrees Kelvin

k Boltzmann Constant

MAS Magic Angle Spinning

MHz Megahertz

MW Molecular Weight

NMR Nuclear Magnetic Resonance

NOE nuclear Overhauser effect

NOESY Nuclear Overhauser Effect Spectroscopy

PBLG Poly-γ-Benzyl-L-Glutamate

PEEK Polyether Ethyl Ketone

ppm Parts per Million

P_α Population of alpha spins

P_β Population of beta spins

Q Quality factor

RDC Residual Dipolar Coupling

RF Radio Frequency

RMSD Root-Mean-Square Deviation

S_{xx} Saupe Tensor xx component

S_{yy} Saupe Tensor yy component

S_{zz} Saupe Tensor zz component

TMS Tetramethylsilane

T_2	Transverse relaxation time
β-LG	β-Lactoglobulin
ΔE	Change in Energy
δ	Chemical Shift
γ	Gyromagnetic Ratio
$\hat{A}$	Alignment Tensor
$\hat{P}$	Probability Tensor
$\hat{S}$	Saupe Tensor
$\hbar$	Reduced Planck Constant
μ_0	Vacuum Permeability Constant
ν_{ref}	Resonant Frequency of a Reference Nuclei
$\nu_{spectrometer}$	Operating Frequency of Spectrometer
ν_o	Lamor Precession Frequency
ω_0	Zero Quantum Transition
ω_1	Single Quantum Transition
ω_2	Double Quantum Transition
$\vec{r}$	Internuclear Unit Vector
^1J	One Bond J-Coupling
^3J	Three Bond J-Coupling
$\mathbf{B}_0$	Spectrometer's Magnetic Field Vector

M	Net Magnetization Vector
h	Planck's Constant
m	Magnetic Quantum Number
t_1	Spin-lattice relaxation time

1. Introduction

Proteins are an undeniably important class of large biomolecules which play vital roles throughout living systems, from the structural roles of keratin, collagen, and elastin, to the more intricate enzymes which help to drive the many processes of life. While many of the functional structural properties of proteinaceous material can be observed on the macroscale, understanding the structures of the individual protein molecules can allow dissection of the chemical and physical processes that contribute to the protein's function. The increased understanding that molecular level structural information can provide opens the door to allow targeted interactions with molecules for specific processes (e.g. a targeted drug).

A protein's structure itself can be divided into four different levels; primary, secondary, tertiary, and quaternary, each of which describes a different aspect of the 3D structure (Figure 1.1).

The primary structure is the most basic level and only describes the amino acid sequence. It does not provide any direct information about the 3D structure of the protein [1]. The secondary structure begins to describe how the molecule folds into highly regular 3D structures, with the commonly seen local structural motifs such as alpha helices, and beta sheets being formed. The secondary structure involves hydrogen bond formation between the amino groups and carbonyl units of each amino acid [2, 3]. Tertiary structure explains the overall shape of the single protein molecule and demonstrates how the secondary structures relate to each other and are driven by the hydrophobic interactions between the amino

acids. The final level of structure is quaternary which involves how multiple polypeptide chains come together to form the larger full protein complex.

There are a variety of methods available to determine the structure of a protein, each with their own advantages and drawbacks. The most commonly utilized method is X-ray crystallography, a technique which can give an accurate structural model developed by measuring the electron density in 3D space, allowing the coordinates of the atoms to be inferred [4, 5]. One draw-back of X-ray crystallography is the need for the protein to be in a crystalline state, a requirement that can be difficult to overcome with the inherent lability of such large molecules or multi-domain structures [6]. Consideration also needs to be given to the differences between the solution and solid state structures, which often results in some differences between the structures obtained using the solution or crystalline forms.

Circular dichroism (CD) is another analytical technique that can give information about the secondary structures that are present in the sample [7]. While this is useful, the applications of CD is largely qualitative about the structures that are present and does not provide information about the location or order of the secondary structures present in the protein.

The second most commonly used technique to gain a full structural model is Nuclear Magnetic Resonance (NMR) spectroscopy. As will be discussed in detail in Chapter 2, NMR relies on the small magnetic fields that nuclei can possess interacting with a strong external magnetic field. Monitoring this interaction and the phenomena related to this interaction, can allow information about the magnetic environment that each nucleus is experiencing to be extracted, allowing the 3D structure of the molecule to begin to be pieced together. In addition to the generation of structural models, NMR can also be used to gather information about the dynamic motions of the polypeptide chain that occur due to thermal energy. As NMR is only concerned with the nuclei of a molecule, a sample can be

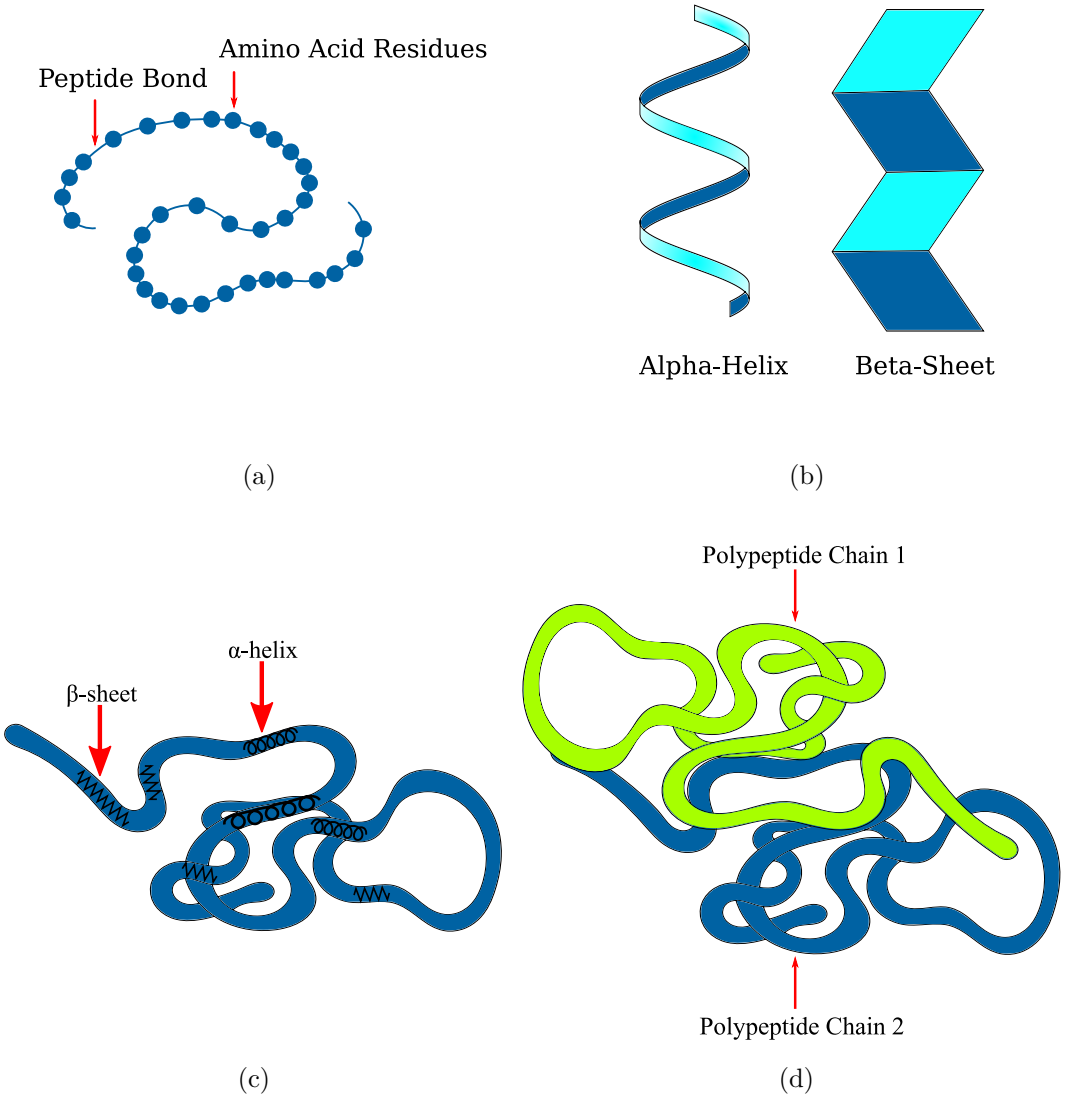

Figure 1.1.: **Cartoon representation of the different levels of a protein's structure:** General representations of the levels present in a protein. a) The primary structure of a protein. The primary structure only describes the sequence in which the amino acids are arranged. b) The secondary structure of a protein. The secondary structure describes local trends in 3D structure, such as alpha-helices or beta-sheets. c) Tertiary structure of a protein. The tertiary structure describes how the secondary structures present in the protein are related to each other in 3D space. For a protein which consists of only one polypeptide chain the tertiary structure is the full complete structure. d) Quaternary structure of a protein. The quaternary structure of a protein describes how multiple polypeptide chains are arranged together to for the full 3D structure of some proteins.

prepared as a solid or solution. Most modern high-resolution NMR experiments use solution samples, and can be applied to a variety of nuclei, most commonly ^{1}H, ^{13}C, and ^{15}N . As proteins are large molecules comprised largely of carbon, hydrogen, and nitrogen, it can be seen how NMR techniques could be applied to developing an understanding of their structure.

NMR has long been used to study protein structures [8], with the development of Fourier transform spectroscopy, superconducting magnets and computationally controlled equipment spurring the development of the field further towards the generation of the first full 3D model of a protein from NMR data in 1985 [9]. This first structure, as with the vast majority that have come after it, were built heavily around the use of NOEs (nuclear Overhauser effect) to generate the 3D structure. NOEs are a through space interaction which can allow the detection of nuclei which are close through space yet may be separated by many chemical bonds, and will be explained in further detail in Section 2.2. The use of NOEs is not always desirable though due to the time consuming nature of their capture and analysis, as well as problems that can be encountered when there is a lack of close contact points between areas of a target molecule, which can occur with largely linear proteins or nucleic acids. Recently there has been a push towards the development and application of Residual Dipolar Couplings (RDCs) in order to provide long range 3D structural information. RDCs provide information about the orientation of a given bond vector relative to the magnetic field, $\mathbf{B_0}$.

RDCs are not observed in an isotropic solution due to the rapid tumbling of all molecules. In order to observe these couplings a small amount of anisotropy needs to be introduced to the sample. Current methods for generating this anisotropy revolve around the use of either a liquid crystalline alignment medium, or a strained gel. These methods only allow for a single RDC data set to be extracted from each alignment medium (or sample), which leaves a substantial amount of ambiguity with the possible orientational outcomes of each bond vector, as is

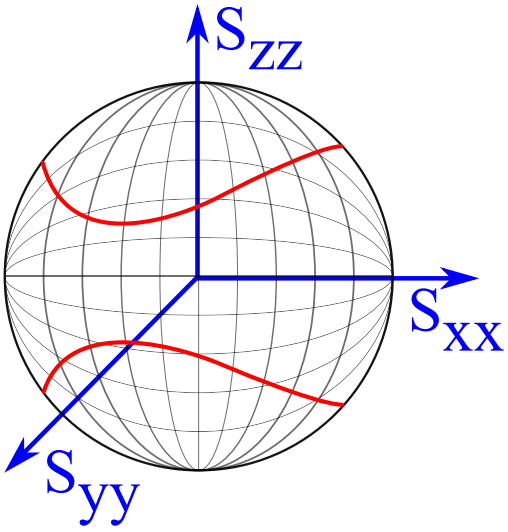

Figure 1.2.: **Possible orientations from a single alignment:** The possible orientations of a bond vector based on the capture of RDCs from a single alignment media. The two red circles represent the two possible paths that a given single bond vector can be aligned along. S_{zz}, S_{xx}, and S_{yy} are the components of the diagonalized Saupe tensor.

displayed in Figure 1.2. The current solution to this ambiguity is to capture multiple sets of RDCs in different alignment media, resulting in the situation displayed in Figure 1.3. Unfortunately the use of multiple alignment media is a time consuming and expensive task that may not always result in "independent alignments" being generated. For this investigation an "independent alignment" has been classed as a set of collected RDCs which are not simply scaled by a common factor. The purpose of the work described in this thesis is to determine if the application of rheo-NMR techniques would allow for the capture of multiple independent alignments to be obtained from a single sample.

Rheo-NMR is an experimental technique which uses NMR tools to monitor the reaction of matter, usually fluids, to the application of shear forces. One state of matter that is commonly studied using rheo-NMR is liquid crystals. These studies have found that it is possible to alter the alignment of a nematic liquid crystal phase's director by applying a sufficiently large shear force. The alignment of the director relative to the magnetic field can be detected through the use of

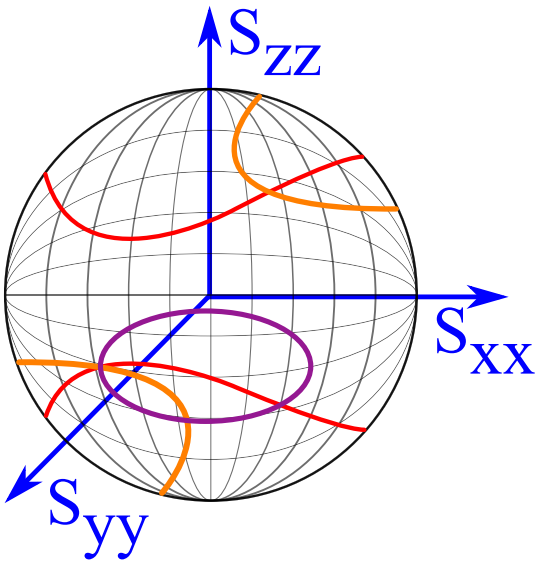

Figure 1.3.: **Possible orientations obtained from multiple alignment media:** The possible orientations of a bond vector measured in multiple alignment media. The possible orientations in each of the multiple alignment media are represented by the different coloured circles. The final orientation of the single bond vector is the intersection of the multiple alignment mediums, on both sides of the sphere. S_{zz}, S_{xx}, and S_{yy} are the components of the diagonalized Saupe tensor of the sample.

^{2}H NMR, where due to the non-spherical charge distribution of a nucleus with a spin quantum number $I > \frac{1}{2}$ (^{2}H: $I = 1$) the orientation of the liquid crystal can be monitored through the quadrupolar splitting exhibited by the ^{2}H nuclei present in the solvent [10, 11, 12].

This thesis sets out to investigate the viability of combining this ability to reorient a liquid crystalline phase with the capture of RDCs in a uniquely oriented liquid crystalline phase. It is hoped that the ability to tune the alignment of a host liquid crystalline material, and have the tuned alignment passed in part along to the target molecule, will allow multiple unique alignments. These multiple unique alignments could then allow for multiple RDC data sets to be obtained from a single sample with minimal experimental effort. If multiple RDC data sets are able to be captured these will be checked for consistency with prior known structures of the target molecules. This project will be completed in a number of steps, firstly a series of investigations into multiple different liquid crystalline media which may be suitable for RDC measurement of small molecules or proteins will be carried out. These investigations will determine if each alignment medium is able to be reoriented through the application of a shear force, as well as what effect, if any, the use of differing shear profiles has on a liquid crystal's director (e.g. steady shear vs. pulsed shear). Once control of the liquid crystalline materials has been established, the second step of this project will involve the capture of RDCs from a target small molecule. As the NMR spectra that can be obtained from a small molecule will be well resolved, this will act as a simplified proxy for a larger molecule, such as a protein. The third step of this project will be the final application of the previously investigated techniques on to a target protein, and will endeavor to determine if multiple independent RDC data sets can be obtained from a single sample through the application of controlled shear forces. Fitting these data sets to a known structure of the target protein will allow the quality of the RDC sets obtained under shear to be determined.

More detailed analysis of the RDC sets obtained for a given molecule may allow improvements to be made to the structural model, giving a better understanding of the true structure of the molecule in solution.

2. Theory

2.1. NMR Spectroscopy

2.1.1. Principles of NMR

2.1.1.1. The Classical Model

The nuclei for which NMR spectra can be measured have an intrinsic angular momentum called *spin* [13]. This property, combined with the nuclei's positive charge creates a small magnetic field. When this small nuclear magnetic field is exposed to a strong external magnetic field ($\mathbf{B_0}$) each spinning nucleus attempts to align its magnetic moment with the external field. This results in a torque being exerted on the nuclear spins causing a circular motion called precession at a frequency ν_o, similar to a traditional spinning top rotating due to the earth's gravity [14, 15]. The precession frequency is proportional to the strength of the external magnetic field strength ($\mathbf{B_0}$) and the gyromagnetic ratio (γ) of the nucleus, which is a constant defining the ratio of its spin angular momentum to its magnetic dipole moment.

$$v_o = \gamma B_0 / 2\pi \tag{2.1}$$

Magnetic field strengths of typical commercial NMR spectrometers cause the rate of precession to be in the radio frequency range (megahertz), and can be measured by applying a short radio signal pulse before monitoring the oscillating

current that is induced by the oscillating magnetization in the sample. The detected current is known as the *Free Induction Decay* (FID), and contains the precession frequencies of all nuclei in the sample. This measurement can allow nuclei in different magnetic environments to be detected and characterized.

2.1.1.2. A Quantum Model

The advantage of the classical model is its simplicity. However, it is unable to account for many important NMR phenomena, for which the more thorough, but more complex quantum model is required.

The intrinsic nuclear spin is described by a quantum number value (I) which can take values of 0, $\frac{1}{2}$, 1.... For a nucleus to be NMR active I must be >0. Such nuclei have an odd number of protons and/or neutrons. The higher the spin quantum number the more possible orientations (spin states) the nuclear spin can adopt in the external magnetic field. The most useful nuclei for NMR have $I = \frac{1}{2}$ e.g. ^{1}H, ^{13}C, ^{15}N, ^{19}F, ^{31}P which have two possible spin states (as determined through the simple formula $(2(I)+1)$). These spins can point 'up' (α) or 'down' (β) in the external magnetic field and are characterized by a magnetic quantum number, m (which can hold values of $m = -I, -I+1$, ..., 0, ..., $I-1$, I). When these spin $\frac{1}{2}$ nuclei are at thermal equilibrium in the absence of an external magnetic field exactly one half of the nuclei will be in each state at any given time.

When an external magnetic field is introduced the distribution becomes unequal with slightly above 50% of the nuclei being in the α state (aligned with $\mathbf{B_0}$). This distribution occurs due to the α state having a lower energy than the β state (for a spin with a positive γ). The energy of each spin is found to be related to the specific nuclei and the magnetic field strength and can be found through:

$$E = -\frac{h\gamma B_0 m}{2\pi} \tag{2.2}$$

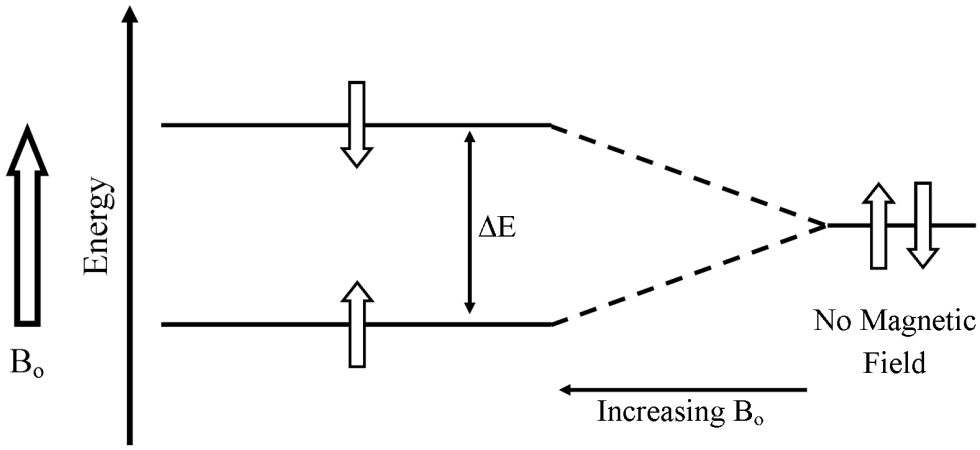

Figure 2.1.: **Quantum energy levels of a spin $\frac{1}{2}$ nucleus in a magnetic field:** The two quantum energy levels formed when a spin$\frac{1}{2}$ nucleus is placed into a strong external magnetic field

As with other types of spectroscopy, only specific transitions are allowed and can take place. With NMR the allowed transitions are those which change the magnetic quantum number by a value of ± 1.

When energy is applied which matches the energy gap (ΔE) between the α and β levels one of the lower energy α spins can be promoted to the higher energy state.

$$\Delta E = h v_o = h\gamma B_0 / 2\pi \tag{2.3}$$

This is similar to the equation seen in the classical model situation, with v_o now being the resonant frequency instead of the precession frequency along with h being Planck's constant.

2.1.1.3. Experimental NMR spectroscopy

The ratio of populations of each spin state is found via a Boltzmann distribution:

$$P_\beta / P_\alpha = e^{-\Delta E / kT} \tag{2.4}$$

where P_α and P_β are the proportion of the total population of 'up' or 'down' spins respectively, ΔE is the energy gap between the 'up' and 'down' spins, k is the Boltzmann constant and T is the temperature in Kelvin (K).

As the 'up' spin will always have a slight population excess, there will be a net magnetic field along the direction of the external magnetic field, $\boldsymbol{B_0}$, which defines the z-axis of the laboratory frame. This net magnetic field is represented by the *net magnetization vector* $\boldsymbol{M}$.

In order to measure the specific resonant frequencies of the nuclei modern NMR spectrometers emit a high power radio frequency (RF) pulse, which if applied for an appropriate duration (typically a few μs) will rotate the net magnetization vector from the z-axis into the x-y plane. Once the magnetization has been rotated, $\boldsymbol{M}$ will precess in a cone as it returns towards the equilibrium position parallel with the z-axis. The precession occurs at the resonant frequency of the given nuclei, generating an oscillating voltage in the receiver coil of the NMR spectrometer's probehead. This occurs for all nuclei of a given type (e.g. all ^{1}H nuclei or all ^{13}C nuclei) simultaneously, subject to the bandwidth of the RF pulse being sufficiently wide. Since, in a typical sample the (e.g. ^{1}H) nuclei rarely experience exactly the same external magnetic field (due to phenomena such as the chemical shift – see below) the resulting signal is therefore usually a sum of sine waves, known as a *free induction decay* (FID). The NMR signal captured as the FID is one of signal intensity vs. time. This can be converted to the standard NMR spectrum of intensity vs. frequency via a Fourier transform.

2.2. Small molecule NMR

The 1D proton (^{1}H) NMR experiment is the most commonly used NMR experiment by synthetic chemists. The utility of this experiment relies on the differences between the magnetic environment that each type of ^{1}H nucleus of a given

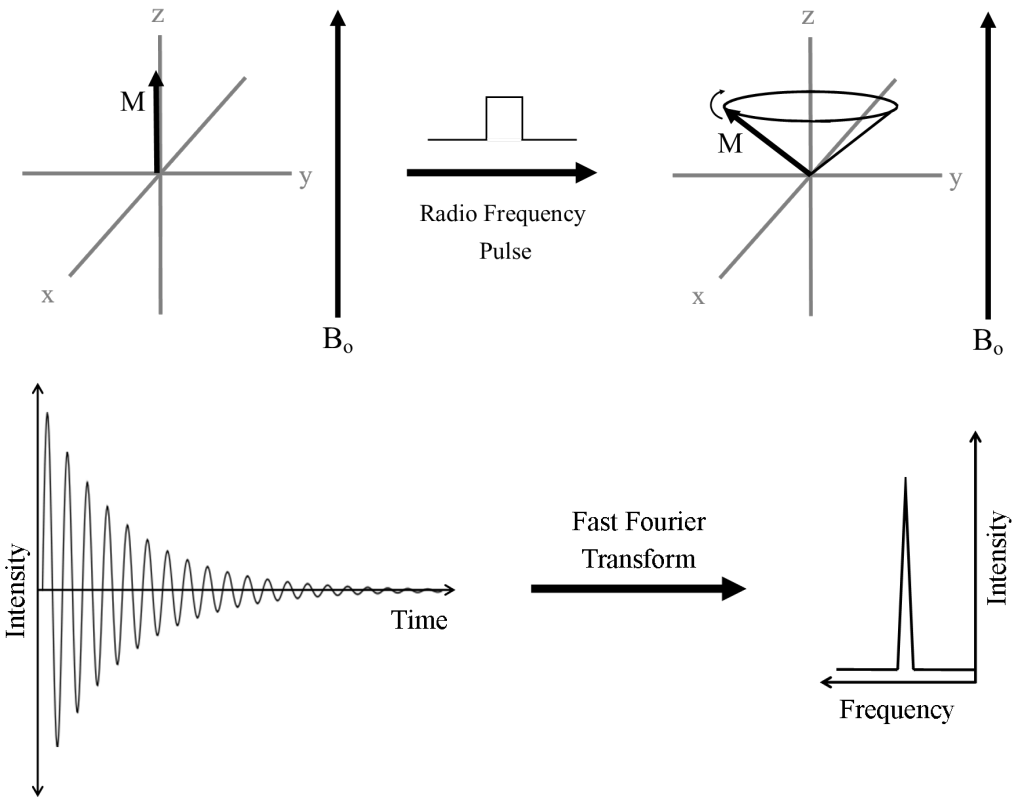

Figure 2.2.: **Vector model explanation of NMR spectroscopy:** Net magnetization vector aligned along the +z-axis of the laboratory frame parallel to the external magnetic field $\mathbf{B_0}$ before being rotated into the x-y plane by a high powered radio frequency pulse. The FID that is captured can be plotted as intensity vs. time. This is then converted into a frequency vs. intensity plot by using a fast Fourier transform.

molecule experience. The small changes in the magnetic field observed by each nucleus are caused by the movement of electrons creating small magnetic fields that add to or oppose that of the spectrometer. This effect is called shielding and changes the magnetic field sensed by each nucleus with a concomitant effect on the energy levels and absorption frequencies compared to those of a "bare" nucleus. These small variations in frequency are on the order of parts per million and are commonly referred to as chemical shifts. The differences in chemical shift of each nuclei in a molecule can allow detailed information about a molecule's structure to be determined. The chemical shift is measured in parts per million (ppm) and is referenced against the fundamental resonant frequency of the specific nuclear isotope being studied at a given external magnetic field strength e.g. 500 MHz is the resonant frequency of a lone ^{1}H nuclei in a 11.7 tesla magnetic field. Chemical shift (δ) of a given nucleus within a molecule is found to follow the following scale:

$$\delta = \frac{(\nu - \nu_{ref})}{\nu(spectrometer)} \tag{2.5}$$

where ν is the resonant frequency of the target nuclei, ν_{ref} is the frequency of the reference nuclei, both in Hz (e.g. the ^{1}H signal of tetramethylsilane, TMS), and $\nu(spectrometer)$ is the operating frequency of the spectrometer, in MHz. This scale removes the difference in signal frequencies that would occur if the same compound was measured in spectrometers with different operating frequencies.

Through understanding of how different chemical bonding motifs will effect the chemical shift of each nuclei it is possible to start to piece together a structure, at least for very simple molecules. To determine the structure of more complex molecules additional NMR phenomena need to be utilized.

J-coupling concerns the interaction between nuclear spins propagated by the bonding electrons of a molecule [21]. For the case of two J-coupled protons, H_a & H_b, in a fragment H_a– C_a– C_b– H_b , the magnetic field that the full population of H_a observes will be split into two distinct groups based on the population of

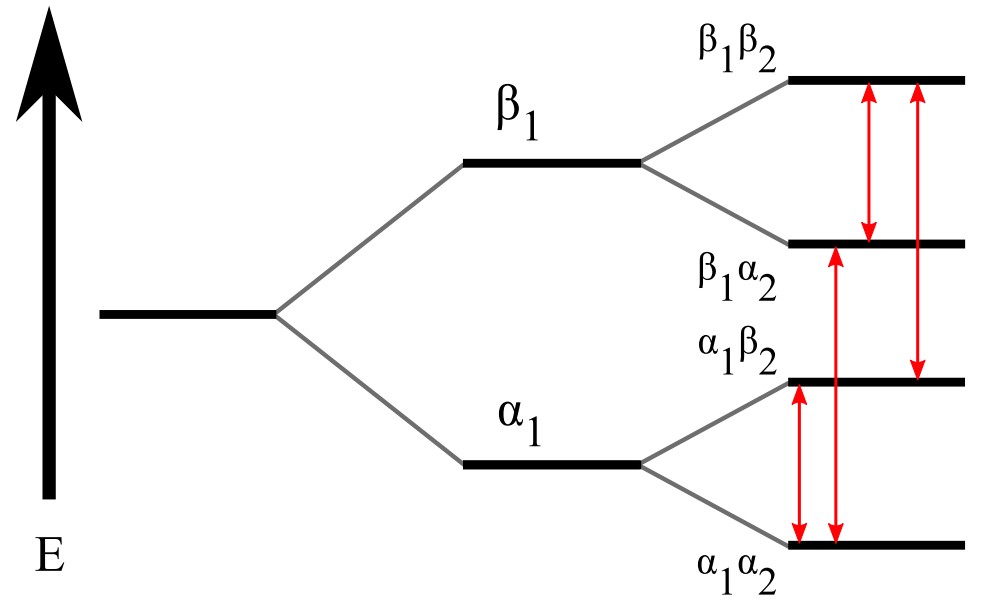

(a)

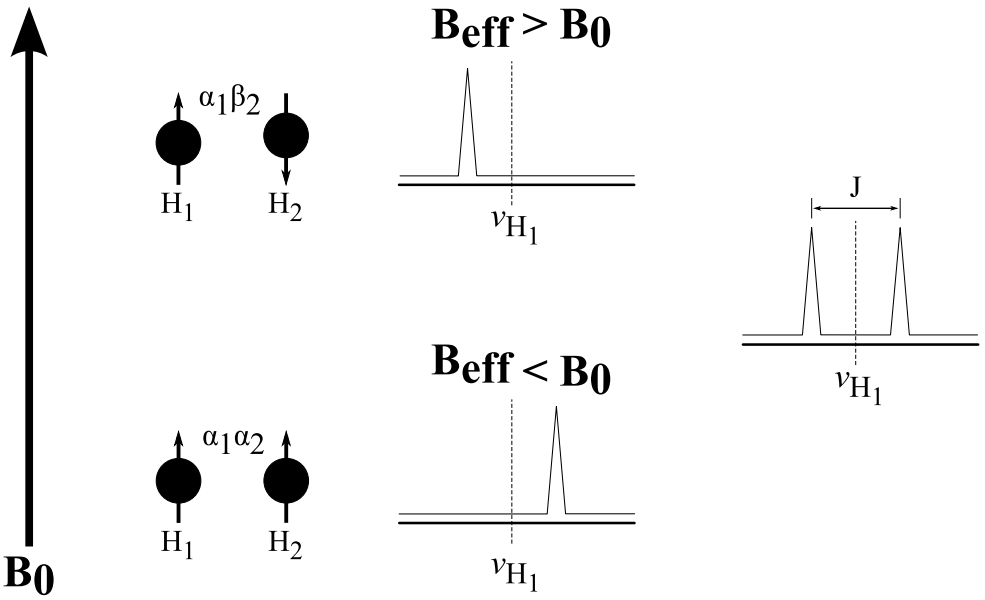

(b)

Figure 2.3.: **Origin of Spin-Spin splitting for a two proton system:** a) Energy level diagram for two coupled protons H_1, and H_2.The four allowed single quantum transitions are demonstrated in red, where a single nuclei 'flips' between the α and β states. This series of transitions results in four peaks being present for the two protons in pairs shifted up and down field from the nominal v_{H_1} frequency. b) Spin-Spin splitting for two protons attached to two adjacent carbon nuclei and the spectra generated from each situation. The spectrum displayed shows only one of the two doublets that is formed. There will be a second doublet formed at v_{H_2} with the same J value arising from the H_2 nuclei being in a fixed orientation and the H_1 nuclei transitioning between the α and β states [16, 17, 18, 19, 20].

H_b having ∼50% with an 'up' spin and ∼50% having a 'down' spin. These two possible spins for H_b will either increase, or decrease the magnetic field that H_a observes splitting the signal of H_a into two equal peaks as is demonstrated in Figure 2.3b. When increasing numbers of neighboring equally coupled protons are present the number of possible up and down configurations of these "passive" nuclei increase leading to the signal of the coupled nucleus to be split into $n + 1$ peaks, where n is the number of neighboring protons. The intensity of each peak in the resulting multiplet can be determined via *Pascal's triangle:*

singlet					1						(*no neighbors*)
doublet				1		1					(*one neighbor*)
triplet			1		2		1				(*two neighbors*)
quartet		1		3		3		1			(*three neighbors*)
quintet	1		4		6		4		1		(*four neighbors*)
sextet	1	5		10		10		5		1	(*five neighbors*)

The peak separation generated by this spin-spin splitting is known as the J-coupling. It is sensitive to parameters such as bond lengths, electronegativity of substituents and perhaps most importantly dihedral angles between protons attached to adjacent carbon atoms as is demonstrated in Figure 2.4.

The nuclear Overhauser effect (NOE) is another important feature of NMR for aiding in the determination of molecular structure and stereochemistry [26, 27, 28, 29]. This effect is a through-space interaction between two nuclei which allows the detection of nuclei that are close in space yet which may be separated by many chemical bonds.

The magnetic dipolar interaction that occurs when a proton is close through space to another nucleus (with spin > 0) is normally completely averaged to zero in solution state NMR systems by the rapid tumbling of the molecules. These

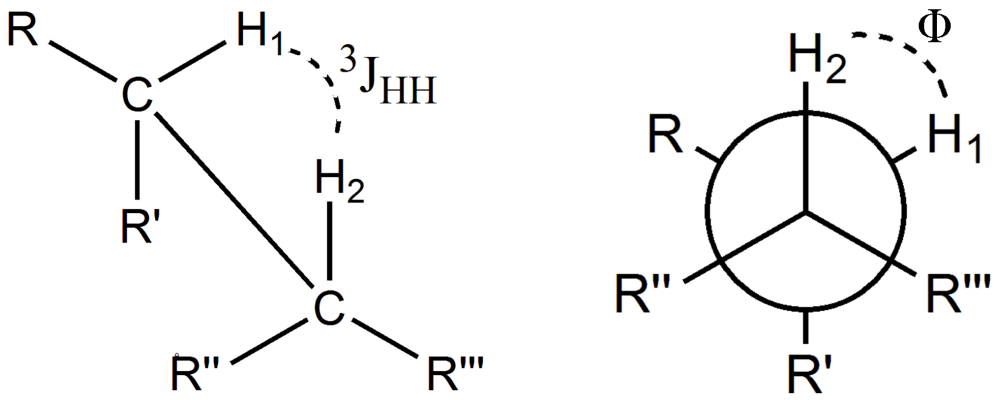

$$^3J_{HH}(\Phi) = A\cos^2\Phi + B\cos\Phi + C$$

Figure 2.4.: **The application of the Karplus equation:** $^3J_{HH}$ coupling between two protons bonded to adjacent carbons allows the torsional angle (θ) to be calculated via the empirical Karplus equation in which A, B, and C are empirically derived constants. This provides more information about the 3D structure of a molecule [22, 23, 24, 25].

dipole dipole interactions result in the relaxation processes that are shown in Figure 2.5 for a two nuclei system of AX. Under normal conditions each of the demonstrated spin states will have nearly equal populations, however the $\alpha\alpha$ population will have a slight population excess of Δ, while the $\beta\beta$ population will have a deficit of $-\Delta$.

The application of decoupling pulses at the frequency specific to X transitions seen in Figure 2.5 will result in the populations of the $\alpha\alpha$ and $\alpha\beta$ states becoming equal, as well as the $\beta\alpha$ and $\beta\beta$ states. This irradiated state is not stable and will begin to decay back to the ground equilibrium state through one of the possible transitions in Figure 2.5. The pathway that the decay takes place through is important and monitoring of which pathway is used is how NOEs are detected.

In a small molecule system it is common for the ω_2 relaxation to be the most efficient ($\omega_2 : \omega_1 : \omega_0 = 12 : 3 : 2$). This process results in both the A and X nuclei that are in the $\beta\beta$ state relaxing back to the $\alpha\alpha$ state. This results in an increase in the population of the α spin state of nuclei A and as such an increase in the NMR signal. This is referred to as a *positive NOE*. It is also possible to

observe a *negative NOE* which results from the ω_0 relaxation process being the most dominant in the system, and the promotion of some of the of the α spin of the A nuclei being promoted to the β state, and therefore a decrease in the NMR signal observed. This *negative NOE* results in a decrease in the observed signal of the A nuclei in the NMR spectrum and is most commonly seen in larger molecule systems such as proteins and biomolecules. As these relaxation effects are both driven through dipole dipole effects they are through space effects, the distance between pairs of nuclei becomes very important. The dipole dipole interaction decay rapidly with a $\frac{1}{r^6}$ distance dependence[30, 31].

NOEs are often measured via a NOESY spectrum, which is a two dimensional experiment with ^{1}H in both dimensions with cross peaks appearing where two ^{1}H nuclei are typically within 5 Å from each other (with the intensity having the $\frac{1}{r^6}$ distance dependence)[32].

After hydrogen the most commonly studied element used for NMR is carbon. Unfortunately the most common natural isotope of carbon, ^{12}C, is not NMR active (I = 0). However ^{13}C which has a natural abundance of ≈1.1% is NMR active (I = $\frac{1}{2}$)[33][34]. This low natural abundance combined with a smaller γ decreases the sensitivity of ^{13}C compared to that of ^{1}H. However it is still an important nucleus to study for organic molecule structure determination. The standard one dimensional experiments that are used on ^{1}H nuclei can also be applied to a ^{13}C nuclei with some modifications. J-coupling between two ^{13}C nuclei is not seen in ^{13}C spectra at natural abundance due to the very low probability of finding two ^{13}C nuclei next to each other. The relatively large couplings ($\sim 130 - -270\ Hz$ for $^1J_{CH}$) between ^{13}C and ^{1}H nuclei is usually removed by using broadband decoupling. Broadband decoupling removes all couplings that would be present by rapidly flipping each ^{1}H nucleus with a continuous train of low powered radio frequency pulses. This rapid flipping of each ^{1}H spin causes only the average spin (zero) to be seen by each ^{13}C nucleus. Another method which will remove the

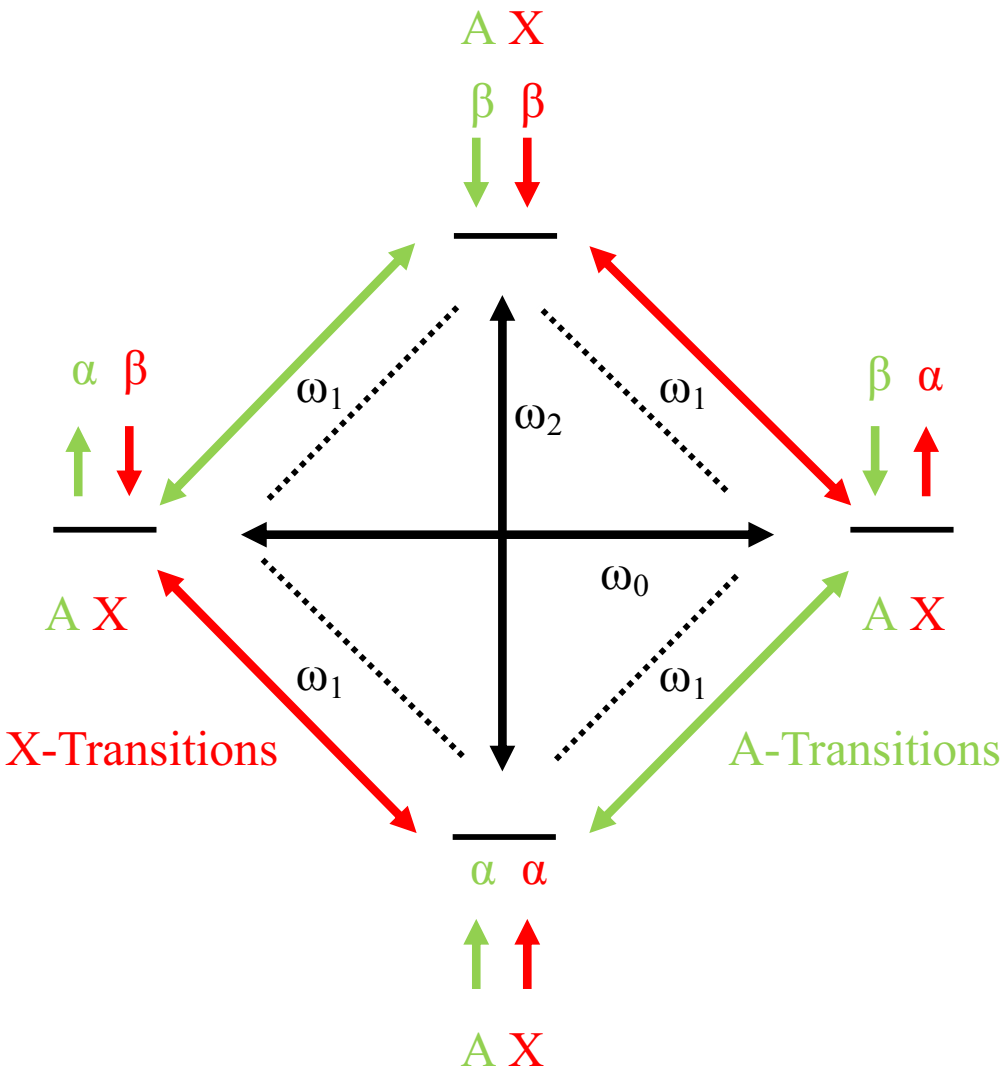

Figure 2.5.: **Possible energy levels and transitions for a pair of nuclei:** The four energy states available for a pair of nuclei (A & X). There are three transition probabilities that can occur, ω_1, a single quantum relaxation between α & β, ω_2, a double quantum relaxation between the $\alpha\alpha/\beta\beta$ spin states, finally ω_0, a zero quantum relaxation between the $\alpha\beta/\beta\alpha$spin states.

$^{1}J_{CH}$ couplings is the inclusion of a 180° ^{1}H refocusing pulse in the middle of the t_1 evolution period, which causes the J coupling to precess back to zero.

^{1}H and ^{13}C NMR can be combined into the Heteronuclear Single Quantum Coherence (HSQC) experiment. This is a two dimensional experiment that correlates ^{1}H and ^{13}C chemical shifts. The spectrum results in a "spot" for each chemically bonded ^{1}H and ^{13}C pair at the intersections of the component spectra. The experiment works via the transfer of magnetization from the ^{1}H nucleus to the ^{13}C nucleus via an Insensitive Nuclei Enhanced by Polarization Transfer (INEPT) step [35]. The ^{13}C chemical shift is encoded during an incremented time delay (t_1) after which the polarization is then transferred back to ^{1}H via a retro-INEPT. Evolution of J-coupling is usually removed by a 180° pulse applied to the ^{1}H nuclei in the middle of the t_1 delay. Once the ^{13}C encoded magnetization has been transferred back to ^{1}H the signal is recorded, usually which simultaneously decoupling ^{13}C. This experiment is useful for separating out peaks that may be overlapped in the 1D spectra, and simplifies the assignment of each peak to the molecule. It can also be applied to other NMR active heteronuclei, most commonly ^{15}N. The ^{1}H-^{15}N HSQC is very useful in protein NMR spectroscopy and will be discussed later. When this experiment is used in conjunction with other two dimensional experiments, such a NOESY and Correlation spectroscopy (COSY)[36] (a common 2D NMR experiment which correlates two homonuclei via J-coupling), it can become an exceptionally powerful tool for solving a molecules structure [37].

2.3. Protein NMR

The same principal experiments used for small molecule NMR can also be applied to proteins and many protein NMR experiments are based on common small molecule experiments [38]. A particularly useful experiment is ^{1}H-^{15}N HSQC.

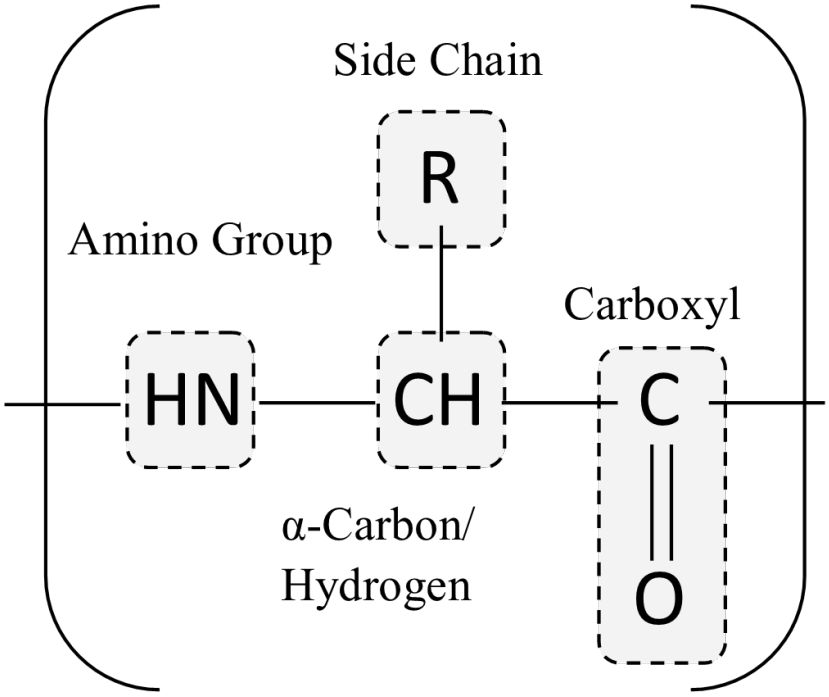

Figure 2.6.: **Structure of an Amino Acid:** The structure of an amino acid with each component labeled.

This experiment results in a spectrum with a one peak for every amino acid residue (excluding of prolines due to their lack of an N-H group), and an additional peak for any side-chain amino groups such as is present in tryptophan [39]. For the assignment of the peaks in the ^{1}H-^{15}N HSQC to their associated amino acid residues a third dimension (containing specific ^{13}C or ^{1}H chemical shifts) is often added to the experiment, allowing the chemical shifts to be assigned sequentially along the backbone through the C_α or H_α and on to each successive amide nitrogen.

Once this has been completed the investigation of the 3D structure can begin. Initially a 3D model for the protein structure is generated using feasible bond lengths and angles. This model is then used as a starting position for iterative energy minimization using computer modeling under the influence of structural restraints obtained from the NMR spectra. The common structural restraints which are used are the nuclear Overhauser effect (NOEs) (distance restraints), J-

couplings (bond angle restraints), and more recently Residual Dipolar Couplings (RDCs) which provide restraints on bond orientations.

The simplest of these restraints are three-bond J-couplings between H_N and H_α which are related to the dihedral angle between their N-H and C-H bonds by the Karplus equation (2.6),

$$J(\phi) = A\,cos^2\phi + B\,cos\,\phi + C \tag{2.6}$$

in which J is the observed coupling constant, ϕ is the dihedral angle, and A, B, and C are all empirical constants. The ranges of possible J-coupling values each correspond to different secondary structures within the protein (J-coupling <6 Hz: $\phi = -90° - -40°$ or a "helical" conformation, J-coupling >8 Hz: $\phi = -150° - -90°$ or a "beta sheet" conformation. J-coupling between 6 - 8 Hz is likely due to rapid switching between multiple conformations.)

The utility of the NOE to define points of close contact is perhaps the most important tool in generating a full three dimensional model using NMR. However the experimental procedures for capturing this information is often very time consuming making the action of solving a structure via NMR a long process. Another limitation of NOEs is the relatively small distance over which they are able to provide information. The size of the NOE has a $\frac{1}{r^6}$ distance dependence, which in practice limits the maximum separation that can be detected to ~ 5 Å, a relatively small distance when considering the size of a full protein.

The most recently developed structural restraints are provided by residual dipolar couplings (RDCs). RDCs are an orientational restraint as they contain information about the relative angle of a chemical bond vector relative to the magnetic field vector ($\mathbf{B}_0$) and they will be discussed in depth in the following section. RDCs are often captured for the amide bonds (N-H) of a protein, however alkyl (C-H), carbonyl (C=O), and even homo nuclear (e.g. H H) RDCs can also be utilized.

2.4. Residual Dipolar Couplings

The angular information gathered from RDCs allows sections of a molecule that may be chemically remote to be aligned relative to each other, improving the quality of the final structure [40]. RDCs are obtained in a middle ground between solution state NMR, where all dipolar couplings are averaged to zero due to rapid isotropic tumbling, and solid state NMR, where due to the spacial restriction of the bond vectors, dipolar couplings can be of the order of several kHz, often preventing detailed analysis if it was not for Magic Angle Spinning (MAS)[41]. The observation of RDCs relies on the rapid tumbling of molecules in a solution state system being slightly anisotropic, resulting in a minute preference for a particular orientation. This small anisotropy results in a residual amount of the dipolar coupling being visible in the spectra, typically of the order of 10s of Hz (i.e. of the order of the J couplings), a much more manageable situation compared to that encountered in solid state NMR.

The small amount of anisotropy nature needed to observe the RDCs is typically generated by either using a nematic liquid crystal phase, or via a strained gel [42, 43, 44]. Liquid crystals show orientational order due to the spontaneous alignment of the elongated particles. Strained gels on the other hand have pores which are forced into anisotropic shapes perpendicular to the strained axis. Both systems produce an anisotropic environment for a hosted molecule sufficient to cause it to show a slight orientational preference due to steric and/or electrostatic interactions.

Nuclear dipolar coupling has already been introduced in the discussion of the NOE in Chapter 2.2. The small magnetic field of a nucleus is able to modify the external magnetic field $\boldsymbol{B_0}$ in a through space effect, where the effect on the second nucleus depends on the spin state of the first ('up' or 'down'). The size of these dipolar couplings (D) is dependent on the angle of the bond vector relative to the external magnetic field, following this relationship:

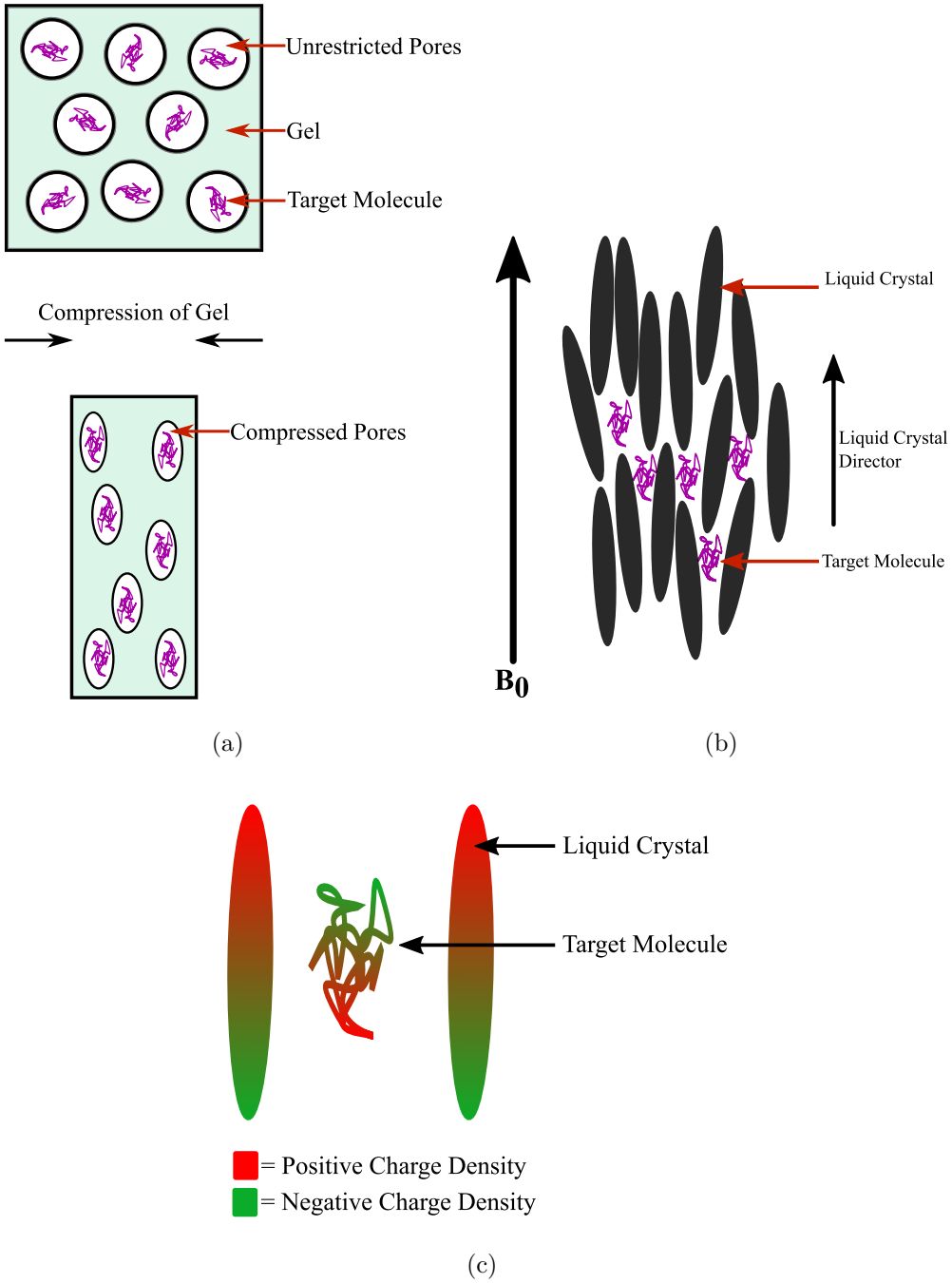

Figure 2.7.: **Types of alignment media commonly used in the capture of RDCs:** a) A compressed gel polymer system. A gel is allowed to swell to its full size in a solution containing the target molecule before is it compressed into a small diameter NMR tube compressing the pores anisotropically limiting the solute molecule in its mobility [43]. b) An example of a liquid crystal system which is relying on steric interaction to limit the rotational freedom of the target molecule. c) An example of another liquid crystal system which is now using electronic interactions to limit the mobility of the solute.

$$D = D_o(1 - 3cos^2\theta) \tag{2.7}$$

where θ is the angle between the inter-nuclear vector in question and $\boldsymbol{B}_0$. D_o is a maximum possible splitting for the pair of nuclei and is determined by the inter-nuclear separation and the product of their gyromagnetic ratios. When this equation is applied to a solution state system where there is equal probability of the inter-nuclear vector in question being oriented anywhere inside a sphere the average value of $cos^2\theta$ is $\frac{1}{3}$, causing the observed dipolar coupling interaction to equate to zero.

As RDCs have become a more common method for refining a protein's structure, new experimental methods for finding the coupling values have been developed each with their own unique benefits and trade-offs. The simplest NMR experiment for capturing these couplings is a coupled-HSQC, where the standard broadband decoupling is simply omitted during the signal acquisition. This results in both J and, if present, residual dipolar couplings developing in the direct dimension of the resultant spectrum.

To separate the RDCs from the J couplings the spectrum is also recorded in the absence of an alignment medium (isotropic solution) in order to obtain a spectrum with just the J-couplings, which can then be removed. A more sophisticated experiment for the capture of RDCs is the In-phase-Antiphase HSQC (IPAP)[45]. The full IPAP experiment comprises two spectra being recorded, one containing the peaks as in-phase doublets (both signals positive), and an anti-phase spectrum where one component of the doublet is positive and the other negative. The addition of these two spectra yields a spectrum that contains one peak from each doublet, while the subtraction of the two spectra leaves the complementary peak. The IPAP spectra halves the number of peaks seen in each spectra, as well as allowing for more accurate detection of the precise peak location, which is important when the RDC values can often be on the order of only a few Hz.

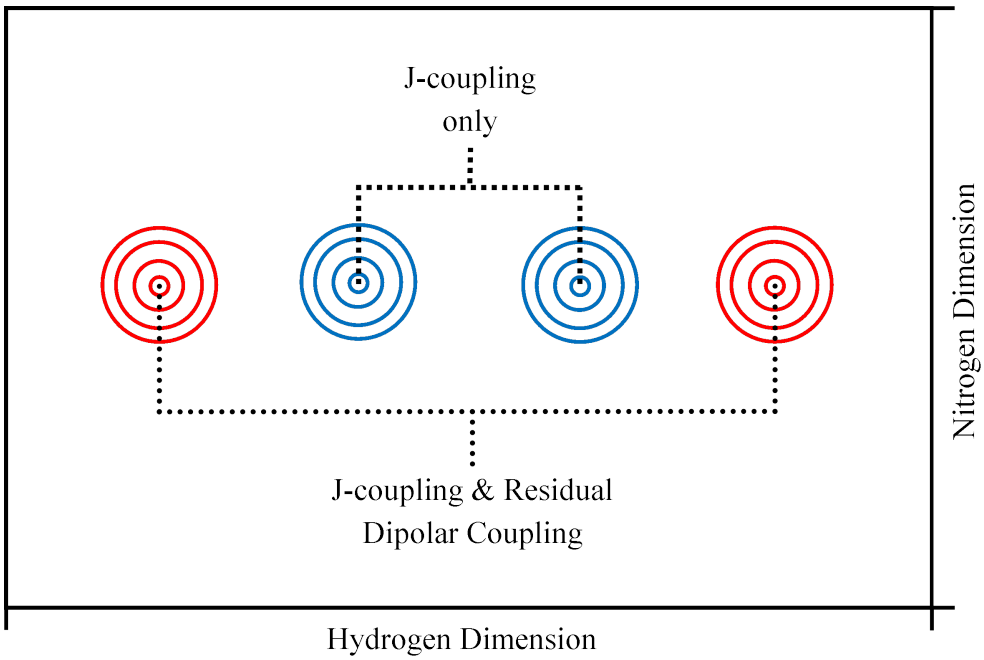

Figure 2.8.: **Coupled HSQC experiment:** Example of two coupled-HSQC experiments applied to a NH bond pair. Isotropic solution experiment results in only the J-coupling being present (blue). And an anisotropic sample used to measure RDCs results in J-coupling and residual dipolar coupling being present (red).

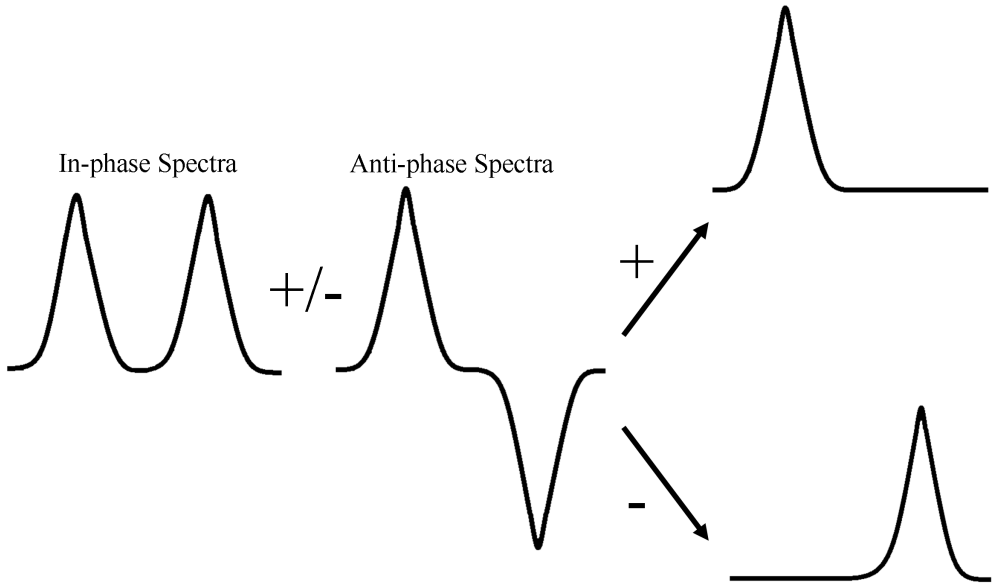

Figure 2.9.: **Components of an IPAP-HSQC experiment:** The IPAP experiment results in two spectra, one with the in-phase splitting, and the other with antiphase doublets. Addition and subtraction of these two spectra result in two spectra each with one peak from the doublet allowing more accurate detection of their separation.

Once the RDC values are obtained from the spectra, information about the angles of the inter-nuclear vectors needs to be extracted. This information is extracted via the following equations for a pair of nuclei, p and q. The overall equation for each dipolar coupling, D_{pq} is:

$$D_{pq} = \frac{D_{max}}{r_{pq}^3}\left(cos^2\theta - \frac{1}{3}\right) \tag{2.8}$$

$$D_{max} = \frac{-3}{8\pi^2}\gamma_p\gamma_q\mu_0\hbar \tag{2.9}$$

where r_{pq} is the internuclear distance between nucleus p and nucleus q, θ is the angle between the internuclear vector joining the two nuclei p and q and the magnetic field. D_{max} is the maximum possible dipolar coupling value for the pair of nuclei, and is comprised of γ_p and γ_q which are the gyromagnetic ratio of each nucleus, μ_0 is the vacuum permeability constant, and $\hbar$ is the reduced Planck constant. For mobile samples we measure a time average of the dipolar coupling, resulting in the following equation:

$$\left\langle D_{pq}\right\rangle_t = \frac{D_{max}}{r_{pq}^3}\left\langle cos^2\theta - \frac{1}{3}\right\rangle_t \tag{2.10}$$

This unfortunately is not simple to solve in the laboratory reference frame used up to this point in which the magnetic field direction is constant and the molecular orientation varies. A molecular frame is now used in which the Cartesian coordinates are fixed to a single target molecule, and the magnetic field is constantly rotating instead. This allows a probability tensor to be determined which describes the average probability of the magnetic field pointing in a given direction:

$$\left\langle cos^2\theta\right\rangle_t = \overrightarrow{r}^{\,t}\hat{P}\overrightarrow{r} \tag{2.11}$$

in which $\overrightarrow{r}$ is a single internuclear unit vector and $\hat{P}$ is the probability tensor. As the probability tensor is real, symmetric, and has a trace of 1 it can be moved into another reference frame in which $\hat{P}$ has a diagonal representation and the previous equation is reduced to the following:

$$\overrightarrow{r}^{\,t}\hat{P}\overrightarrow{r} = P_x r_x^2 + P_y r_y^2 + P_z r_z^2 \tag{2.12}$$

which does allow a solution to be found, however as a probability is of limited use, it is possible to go another step further and instead of the probability tensor use an alignment tensor, $\hat{A}$ given by:

$$\hat{A} = \hat{P} - \frac{1}{3}\hat{1} \tag{2.13}$$

which when combined with Equation 2.11 gives the following:

$$\left\langle cos^2\theta - \frac{1}{3} \right\rangle_t = \overrightarrow{r}^{\,t}\hat{A}\overrightarrow{r} \tag{2.14}$$

Solving this equation via a least squares method is now trivial, the effect of the gyromagnetic ratios and the internuclear distances can be easily removed from the observed couplings by dividing by the distance and constant components leaving a reduced coupling, as displayed in the following equation:

$$D^{reduced} = \overrightarrow{r}^{\,t}\hat{A}\overrightarrow{r} = (x\ y\ z)\begin{pmatrix} Axx & Ayx & Azx \\ Axy & Ayy & Azy \\ Axz & Ayz & Azz \end{pmatrix}\begin{pmatrix} x \\ y \\ z \end{pmatrix} \tag{2.15}$$

As the alignment tensor is traceless ($Axx + Ayy + Azz = 0$) and symmetric ($Axy = Ayx$, $Axz = Azx$, $Ayz = Azy$) algebraic manipulation can reduce the prior equation down, leaving only five unknown components, as is shown in the following equation (in this case Axx has been replaced with $-(Ayy + Azz)$):

$$D^{reduced} = (2xy \;\; 2xz \;\; y^2 - x^2 \;\; 2yz \;\; z^2 - x^2) \begin{pmatrix} Axy \\ Axz \\ Ayy \\ Ayz \\ Azz \end{pmatrix} \tag{2.16}$$

Once five or more RDC values have been measured Equation 2.16 can be turned into a set of simultaneous equations which are easily solved as shown in the following:

$$\begin{pmatrix} D_1^{reduced} \\ D_2^{reduced} \\ \cdots \\ D_n^{reduced} \end{pmatrix} = \begin{pmatrix} 2x_1y_1 & 2x_1z_1 & y_1^2 - x_1^2 & 2y_1z_1 & z_1^2 - x_1^2 \\ 2x_2y_2 & 2x_2z_2 & y_2^2 - x_2^2 & 2y_2z_2 & z_2^2 - x_2^2 \\ & & \cdots & & \\ 2x_ny_n & 2x_nz_n & y_n^2 - x_n^2 & 2y_nz_n & z_n^2 - x_n^2 \end{pmatrix} \begin{pmatrix} Axy \\ Axz \\ Ayy \\ Ayz \\ Azz \end{pmatrix} \tag{2.17}$$

Once Equation 2.17 has been solved and an alignment tensor has been extracted for the target molecule, theoretical RDCs are back calculated as a way of verifying the alignment tensor. Equation 2.17 is the crux equation that is used in the analysis of RDC data sets, and can be applied with any one of the three components (reduced RDCs, structural information, or alignment tensor) missing, to determine the missing component. In addition to the alignment tensor representation, many in the RDC community have taken to using another representation, the Saupe tensor ($\hat{S}$), which is simply the alignment tensor scaled by a factor of $\frac{3}{2}$.

$$\hat{S} = \frac{3}{2}\hat{A} \tag{2.18}$$

In order to make the alignment and Saupe tensors more usable further information can be extracted from it such as the eigenvectors and eigenvalues, as well as an axial and rhombic component. The eigenvectors and eigenvalues are by solving the following equation:

$$A\nu = \lambda\nu \tag{2.19}$$

with A being a square matrix, ν being the non-zero eigenvector, and λ being the eigenvalue for each eigenvector. As the alignment tensor is a 3x3 symmetric and traceless tensor there will be three eigenvectors and eigenvalues for this system. The eigenvalues are also the diagonal components of the diagonalized alignment tensor (alignment tensor in the principle axis frame). The axial component of the alignment tensor is found to be equal to $\frac{3}{2}$ of the 'zz' component of the diagonalized alignment tensor.

$$A_a = \frac{3}{2}A_{zz}{}^{d} = S_{zz}{}^{d} \tag{2.20}$$

The rhombic component of the alignment tensor is found to be another combination of the diagonalized alignment tensor components as represented in the following equation:

$$A_r = A_{xx}{}^{d} - A_{yy}{}^{d} = \frac{2}{3}\left(S_{xx}{}^{d} - S_{yy}{}^{d}\right) \tag{2.21}$$

The rhombicity of the tensor can now be described by dividing the rhombic component by the axial component.

$$R = \frac{A_r}{A_a} \tag{2.22}$$

Verification of this tensor involves the calculation of a structure quality factor or *Q-factor* which is analogous to the R - factor that is seen in X-ray crystallography. The Q-factor is calculated according to the following equation:

$$Q = \frac{\sqrt{\left[\sum_{i-1,\ldots,N} \frac{(D^{obs}-D^{calc})^2}{N}\right]}}{D^{rms}} \tag{2.23}$$

in which D^{obs} and D^{calc} are the observed and back calculated values for each dipolar coupling, N is the number of residues present in the calculation over which this summation takes place. D^{rms} is a root mean square value for the set of dipolar coupling found via the following equation [46, 47]:

$$D^{rms} = \sqrt{D_a^2 \frac{[4 + 3\left(\frac{D_r}{D_a}\right)^2]}{5}} \tag{2.24}$$

where D_a and D_r are the axial and rhombic components of the diagonalized Saupe tensor.

Currently several software packages exist that allow the alignment tensor to be calculated as well as all of the characterization of the Saupe tensor (several further parameters e.g. Euler angles). One of the most widely used of these packages is PALES which contains a multitude of functions applicable to the study of RDCs, the most integral being the ability to generate an alignment tensor when provided with a set of measured RDCs and a structural model allowing verification of the model, as well as demonstrating areas of the structure which may be more labile[48]. This package is heavily used when working with protein structures due to the simplicity of dealing with the numbering of nuclei that can become increasingly complex in other small molecule packages.

This process can be applied to a variety of molecules including both small molecule and bio-molecules such as proteins and nucleic acids, and can prove to be useful for structural calculations of all molecules.

When RDCs are used to improve the quality of a molecules structure that is calculated it is often useful to have multiple unique RDC data sets that have been obtained with the target molecule in different orientations. The current methods for obtaining theses multiple orientations involves a trial and error type approach of placing the target molecule in to solutions with a variety of different orienting media (strained gels, liquid crystals, bicelles etc.) and hoping that these differing media allow the molecule to be aligned in unique orientations, yielding multiple suitable sets of data. Unfortunately this method is very time consuming, and expensive given that each alignment medium may not give a unique alignment of the target molecule. This project investigated the application of a shear force to a single orientation media with the hopes of generating multiple orientations, allowing several unique RDC data sets to be captured.

2.5. Rheo-NMR

Rheology is the study of the deformation and flow of matter, usually liquids. Understanding the molecular level changes that give rise to the larger macroscopic mechanical changes in the fluid especially with bio-polymers such as proteins, DNA and polysaccharides is becoming hugely important for industries product development. The traditional methods for studying such changes include light scattering based methods and rheometry. Unfortunately these methods are not perfect, light scattering requires the sample to be optically transparent, a requirement that may not always be able to be met easily with polymer samples, while rheometry can only yield an average of the bulk sample, rather than targeted information about regions of the sample. One of the other methods for completing rheological methods is NMR, giving rise to Rheo-NMR. Rheo-NMR can give information about spectroscopic changes in the structure of a molecule, in addition to the ability to glean information about the molecular dynamics, bulk orienta-

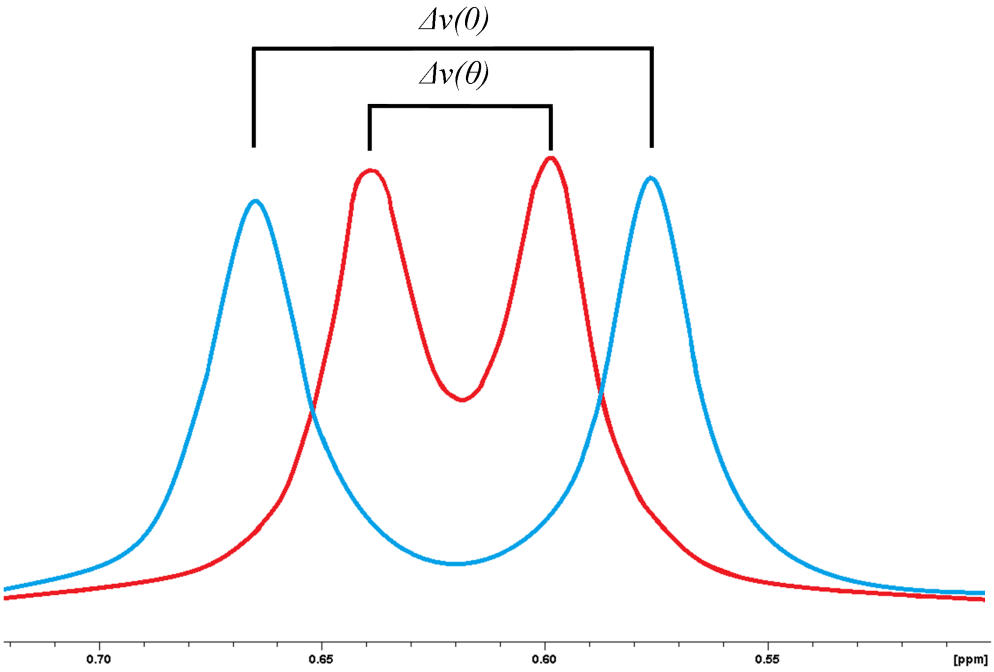

Figure 2.10.: **Example ^{2}H spectra**: The quadrupolar splitting between each doublet is annotated as either showing $\Delta v(\theta)$ or $\Delta v(0)$, depending on the angle at which the liquid crystal's director is found to be.

tion, and other useful parameters. Rheo-NMR also has an advantage of being applied to optically opaque samples without any modification to experimental techniques, allowing an increasingly large range of samples to be studied.

One class of materials that have been extensively studied by Rheo-NMR is liquid crystals [49, 50]. Liquid crystals are a state of matter that has properties bridging both traditional liquids and crystalline substances [51]. A liquid crystalline substance in the absence of any external forces will have a high degree of orientational order but no translational order over long ranges, and will flow like a liquid. Some of these liquid crystal substances will align their long axes when a strong magnetic field is applied, resulting in the sample having an overall *director* corresponding to the long axis of the liquid crystal molecules aligned with the magnetic field (provided the liquid crystal has a magnetic anisotropy aligned along its long axis). Several studies have looked into what effect the application of a shear force can have on the director angle of a nematic liquid crystal and have

found that it will reorient from being parallel to being nearly perpendicular to the magnetic field of the spectrometer (for a system with a positive diamagnetic susceptibility anisotropy) [11, 12, 49, 50, 52]. These measurements were carried out using ^{2}H NMR spectra to monitor the liquid crystal's director angle via the observed quadrupolar splitting of the oriented deuterium oxide solvent. These have the following relationship:

$$\Delta v(\theta) = \left| \frac{1}{2} \Delta v(0) \left(3cos^2\theta - 1\right) \right| \tag{2.25}$$

in which θ is the angle of the liquid crystal director relative to the magnetic field, $\Delta v(0)$ is the quadrupolar splitting value when the liquid crystal director is under no shear and at equilibrium, and $\Delta v(\theta)$ is the quadrupolar splitting value while the sample is under shear [12]. The ability to reorient a liquid crystal using shear is a cornerstone of this project.

Another prerequisite is that shear forces should not perturb the structure of the molecule under investigation. The effect that a shear force may have on the structure of a molecule has been investigated by Ashton *et al.* [53]. It could be imagined that if a macromolecule such as a protein, which is held together largely with weak intermolecular forces, was sheared with sufficient force the structure may be somewhat perturbed. There are many rheological techniques which could be used to monitor this perturbation, including high-resolution Rheo-NMR. Since structural changes are usually accompanied by changes in chemical shifts it is simple to monitor ^{1}H spectra for any changes when a shear force is applied.

One of the simplest approaches to applying a shear force to a sample inside a NMR spectrometer involves a *Couette cell* design. This involves an outer NMR sample tube with a diameter corresponding to the probe diameter, with a smaller diameter NMR tube placed concentrically inside it. The inner tube is rotated while the outer remains stationary, resulting in the application of a shear force

to the sample. The design of a couette cell and motor will be described in depth later.

3. Experimental Methods and Preliminary Results

The goal of this thesis is to investigate the effects on the NMR spectrum of a protein placed in an alignment media that is then sheared by the application of a shear stress. Understanding what effect this shear stress is having on the alignment media is an undoubtedly important part of this, and will be discussed below.

3.1. Shear Cells

There are many unique geometries for shear cells. Typically such devices are used in rheology experiments in order to mechanically characterize a sample. Some of the more common geometries used in rheometers include the following:

- A cone and plate set-up, where a sample is placed on a flat plate and a shallow cone is lowered into contact with the sample. This can be used to measure the forces that are transferred through the sample by rotating the plate or cone relative to the surface.

- A capillary set-up where a sample is pushed through a tube of known dimensions. This exerts a shear force onto the sample that depends on the flow rate of the sample through the tube. This allows the mechanical prop-

erties of a sample flowing through pipes to be determined, giving insight to how fluids are moved around in industrial processes.

- A Couette cell or rotational cylinder design involves two concentric cylinders with a sample being placed between the two tubes. One of the cylinders is rotated resulting in a shear force being applied across the annulus between the cylinders. This results in a velocity gradient forming across the gap between the two cylinders which can be calculated (shown in Equation 3.1, where $\dot{\gamma}$ is the applied shear rate across the annular gap, ω is the angular velocity, and R_i and R_o are the inner and outer radii of the gap between the two cylinders [54, 55]). This is the design that has been chosen in the past for rheo-NMR studies due to the ease of implementing such a device inside the probe of a NMR spectrometer and has been the focus in this work.

$$\dot{\gamma} = -\frac{2\omega}{1 - \left(\frac{R_i}{R_o}\right)^2} \tag{3.1}$$

3.1.1. First Generation

As NMR sample tubes are cylinders the most basic design possible for creating a Couette cell that would function inside a NMR spectrometer involves an NMR tube loaded with the sample with a smaller diameter tube being placed inside. This creates an annular gap containing the sample between the two tubes. The inner tube can then be rotated which will create a shear gradient across the sample. This is a functioning design for a rheo-NMR setup, however if there is nothing constraining the inner tube it is likely that the rotation would not be concentric, resulting in momentary uncontrollable changes to the shear rate.

To counter this problem, a first generation rheo-NMR cell was designed in house and included a small semi-spherical cup which sat in the base of the outer tube which directed the inner NMR tube towards the center. In addition to this, a small ring was designed to sit at the top of the outer tube designed again

to keep the inner tube centered. As this cell is designed to be placed inside a high resolution NMR spectrometer it is important that the materials used in its construction are not magnetic and have small enough T_2's in order to be "NMR invisible" so as to not to interfere with the spectra of the sample. As such the material that has been chosen to make each of these fittings is polyether ether ketone (PEEK), an inert temperature stable plastic. The NMR tubes chosen for this cell are a 5 mm outer diameter thin walled NMR tube (type 507-PP-7, Wilmad Glass Co.) (inner diameter of 4.2 mm) and a 3 mm outer diameter NMR tube (type 307-PP-8, Wilmad Glass Co.) as the inner cylinder. This results in an annular gap of 0.6 mm which is available to be filled by the sample (Figure 3.1). This design did prove to be effective at stabilizing the inner tube, however was often problematic due to the cup becoming stuck in the base of the 5 mm tube. To remedy this a new tube design was proposed which countered this problem, based on a previously successful larger scale rheo-NMR setups.

3.1.2. Second Generation

An improved cell design was implemented which involved a 5 mm outer diameter NMR tube with the sealed end removed. This end was replaced by a PEEK cap which allowed the inner tube to be held in better alignment without removing possible sample space. A stabilizing ring was again used around the neck of the 5 mm tube to hold the inner 3 mm tube in the center. In addition to this a long PEEK plug was placed into the top of the 3 mm inner tube to increase the strength of the inner tube, which was often prone to breaking in the previous generation set-up (Figure 3.2). This second generation set-up was designed and initially built by Tim Brox from the Victoria University Magnetic Resonance group.

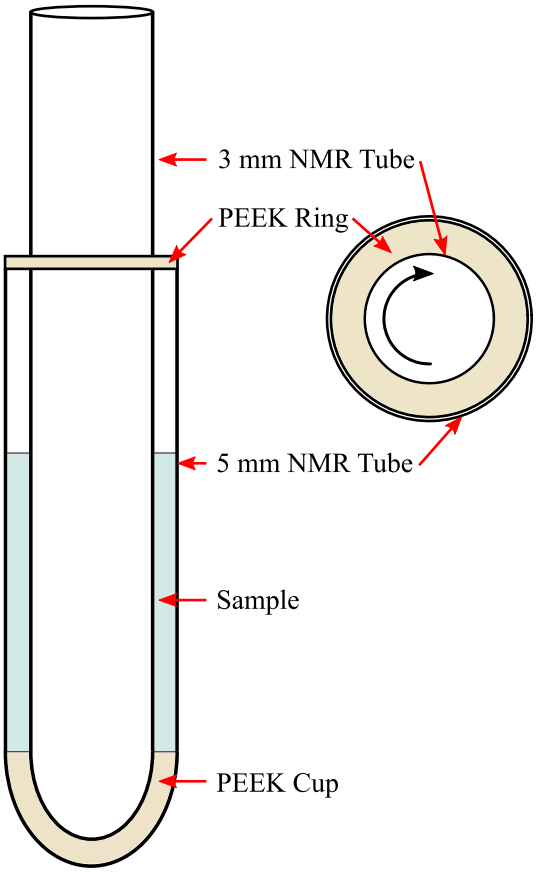

Figure 3.1.: **First generation shear cell:** First generation shear cell set up utilizing a 5 mm NMR tube as the outer shell, and a 3 mm NMR tube as the inner wall. PEEK fittings are included at the neck of the 5 mm tube and between the bases of the tubes in order to provide stability.

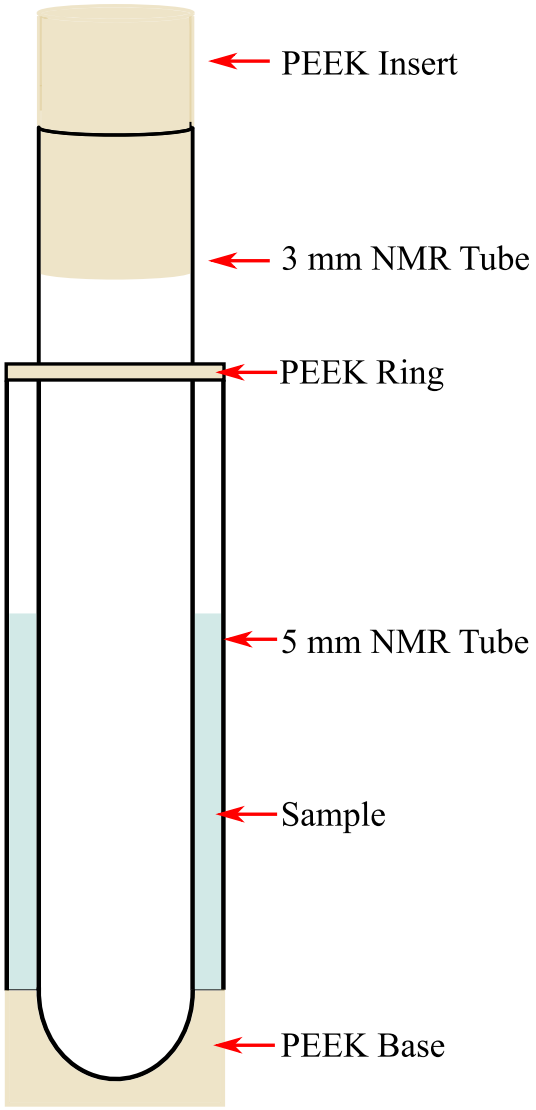

Figure 3.2.: **Second generation shear cell:** Second generation shear cell set up with an open ended 5mm NMR tube capped with a PEEK fitting. A standard 3mm NMR tube is held inside by a PEEK ring around the neck of the 5mm tube. A 3mm diameter PEEK insert is placed inside the 3mm tube for added strength.

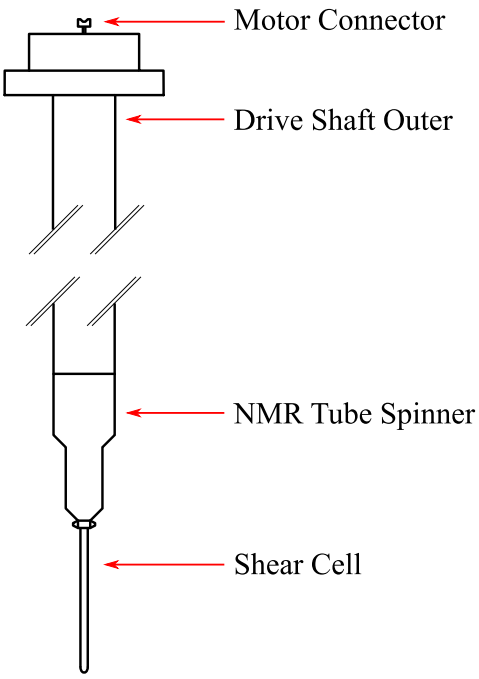

Figure 3.3.: **Schematic diagram of the drive shaft connected to each shear cell**

3.1.3. Drive Shaft

In order to be able to shear the sample the inner tube of the rheo-cell needs to be rotated. To do this a drive shaft which is clamped to the inner tube while holding the outer tube in place is used. This allows the movement of the inner tube to be controlled outside of the spectrometer by attaching a motor to drive the system. The drive shaft design has remained constant throughout the development of other shear cell designs, and consists of a long aluminum shaft which holds the 5 mm outer NMR tube through a design similar to that of a standard NMR spinner. The 3 mm inner tube is connected via a clamping screw to the drive shaft which extends out the top of the spectrometer ending with a coupling joint which can be attached to an external motor.

3.2. Shear Drive Motors

3.2.1. First Generation

The original motor that has been used to apply a shear force to the sample tube is a simple stepper motor with a rotation rate range between 0.1 Hz and 14 Hz. This motor was designed and built by Robin Dykstra & Terry Southern and is controlled via an external micro-controller which allows the rotation rate to be increased step wise, or reset to zero. These alterations to the rotation rate are able to be controlled either manually, or via a serial port communication link with the spectrometer computer. The ability to control the motor via a serial port connection is vitally important as not only does it allow the desired speed of the motor to be set rapidly, but also gives the possibility of changing the rotational rate of the motor dynamically, and introducing waveforms of rotation rate.

The control of this motor via the spectrometer was scripted inside TopSpin 2.1 (Bruker BioSpin, Rheinstetten, Germany), a program for data acquisition and analysis on Bruker NMR spectrometers. The programs written in the spectrometer's scripting language are known as "AU programs", this language was developed especially for use within TopSpin. It is built on an underlying C structure with the addition of several macros specific to the capture and processing of NMR data. Several AU programs have been written to aid in the control of this motor including a simple script which increases the rotation rate to a given rate with a ramp; a script which allows the rotation rate to be switched between two set values; and several other variations of waveforms.

This first generation motor was an effective tool for generating shear forces inside the Couette cell, however the range of rotation rates available to this motor was limited to a range between 0.1 Hz and 14 Hz, with step size of 0.1 Hz. The minimum rotation rate of 0.1 Hz has been lowered through the use of a gear box

with a ratio of 1:50, giving a new rotation rate range of 0.002 Hz to 0.28 Hz with steps of 0.002 Hz.

3.2.2. Second Generation

A second generation motor was developed by Beta Solutions for Magritek which set out to allow the application of higher shear forces, along with easier feedback and script development. This motor has an operating rate ranging from 0.1 Hz to upwards of 60 Hz. The micro-controller for this motor is now mounted directly on the drive unit itself, greatly reducing the bulk of the system and the system is communicated with by writing commands to a USB port (Figure 3.4). This allows a variety of different types of programs to control the motor including scripting languages which have access to system level processes. Several scripts for control of the motor were developed using Python 2.7, a common programming language. These scripts ranged from simple scripts that turned the motor on at a given speed, to more complex scripts that allowed the rotation rate of the motor to follow a waveform. In addition to the AU programs which were mentioned briefly in 3.2.1, it is also possible to develop scripts in TopSpin using Python as the base language. This allowed this second generation motor to be controlled in a similar fashion to the previous motor, and will allow for some interesting developments for full integration of motor control into pulse programs in the future.

3.3. Rheo-NMR of liquid crystal phases

In order to investigate the capability of the shear cell to reorient anisotropic materials several liquid crystals were prepared and subjected to stresses in the shear cell.

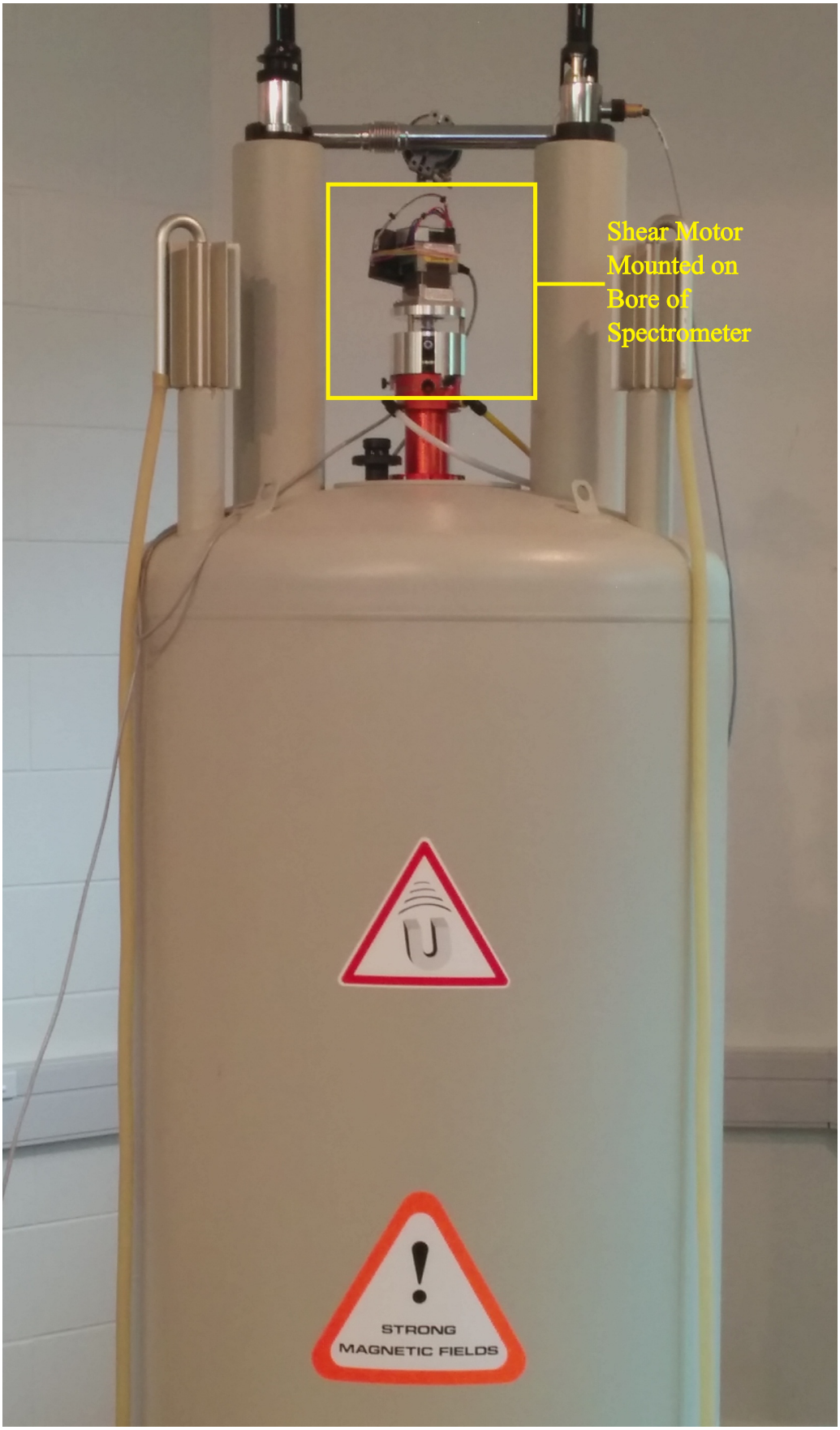

Figure 3.4.: **Second generation motor:** 500 MHz Bruker NMR Spectrometer with Second Generation shear motor mounted atop the bore.

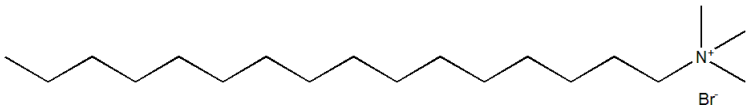

Figure 3.5.: **Molecular structure of CTAB**

3.3.1. CTAB in D_2O

3.3.1.1. Introduction

Cetyltrimethylammonium bromide (CTAB) is a cheap commonly available cationic surfactant which, given appropriate conditions, can self-assemble into worm-like micelles. This self-assembly is driven through the amphiphilic structure of the CTAB molecule where the ammonium bromide head is highly polar and well solvated in water, in contrast to the long aliphatic tail of the molecule which has a very low solubility in water. When a sufficiently high concentration of the CTAB molecules are present in an aqueous system the self assembly process will begin, with the aliphatic hydrocarbon tails aligning leaving only the hydrophilic ammonium heads exposed to the solution. This results in a worm-like micelle structure. These micelles can grow in length through either increased concentrations of CTAB, or through lowering of the temperature, eventually reaching a critical length where the micelles will form a nematic liquid crystal phase (nematic liquid crystal phases have orientational order but no translational order). Deuterium NMR is a very powerful tool that can be used to track the formation of the micelles and more importantly the orientation of the nematic liquid crystal director formed by CTAB solutions. A liquid crystal's director is the average bulk orientation of the structures within the sample about which Brownian fluctuations take place, as shown in Figure 3.6.

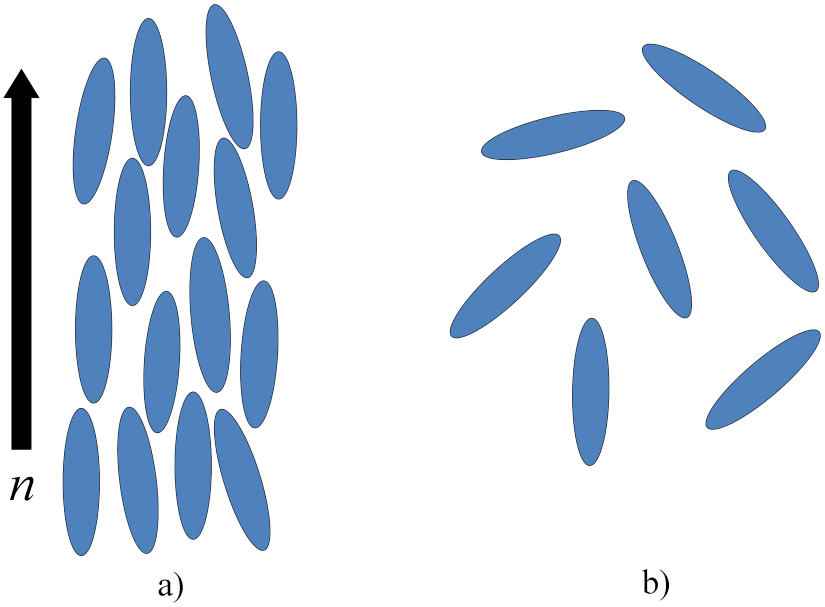

Figure 3.6.: **Different phases of a rod like molecule:** a) Nematic liquid crystal phase where n is the overall director orientation of the sample, aligned with the long axis of the structure present in solution. b) An isotropic solution phase sample where there is no overall orientation of the structures present.

3.3.1.2. Experimental Method

Samples of CTAB (BDH Chemicals) in D_2O (99.9% deuteration, Cambridge Isotope Laboratories) were prepared to 20 wt% and dissolved using a bath of warm tap water before being mixed thoroughly on a vortex mixer for 5 minutes.

All ^2H NMR work reported in this section was carried out on a Bruker 500 MHz NMR spectrometer operating at 76.8 MHz with a spectral width of 500.8 Hz and one scan per FID.

The samples were loaded into a first generation shear cell and placed into the spectrometer and allowed to equilibrate at 309 ± 1 K for 30 minutes before any spectra were recorded. A set of control experiments without any shear applied were carried out. The first ^2H spectrum was recorded at 309 ± 1 K before the temperature was lowered to 303 ± 1 K and allowed to equilibrate for 10 minutes before a second spectrum is recorded.

Another experiment was then carried out at 303 ± 1 K in which the sample experienced an average shear rate of 251.79 s^{-1} applied through the first generation motor running at 14 Hz. The deuterium spectrum were measured and the quadrupolar splitting observed was compared to that of the static system.

The next experiment that was carried out on these samples investigated the rate of reequilibriation after the application of a shear force. A "2D" NMR experiment of the ^2H spectrum vs. time was carried out with 800 rows in the time dimension and a delay between scans of 1 s. This experiment had the sample under an average shear of 215.82 s^{-1} for the first 10 rows, before the shear was ceased for the remainder of the experiment.

3.3.1.3. Results and Discussion

The first control experiments carried out on CTAB set out to show that indeed there is an isotropic to nematic phase transition between 309 ± 1 K and 303 ± 1 K. By monitoring the ^2H NMR spectra of the sample as it is cooled between the two temperatures it was seen that a single isotropic D_2O peak (characteristic of an isotropic phase) is split into a quadrupolar doublet as the sample becomes aligned into a nematic phase. Figure 3.7 clearly shows the difference between the two spectra.

As it has been seen that a nematic liquid crystal phase can be established, the effect that shear had on this anisotropic phase was now investigated. As soon as a shear force was applied to the couette cell there were major changes in the ^2H spectrum. Once the sample had reached an equilibrium under shear the spectrum was recorded and can be seen to be notably different from the spectrum without an applied shear force (Figure 3.8). As described in Equation 2.25, the angle of the liquid crystal's director can be calculated from the values of the quadrupolar splitting. The experiment without any applied shear force was found to have a quadrupolar splitting value of 18.5 ± 0.1 Hz ($\Delta\nu(0)$), while the experiment under

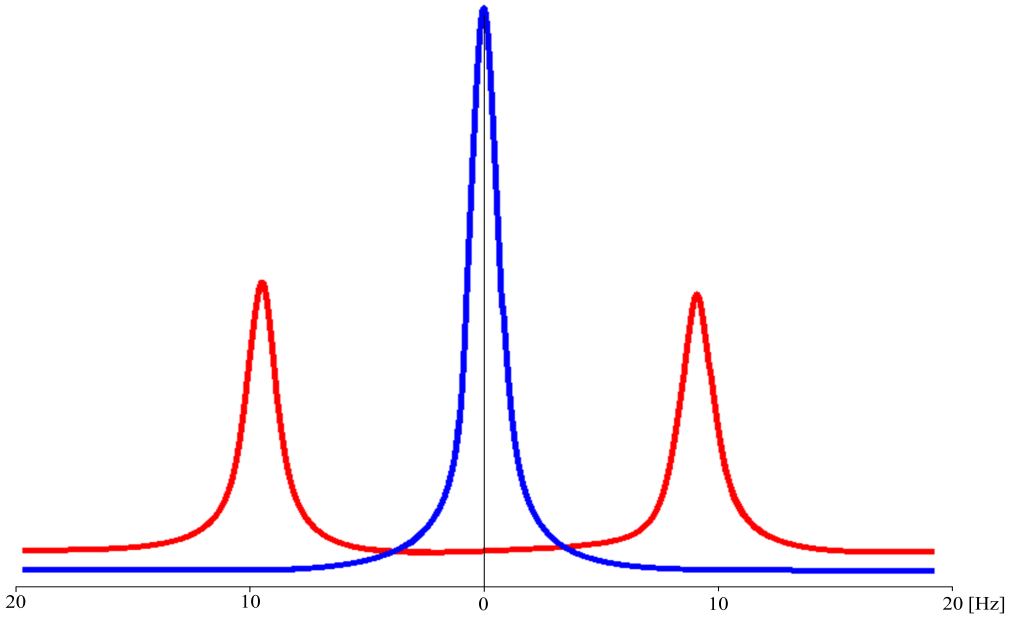

Figure 3.7.: **^{2}H spectra of isotropic and nematic CTAB:** Two control spectra obtained from 20 wt% sample of CTAB in D_2O. Blue spectrum is measured at 309 K and shows a single isotropic peak. Red spectrum is measured at 303 K and shows a quadrupolar doublet.

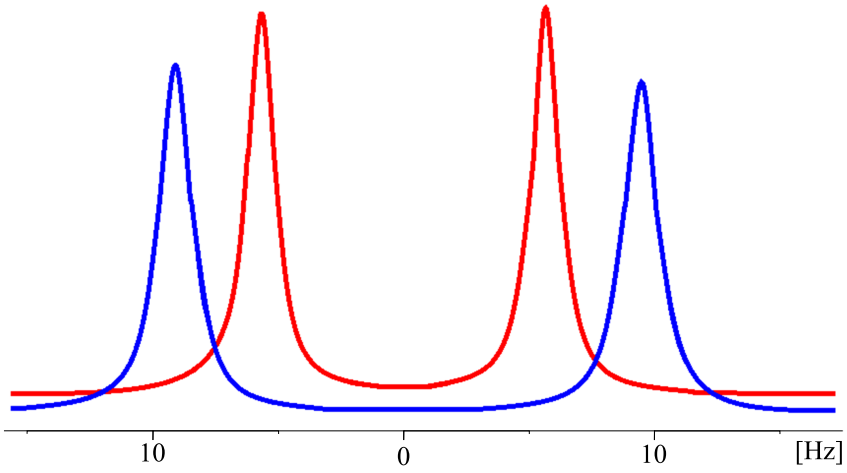

Figure 3.8.: **The effect of an applied shear force on the ^{2}H spectra:** Spectra showing the difference in the quadrupolar splitting when the CTAB nematic phase sample has a shear force applied. Blue spectrum is the unsheared experiment. Red spectrum is a sample being sheared at a rate of 251.79 s^{-1}

shear was found to have a splitting value of 11.3 ± 0.1 Hz ($\Delta\nu(\theta)$). These values are found to correspond to a director angle of $30.75 \pm 0.5°$ relative to the external magnetic field, showing that the application of a shear force will indeed reorient a liquid crystal phases director angle.

The 2D experiment carried out on the relaxation of the liquid crystal's director back towards an equilibrium position showed interesting results. As is shown in Figure 3.9, when the shear force ceases to be applied the quadrupolar splitting decreases to zero, before expanding out to the maximum (the splitting seen when the director is aligned with the magnetic field).

3.3.1.4. Conclusion

These results fit those seen in prior works by our group [11, 12], showing that the application of a shear force to a liquid crystal sample made from micelle structures reorients the phase and that the angle between the director and the

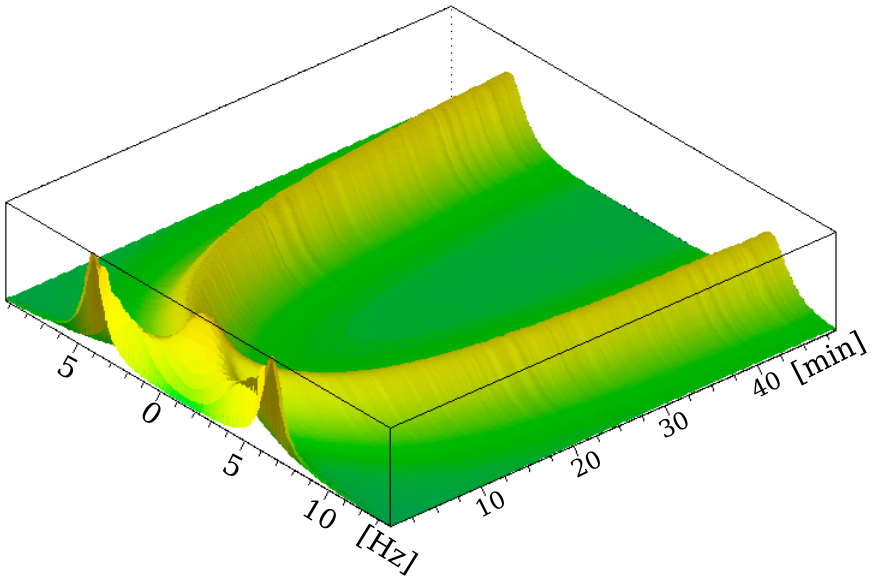

Figure 3.9.: **2D ^{2}H NMR spectrum while the CTAB director is relaxing:** 2D NMR showing the changes in the quadrupolar splitting as the liquid crystal's director relaxes back towards being parallel with the magnetic field.

magnetic field can be obtained from the splitting in the deuterium spectra using a $|3cos^2 - 1|$ relationship. This shows that the shear cell setup used is working as designed and may be suitable for reorientation of other liquid crystal materials.

3.3.2. PBLG in $CDCl_3$

3.3.2.1. Introduction

Poly-γ-Benzyl-L-Glutamate (PBLG) is an amphiphilic chiral polymer comprised of a derivative of the amino acid Glutamic acid. The polymer is highly soluble in non-polar organic solvents such as chloroform. The polymer forms long helical strands in solution, which when exposed to a strong external magnetic field will align parallel with the external field. When the correct concentration and solvent conditions are met, this sample can behave as a nematic phase liquid crystal. This experiment set out to discover if an alternative liquid crystal solution is able to be reoriented under shear forces, and the time scales involved in such a

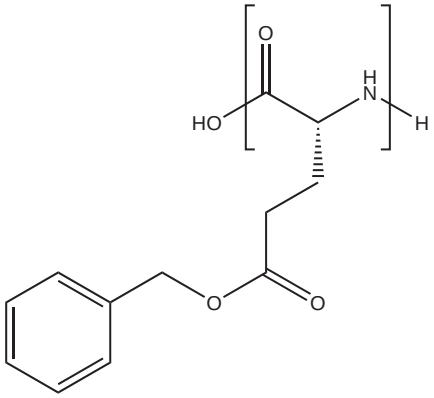

Figure 3.10.: **Molecular structure of the monomer γ-Benzyl-L-Glutamate.**

reorientation. Again the orientation of the liquid crystal director (which in this system is the long axis of the PBLG is the director) is monitored through ^{2}H NMR with the deuterium probe being a deuterated solvent.

As PBLG is a polymeric structure it is possible to vary the molecular weight in order to change the physical properties. One of the properties that has been investigated by other groups prior is the effect that molecular weight has on the orientational properties of the liquid crystal formed by PBLG [56]. It has been found that having a higher molecular weight PBLG will yield a higher quality spectra of an included molecule as well as a lesser degree of alignment on a target molecule.

3.3.2.2. Experimental Method

A low molecular weight PBLG sample (low MW PBLG) was prepared from 79.1 mg of PBLG (70,000 - 150,000 molecular weight, Sigma Aldrich) which was placed into a 5 mm NMR tube with 720 mg of deuterochloroform (99.8% deuteration, SDS) and was left overnight for the PBLG to dissolve. The sample was then inverted and centrifuged multiple times in a custom built NMR tube centrifuge to increase the homogeneity, before being set up as a rheo-cell by inserting a 3 mm inner tube as described previously. NMR measurements were carried out

Table 3.1.: **Shear rates applied to low molecular weight PBLG samples.**

Avg. shear rate [s^{-1}] [a]	Max shear rate [s^{-1}] [a]
0	0
18	26
36	51
72	103
108	154
0	0

[a] Shear rates are calculated using a program written in house by Prof. Bill Williams.

on a Bruker 500 MHz NMR spectrometer operating at 76.8 MHz with a spectra width of 3 kHz at 298 ± 1 K. This sample was exposed to a variety of shear rates ranging from 17 s^{-1} to 108 s^{-1} as described in Table 3.1 chosen to given a range of values and demonstrate any possible differences in response.

In addition to constant shear profiles, a variety of wave forms were applied using the second generation motor and looped through for a given time. These profiles were decided upon as a possible method of generating stable intermediate angles between those seen with constant shear forces. A simple 1D experiment with 16 scans per FID and a delay between scans of 1 s was carried out to measure the maximum quadrupolar splitting (obtained without the application of any shear). In addition to this a "2D" experiment comprised of several 1D scans stacked over time was also implemented for the monitoring of the effect of shear over time. These "2D" experiments had one scan per row and a recycle delay of 1 s. The applied shear profiles which were run are described in Table 3.2 and Figure 3.11.

The effect of molecular weight was also investigated by preparing a high molecular weight sample. 147.3 mg of PBLG (150,000 - 300,000 molecular weight, Sigma Aldrich) along with 950 mg of deuterochloroform and 55.8 mg of (+)-

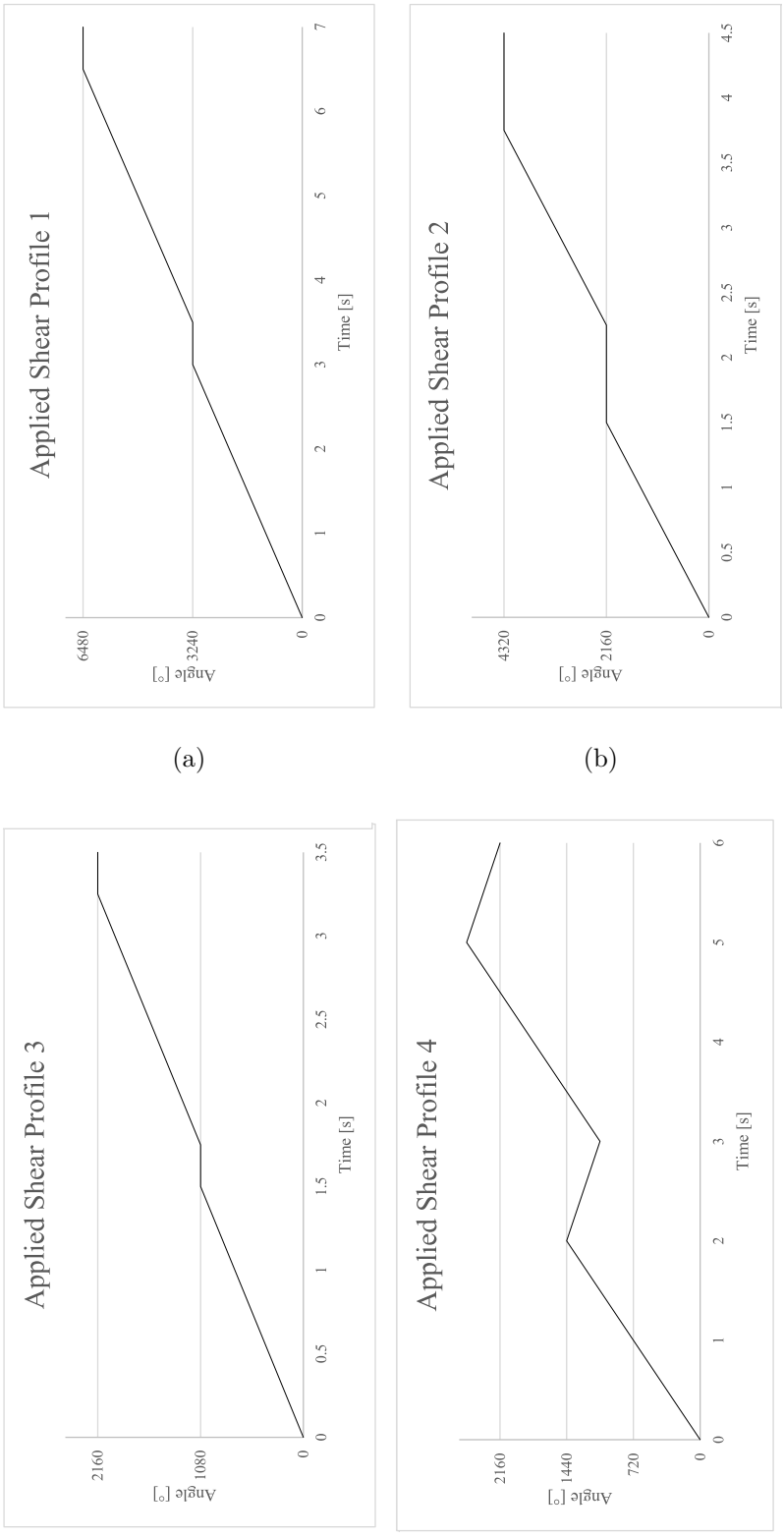

Figure 3.11.: **Graphical representation of the shear waveforms applied to low MW PBLG:** Each plot is representing two loops through the waveform. The angle displayed is the angle of the drive shaft relative to an arbitrary origin point set at the start of each loop. a) Applied shear profile 1. b) Applied shear profile 2. c) Applied shear profile 3. d) Applied shear profile 4.

Table 3.2.: **Waveforms of shear applied to low MW PBLG:** Description of the waveforms used with the second generation motor for the application of a shear force to a low molecular weight PBLG sample.

Applied Shear profile 1		Applied Shear profile 2		Applied Shear profile 3		Applied Shear profile 4	
Time[a][s]	Angle[b][°]	Time[a][s]	Angle[b][°]	Time[a][s]	Angle[b][°]	Time[a][s]	Angle[b][°]
0	0	0	0	0	0	0	0
3	3240	1.5	2160	1.5	1080	2	1440
3.5	3240	2.25	2160	1.75	1080	3	1080

[a]: Time relative to the start of each loop.
[b]: Angle of the drive shaft relative to an origin point set at the start of each loop.

isopinocampheol (Santa Cruz Biotechnology inc.) were mixed in a 1 ml Eppendorf tube and left to dissolve overnight before being mixed thoroughly by centrifuge and inverting the sample multiple times. The sample was then loaded into a 5 mm first generation rheo-cell. All NMR measurements on this sample were carried out on a Bruker 500 MHz NMR spectrometer operating at 76.8 MHz with a spectral width of 3 kHz. Again both 1D experiments and "2D" stacked experiments were carried out on this sample, with 4 scans per FID for 1D experiments, and one scan per FID for 2D. A recycle delay of 1 s was used for both. The motor control used for these experiments involved a square wave profile developed in the AU scripting language. This script allowed the motor to be set to loop between two given revolutions per minute for two time periods. The conditions of each run are outlined in Table 3.3 and Figure 3.12.

3.3.2.3. Results and Discussion

The application of a shear force to sample of low molecular weight had a noticeable effect on the quadrupolar splitting observed in the deuterium NMR spectra. The spectra acquired without the application of any shear forces showed a quadrupolar

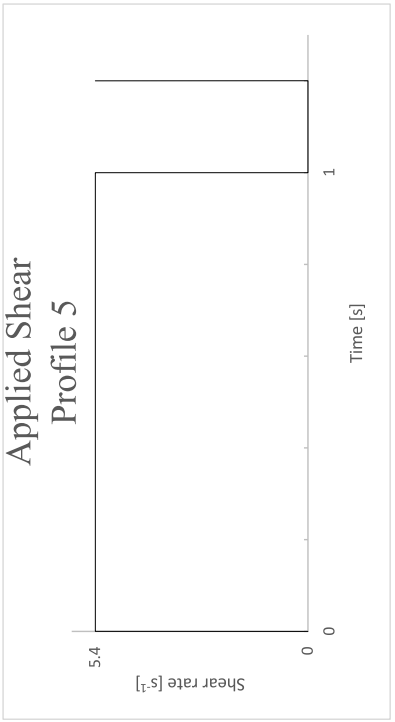

(a)

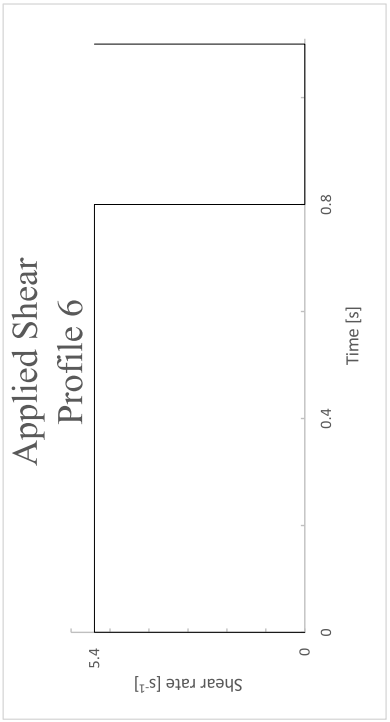

(b)

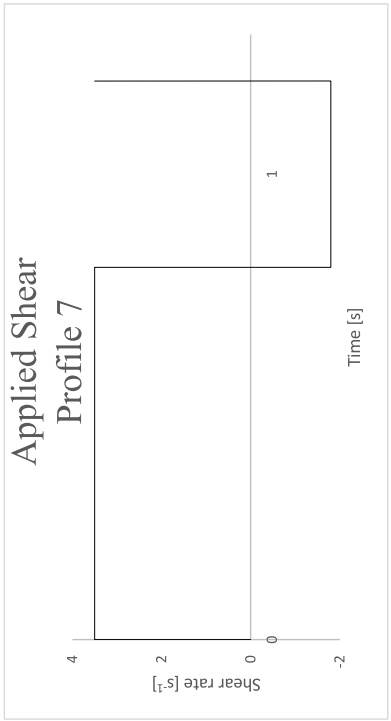

(c)

Figure 3.12.: **Graphical representation of three shear profiles applied to high MW PBLG:** a) Applied shear profile 5. b) Applied shear profile 6. c) Applied shear profile 7.

Table 3.3.: **Shear conditions applied to high MW PBLG:** Applied shear conditions used in high molecular weight PBLG experiments.

Applied shear profile	Average shear rate at top of wave [s^{-1}]	Average shear rate at base of wave [s^{-1}]	Time at top of wave [ms]	Time at base of wave [ms]
5	5.4	0	1000	200
6	5.4	0	800	300
7	3.5	-1.8	800	400

splitting of 399 Hz, much larger than that seen in the CTAB experiments, but not unexpected for a low molecular weight PBLG sample [56] (Figure 3.13).

The "2D" experiments carried out on this sample provided interesting results, with the range of different applied shear profiles each generating a unique quadrupolar splitting value, some with sharper peak shapes than others (the "2D" spectra is outlined in Figure 3.14, for information about the effect of each shear profile refer to Table 3.4). Unfortunately the lowest shear rate used, 18 s^{-1} gave a large spread single peak due to a large number of orientations present in the sample. Increasing the shear rate to 36 s^{-1} forced the sample to adopt a more uniform orientation, as measure by the peak width at half height, with a director angle of 62 $\pm$ 1° relative to the magnetic field. Further increasing the shear rate to 72 s^{-1} and 108 s^{-1} both had a similar effect of further decreasing the peak width at half height, and slightly increasing the quadrupolar splitting resulting from relative director angles of and 63 $\pm$ 1° and 65 $\pm$ 1°. The relatively small changes in the director angle of the PBLG were somewhat surprising at first, however it can be explained by considering both the high viscosity of the sample, and the torque which the spectrometers magnetic field will be exerting trying to align the PBLG with itself. As soon as the shear force was no longer applied, the quadrupolar splitting increased towards the maximum seen before the experiment had started. The final quadrupolar splitting measured without

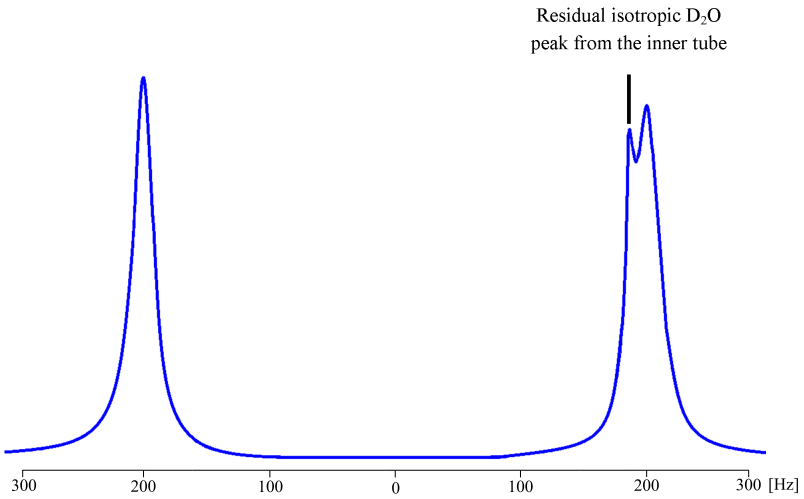

Figure 3.13.: **^{2}H spectrum of low MW PBLG:** 1D spectrum of low molecular weight PBLG in $CDCl_3$ showing a quadrupolar splitting of 399 Hz. A small isotropic D_2O peak is seen from a residual amount of D_2O in the inner tube.

shear showed that the samples director orientation had not yet completely re-aligned with the magnetic field, and still had a director angle of 6 $\pm$ 1°. This is due to the time needed before the sample will become completely aligned with the external magnetic field being greater than was allowed for in this experiment. Later experiments on other samples found the time required to be between 30 and 60 minutes.

The use of the applied shear profiles generated a variety of results. The results generated from the first shear profile is seen in Figure 3.15 where there is a clear pulsing of the peak intensity of the doublet. Closer inspection shows that there is a slight bulge in the center of the doublet appearing while the shear is ceased. The next shear profile applied lowered the shear force applied with the aim of lowering the gap between the two states, and can be seen in Figure 3.16.

Interestingly instead of decreasing the gap between the two possible states this eighth applied shear profile appeared to allow a second state in the middle of the quadrupolar doublet to increase in intensity as the experiment progressed (Figure

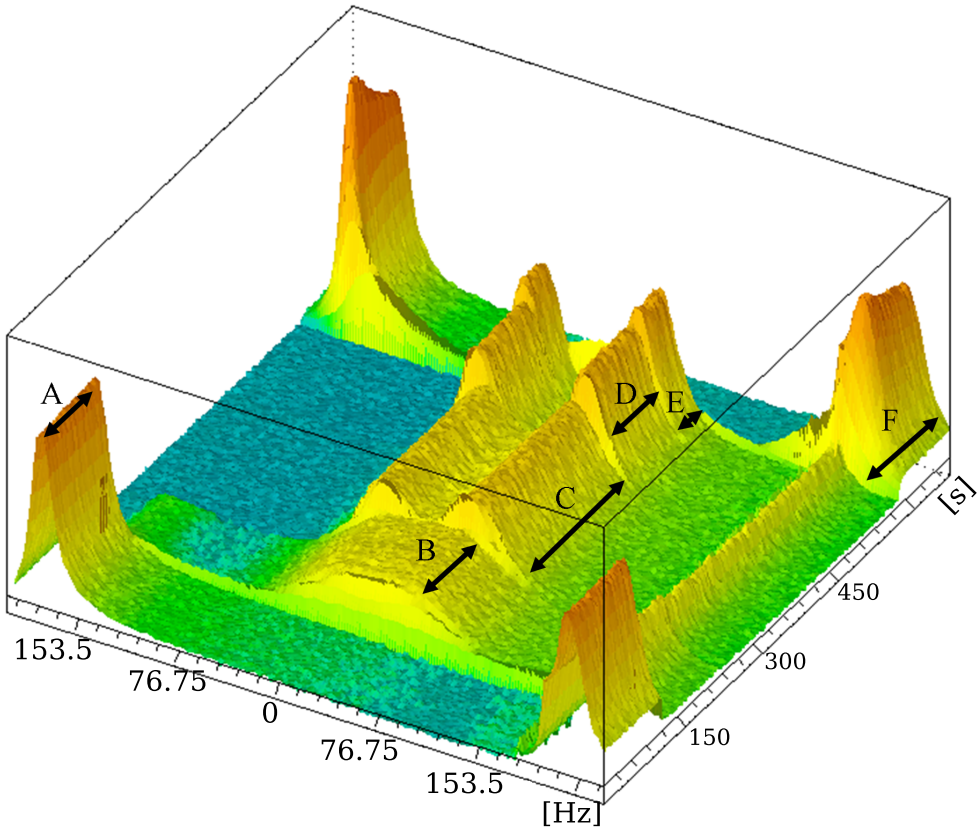

Figure 3.14.: **"2D" experiment of a variety of constant shear rates on the low molecular weight PBLG sample:** A: No shear applied. B: Average shear rate of 18 s^{-1}. C: Average shear rate of 36 s^{-1}. D: Average shear rate of 72 s^{-1}. E: Average Shear rate of 108 s^{-1}. F: No shear applied. The small peak that can be seen trailing on the right hand side is a D_2O peak from the residual amount in the inner tube.

Table 3.4.: **The effect of a number of applied shear profiles on low MW PBLG:** Detailed information for the effect that each shear rate had on the spectral properties of low molecular weight PBLG.

Avg. shear rate [s^{-1}]	Max shear rate [s^{-1}]	$\Delta\nu_Q$[a][Hz]	$\Delta\nu_{\frac{1}{2}}$[b][Hz]
0	0	401	20
18	26	Indistinguishable	130
36	51	70	50
72	103	81	30
108	154	90	28
0	0	394	20

[a]The quadrupolar splitting between the $CDCl_3$ doublet.
[b]The peak width at the estimated half height of the left peak of the quadrupolar doublet.

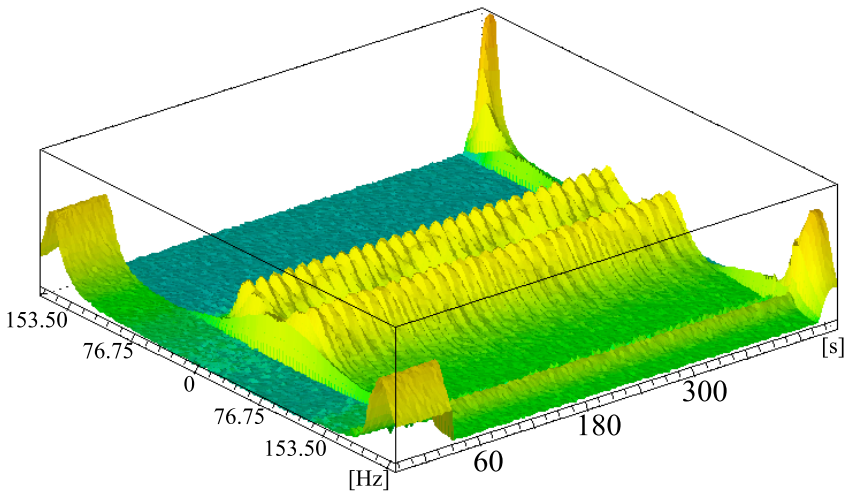

Figure 3.15.: **^{2}H spectra obtained with the shear profile of applied shear profile 1.**

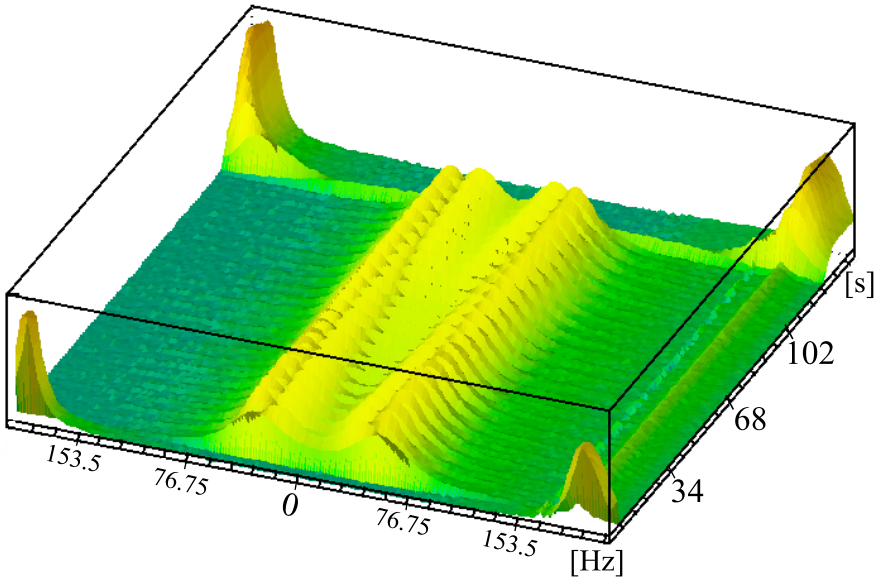

Figure 3.16.: **^{2}H spectra obtained with the shear profile of applied shear profile 2.**

3.16). When the quadrupolar splitting is measured for both doublets it is found that the initially seen outer doublet had a splitting of 90 Hz, corresponding to a director angle of 65°, while the developing inner doublet had a splitting of 54 Hz which corresponded to a director angle of 60°. The next shear profile investigated in the applied shear profile 3 cut down the time that the shear is halted for. The results of this experiment are displayed in Figure 3.17.

The results generated from shear profile 3 do appear to be the most homogeneous generated thus far using alternative wave forms, however there is still a clear pulsing of the intensity of the doublet peaks, indicating that another alignment is being formed during the delay period. Results from the final applied shear profile tested with the low MW PBLG are displayed in Figure 3.18.

This final shear profile involved a period in which the rotation of the shear motor was reversed. This shear profile has generated a large single bulge in the center of the quadrupolar doublet.

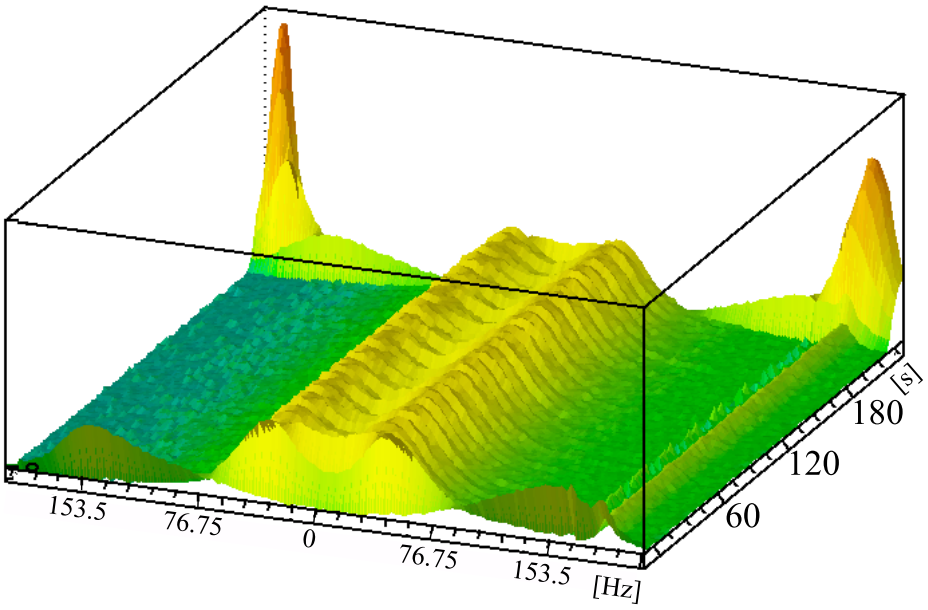

Figure 3.17.: **^{2}H spectra obtained with the shear profile of applied shear profile 3.**

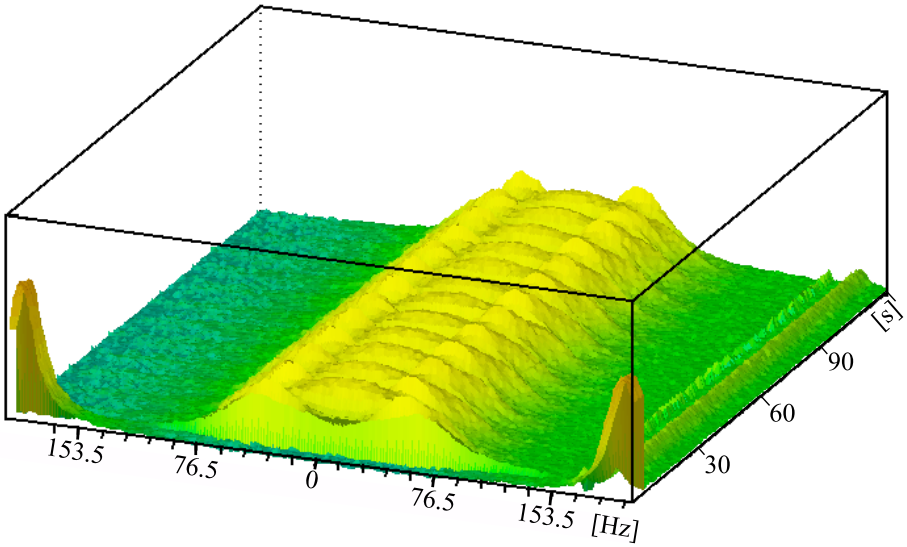

Figure 3.18.: **^{2}H spectra obtained with the shear profile of applied shear profile 4.**

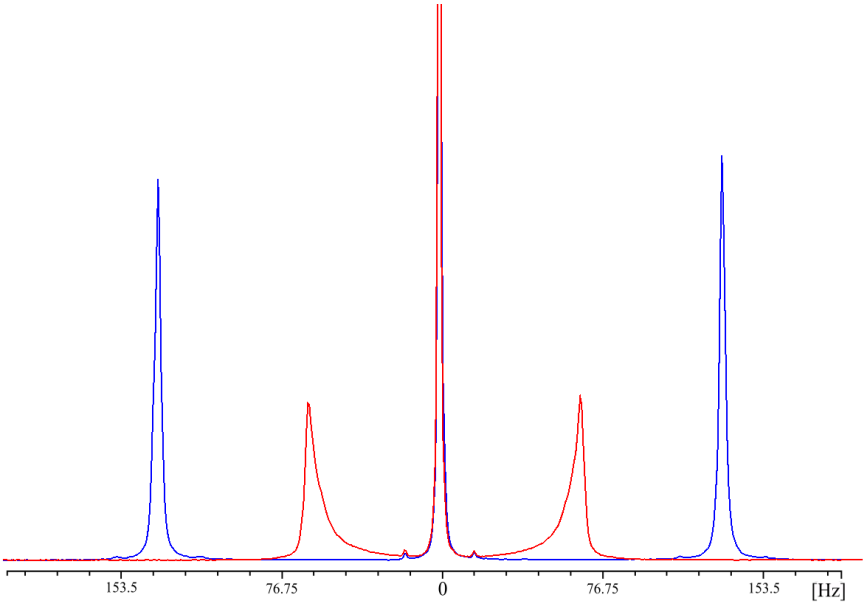

Figure 3.19.: **The effect of a shear force on the ^{2}H spectra of high molecular weight PBLG:** ^{2}H spectra of high molecular weight PBLG. Blue spectrum is the sample without the application of a shear rate. Red spectrum is the sample under shear at a rate of 90 s^{-1}. The large central peak is an isotropic deuterochloroform peak resulting from the lock solvent in the inner 3 mm tube.

The high molecular weight sample was found to behave in a very similar fashion to those trialed previously. When a sufficiently high shear rate is applied, the quadrupolar splitting is observed to reduce indicating that the director of the liquid crystal is being reoriented from parallel with the magnetic field to another orientation. This is demonstrated in Figure 3.19 with a constant average shear rate of 90 s^{-1} causing the quadrupolar splitting to be reduced from 261 $\pm$ 0.2 Hz to 125 $\pm$ 0.2 Hz indicating a liquid crystal director angle of 83° $\pm$ 0.4°.

The overall goal of maintaining stable liquid crystal orientations had been hard to obtain with the lower molecular weight PBLG sample when pulsed shear profiles were used. The use of a number of steady shear rates on the high molecular weight sample was however much more fruitful, with Figure 3.20 showing the results obtained when a shear rate of 5.4 s^{-1} was applied for 1 s before the shear was halted for 0.2 s.

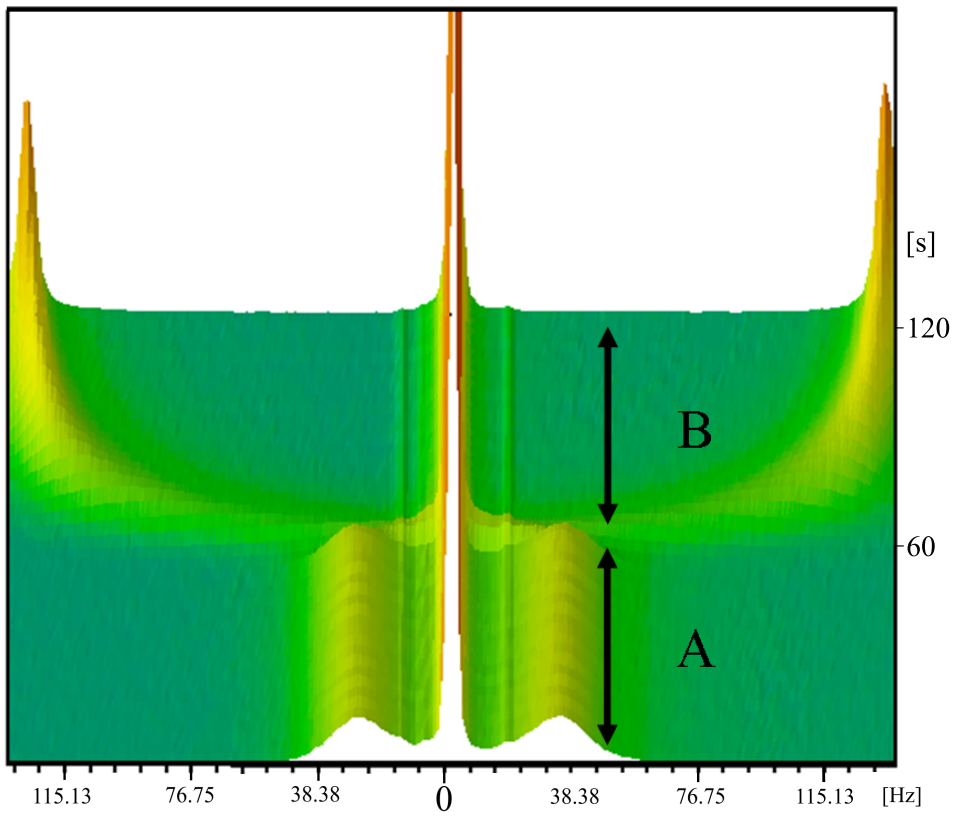

Figure 3.20.: **The effect of applied shear profile 5 on the ^{2}H spectra of high molecular weight PBLG:** ^{2}H spectrum of high molecular weight PBLG. A) Sample under applied shear profile 5 . B) No shear force applied, sample relaxing back to equilibrium state. Note: The large central peak is due to the deuterochloroform located in the inner 3 mm tube.

This shear rate caused the quadrupolar splitting to reduce to 62 ± 0.2 Hz from 260 ± 0.2 Hz when no shear was applied, which corresponds to a director angle of 65 ± 1°.

Decreasing how long the sample is sheared for in each loop and increasing the delay between the shear cycles resulted in the stability of the quadrupolar doublet dropping. It can be seen in Figure 3.21 that the doublet intensity appears to pulse along the time axis. This will likely be the result of multiple alignments of the liquid crystal director being present in the sample (a secondary set of peaks cannot be identified, but the decrease in intensity of the main peak would require the population buildup of another alignment). This shear profile resulted in a director angle of 65 ± 0.5°.

Decreasing the shear rate further to 3.5 s^{-1} and setting shear reversed in place of the break in shear resulted in a much poorer quality spectra where there are clearly two alignments present. It can be seen in Figures 3.22 and 3.23 there is one well resolved quadrupolar doublet with a splitting of 259 ± 0.5 Hz, and another poorly resolved doublet with a much smaller quadrupolar splitting of 40 ± 5 Hz. These splittings correspond to director angles of 29 ± 0.5° and 55 ± 5°.

3.3.2.4. Conclusion

Monitoring of the ^{2}H NMR spectrum of each of the PBLG samples has clearly shown that applying a shear force will cause the liquid crystal's director to reorient from parallel with the external magnetic field. The angles between the director of the liquid crystal and the magnetic field can once again be calculated by using the $|3cos^2 - 1|$ described earlier in Chapter 2.5

The use of samples with different molecular weights of PBLG showed that there is a large difference in the maximum quadrupolar splitting observed, as was encountered in prior work by Marx and Theile [56].

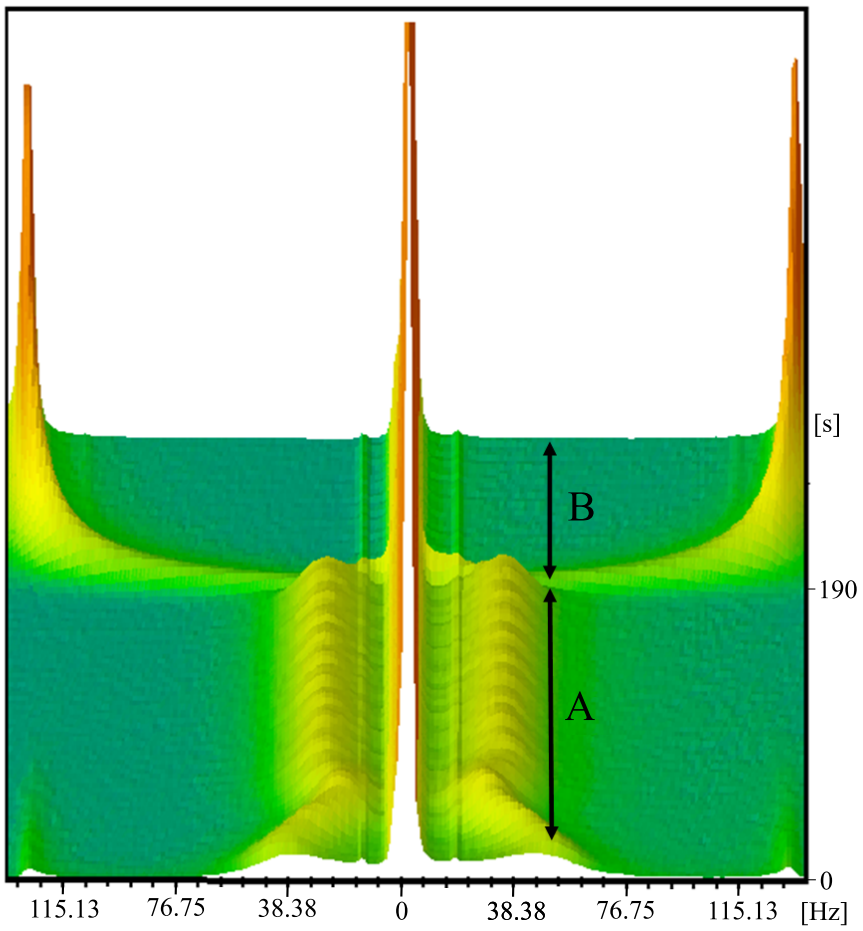

Figure 3.21.: **The effect of applied shear profile 6 on the ^{2}H spectra of high molecular weight PBLG:** ^{2}H spectrum of high molecular weight PBLG. A) Sample under applied shear profile 6. B) No shear force applied, sample relaxing back to equilibrium state. Note: The large central peak is due to the deuterochloroform located in the inner 3 mm tube.

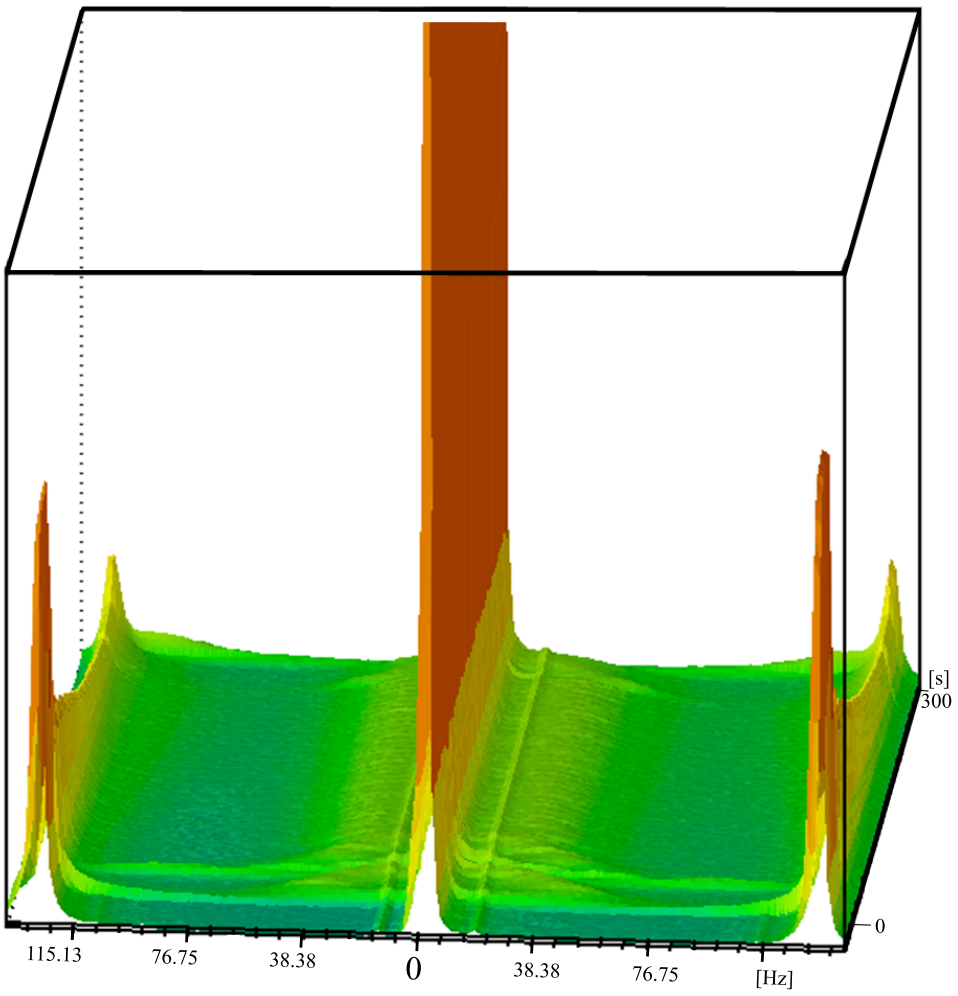

Figure 3.22.: **The effect of applied shear profile 7 on the ^{2}H spectra of high molecular weight PBLG:** ^{2}H spectrum of high molecular weight PBLG. Sample under applied shear profile 7. Note: The large central peak is due to the deuterochloroform located in the inner tube.

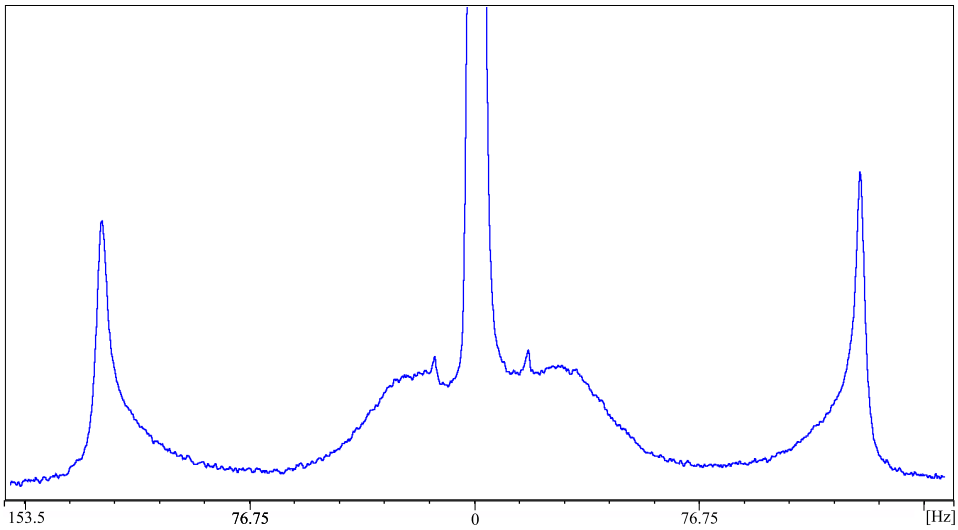

Figure 3.23.: **1D slice showing ^{2}H spectrum of high molecular weight PBLG under shear profile 7:** 1D slice of the 2D ^{2}H experiment shown in Figure 3.22. High molecular weight PBLG whilst under applied shear profile 7.

The application of pulse shear profiles to both high and low molecular weight sample provided some interesting results. The noticeable pulsing of the peak intensity and multiple peaks which appeared in the spectra from the low molecular weight sample indicated that there was not single alignments being generated, but rather a mixture. This evolution is clearly an interesting soft matter problem ripe for further investigation. The application of applied shear profile 5 to the high molecular weight sample proved to be the most effective in generating a single alignment, similar to what has been seen with constant shear rate experiments. The use of pulsed shear profiles has shown that an additional number of orientations that are otherwise unobtainable with constant shear can be obtained.

3.3.3. Pf1 in D_2O

3.3.3.1. Introduction

Bacteriophage pf1 is a long rod-like virus roughly 850 nm in length and 4-6 nm wide. When samples containing pf1 are placed into a strong external magnetic

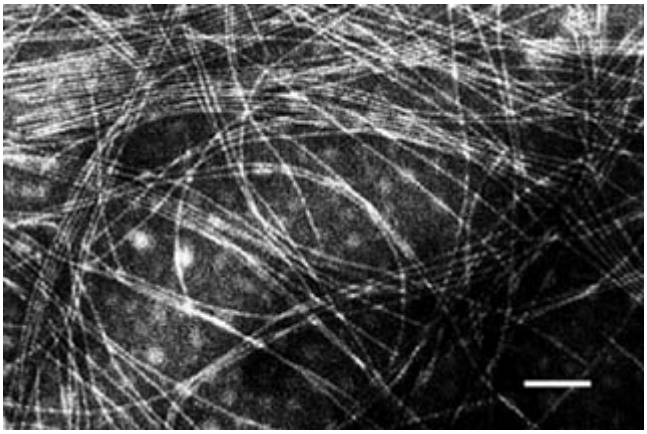

Figure 3.24.: **Electron microscopy image of pf1 bacteriophage sample.** Image reproduced from [64]

field the field will cause the long axis of the phage to align parallel with the field. If a suitably high concentration of pf1 is reached, the sample will take on a nematic liquid crystal phase where the director is aligned with the long axis of the phage. Pf1 bacteriophage is commonly used for the partial alignment of protein molecules for the capture of RDCs [48, 57, 58, 59, 60, 61, 62, 63]. As pf1 is heavily used in the capture of RDCs for protein NMR experiments, the ability to alter the alignment that the liquid crystal forms could prove to be beneficial for fine tuning results as well as possibly gaining more unique data sets. This system has been investigated under methods similar to that of the prior two liquid crystal systems, the angle of the liquid crystal's director is again monitored through ^{2}H NMR, with a deuterium probe being present as the D_2O solvent.

3.3.3.2. Experimental Method

Samples of pf1 without another solute were prepared to assess the viability of applying a shear force to pf1. 100 mL of potassium phosphate buffer was prepared for pf1 samples containing 90 mL of Milli Q water, 0.1285 g of KH_2PO_4(9 mM), 0.1005g of KCl (13.5 mM) and 0.02 g of NaN_3(3 mM) along with 10 mL of D_2O with a pH of 6.2. 0.33 mL of this buffer was then used along with a 0.17 mL of

Table 3.5.: **Constant shear rates applied to a pf1 sample.**

Avg. shear rate [s^{-1}]	Max shear rate [s^{-1}]	$\Delta\nu_Q$[a][Hz]	$\Delta\nu\frac{1}{2}$[b][Hz]
0	0	6.96	1.76
1.8	2.6	3.13	1.65
90	128	2.63	1.65
54	77	2.41	1.8
1.8[c]	2.6	0.75	3.4

[a] Splitting between the quadrupolar doublet in the ^{2}H spectra.
[b] Peak width at halt height of the left hand peak of the quadrupolar doublet.
[c] This shear rate was run at a lowered temperature of 279.4 K

a 50 mg/mL stock solution of pf1 to create a 0.5 mL sample with 17 mg/mL of pf1.

The sample of pf1 had a variety of constant shear rates applied to it as outlined in Table 3.5, while the ^{2}H NMR spectra were monitored. All experiments were carried out on a Bruker 500 MHz NMR spectrometer operating at 76.8 MHz with a spectral width of 3 kHz and, unless otherwise stated, at a temperature of 298 $\pm$ 1 K.

3.3.3.3. Results and Discussion

Measurement of the quadrupolar splitting seen when no shear is applied found that the maximum splitting was 6.96 Hz, as is seen in Figure 3.25 indicating that a nematic phase had indeed formed.

The application of low shear forces, have great impact on the alignment of the liquid crystal director. The stable quadrupolar splitting seen when an average shear rate of 1.8 s^{-1} can be found to relate to a director angle of 79°. The resultant 1D spectra for this shear profile can be seen in Figure 3.26.

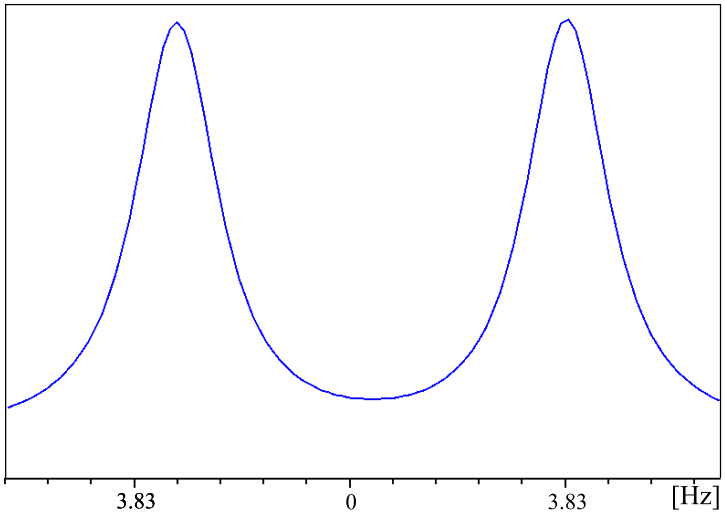

Figure 3.25.: **Spectrum obtained from pf1 sample while no shear forces are applied**

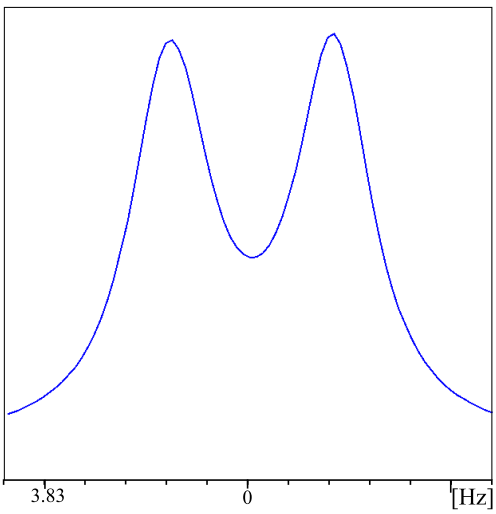

Figure 3.26.: **Spectrum obtained from pf1 sample while** under an average shear rate of 1.8 s^{-1}

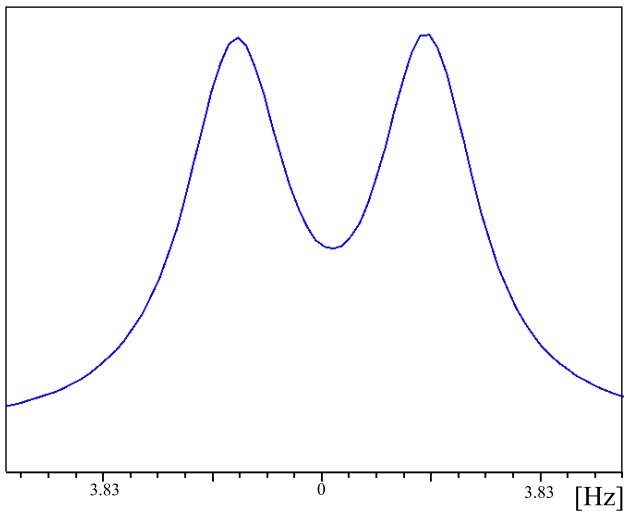

Figure 3.27.: **Spectrum obtained from pf1 sample while under an average shear rate of 90 s^{-1}**

The application of an average shear rate of 90 s^{-1} had a much larger shear rate applied in the hopes of orienting the director closer to 90°, however this shear rate appeared to generate a slightly smaller quadrupolar splitting than that of the prior experiment. This smaller splitting corresponded to a director angle of 73°. The resultant 1D spectra for this shear profile can be seen in Figure 3.27.

Decreasing the average shear rate to 54 s^{-1} resulted in a smaller quadrupolar splitting that all previous shear rates, and was found to correspond to a director angle of 71°. The resultant 1D spectra for this shear profile can be seen in Figure 3.28.

Finally, the temperature was lowered to 279 $\pm$1 K and a shear rate of 1.8 s^{-1} was applied in an attempt to decrease the rate that the quadrupolar splitting returns to the maximum post shear value. This proved to be the most interesting of the shear profiles attempted with a small quadrupolar splitting of only 0.75 Hz being seen. This splitting can be found to correspond to a director angle of either 50° or 59°(calculating which is challenging due to the proximity to the magic angle). The resultant 1D spectra for this shear profile can be seen in Figure 3.29.

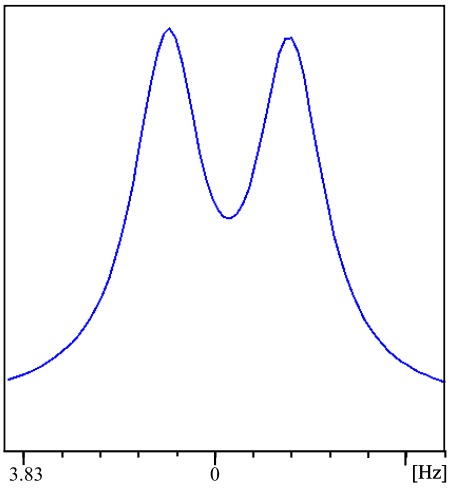

Figure 3.28.: **Spectrum obtained from pf1 sample while under an average shear rate to 54 s^{-1}**

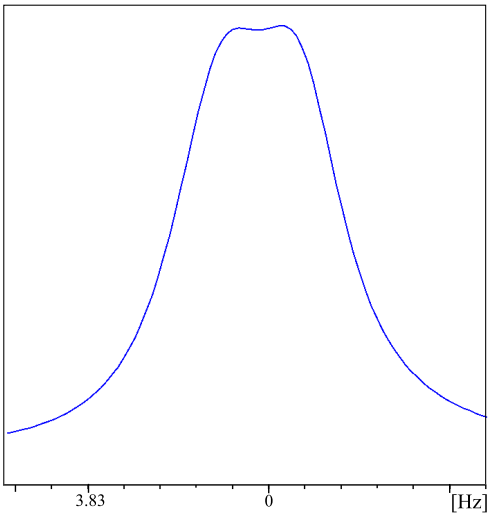

Figure 3.29.: **Spectrum obtained from pf1 sample while under an average shear rate of 1.8 s^{-1} at 279 K**

3.3.3.4. Conclusion

It is clear that pf1 exhibits changes in the quadrupolar splitting when a shear force is applied to a sample. Along with this, the changes seen appeared to follow what has been seen with the previously studied liquid crystal systems, indicating that the behavior is likely due to the same phenomena. The spectrum obtained while both changing temperature and shear rate demonstrated that it is possible to generate a vastly different alignment of the liquid crystal's director.

3.3.4. Conclusion

The three unique liquid crystal systems that have been investigated thus far have all clearly demonstrated changes in the ^{2}H spectra whilst a shear force is applied. Importantly the changes that have been seen all allow the director angle to be calculated by applying the $|3cos\theta^2 - 1|$ relationship that was described earlier in section 2.5. The ability to orient the director of the liquid crystals to unique orientations has also been demonstrated using both pulsed and static shear profiles. With this in hand the effects of reorientation on the spectra of molecules solvated in these anisotropic mediums can now be investigated.

3.4. Shear Stability of a Protein

3.4.1. Introduction

Proteins are macromolecules that have their secondary structure held together by relatively weak intermolecular forces. Given this, it could be easy to see how the application of a sufficiently high shear force could be able to break apart some of these bonds and cause the protein to denature. The denaturation of the target protein would ruin any further experiments as the native structure would no longer be accessible. Prior work by Jaspe and Hagen found that the shear rate

required to cause any significant changes in the structure of a small protein would be on the order of 10^7 s^{-1} [65]. While this is likely significantly more than any shear rate which is going to be applied in order to reorient a liquid crystal system, it is still important to investigate what effect the shear forces will have on the protein's structure. It is also important to note that a much larger non-globular protein is likely to have an increased susceptibility for denaturation under shear.

The target protein for this set of experiments is β-lactoglobulin (β-LG), which is the major protein component of bovine and ovine milk. β-LG is a largely globular protein with a significant proportion of its structure being constructed of beta sheet structure. At physiological conditions β-LG exists largely as a dimer and each monomer has a molecular weight of 18.4 kDa. It has also been reported that shear can cause aggregation into fibrils [66]. The formation of these larger scale structures would not allow the structure of each protein molecule to be studied in detail by NMR.

While determination of the full 3D structure of a protein is an involved process which relies on multiple NMR experiments being carried out and processed, it is possible to qualitatively monitor any changes in the structure through the ^{1}H NMR spectrum of the protein. Unfortunately it would be exceptionally difficult to make any exact claims about which regions of the protein had undergone any changes using only a ^{1}H NMR spectrum, however it will be simple to detect if changes have occurred.

3.4.2. Experimental Method

A β-LG 0.5 mL sample was prepared to a concentration of 2.2 mM in a 10mM phosphate buffer with 10% D_2O and pH adjusted to 2.4 using 20 μL of 1M HCl. The sample was mixed using a bench top vortex mixer before being loaded into a 5 mm first generation rheo-NMR cell. NMR experiments on this sample were carried out on a Bruker 500 MHz NMR spectrometer operating at 500.132 MHz

with a spectral width of 8012 Hz. A control ^{1}H spectrum was captured without the application of any shear forces with 64 scans. The sample now exposed to an average shear rate of 108 s^{-1} while a ^{1}H spectrum was again captured using 64 scans. This experiment was repeated for a final time using an average shear rate of 250 s^{-1}.

3.4.3. Results and Discussion

The spectra from each of the 3 experiments carried out on β-LG are displayed in Figure 3.30. There are no areas in any of the two sheared spectra that appear to have any major deviation from what is seen in the control experiment.

3.4.4. Conclusion

As can be clearly seen in the ^{1}H spectra displayed in Figure 3.30, there is no noticeable changes to the pattern of the spectra. While this is not a completely definitive study on the structural changes of a protein under shear, it is a strong indicator that there is likely very little, if any, change to the overall structure of β-LG whilst under shear rates on the order of 250 s^{-1}. It should be noted that a shear rate of 250 s^{-1} is much higher than any which will be used to reorient a liquid crystal system.

While the protein that will be introduced later is not tested using this same method it can be assumed that there will be little change in result due to the similar globular nature of the structures, and the results that were mentioned earlier by Jaspe and Hagen [65], as well as previous work by our group [67].

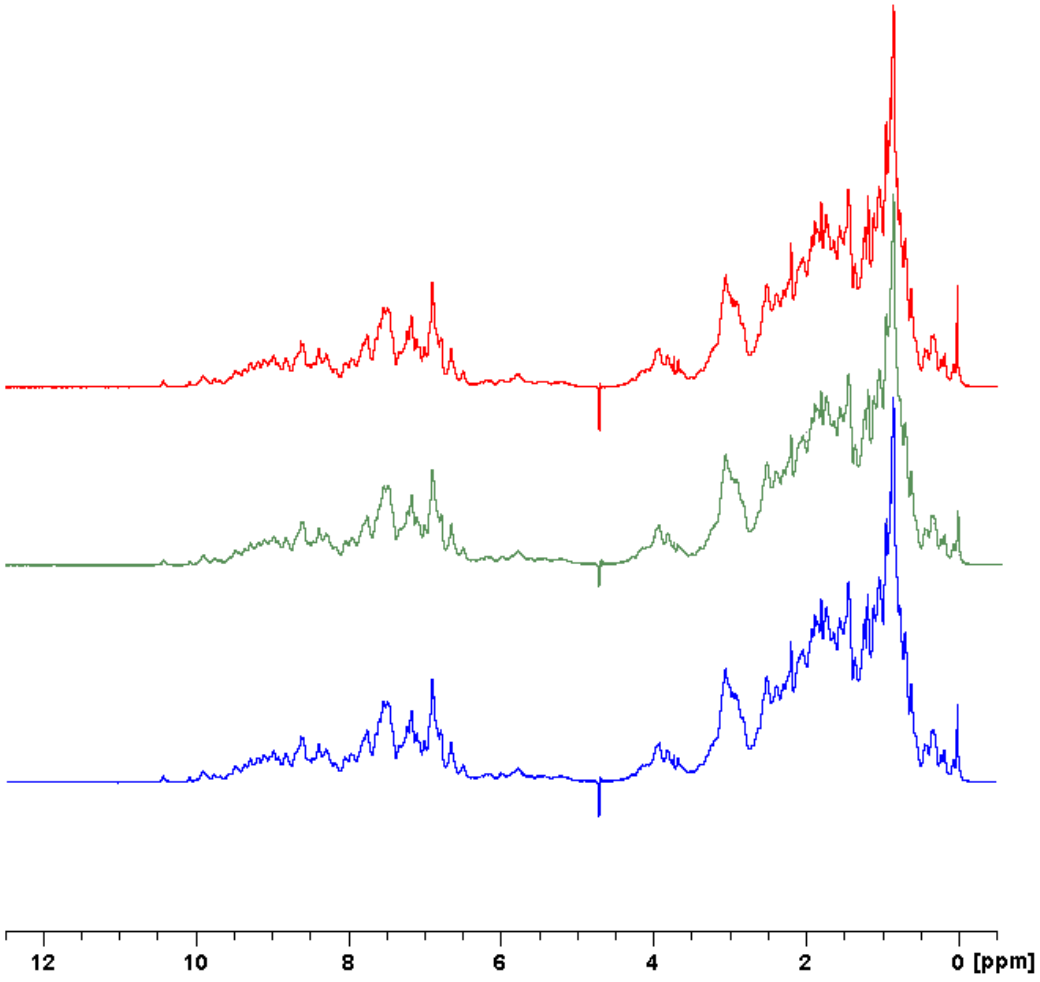

Figure 3.30.: **The effect of applied shear force on the structure of β-LG:** ^{1}H spectra of β-LG. Blue spectrum is under no shear force. Green spectrum is sheared at a rate of 108 s^{-1}. Red spectrum is sheared at a rate of 250 s^{-1}.

4. Isopinocampheol - A proxy for larger molecules

4.1. Introduction

High resolution NMR is one of the most commonly used techniques for studying the structures of organic molecules. The tool box of NMR techniques that have been largely available in the past such as J-couplings, the nuclear Overhauser effect, and chemical shifts are all exceptionally valuable in providing viable structural models. One potential downfall of these techniques however is their local nature, which can lead to problems where a break in the local connectivities may cause the structural model to be incomplete.

RDCs provide information which can be used to calculate an angle between a bond vector and the spectrometer's magnetic field. Unlike J couplings and NOEs they are not limited by internuclear distance. Therefore they can be of use for problems such as determining the relative conformation of remote stereocentres, improving on a structural model obtained from prior techniques.

RDCs have been applied for the refinement of small organic molecules by a variety of groups [68, 69, 70, 71, 72, 73, 74], but do not appear to have found widespread application yet.

$(1S, 2S, 3S, 5R)-(+)-$Isopinocampheol ($(+)-$IPC) is a chiral rigid small molecule which has been extensively studied by the Thiele group [56]. This molecule was

picked for investigation due to the rigid nature of the bridged ring structure, as well as the number of possible bonds from which RDCs could be captured from. The (−)−isopinocampheol enantiomer has also been investigated by this group and has been used to demonstrate that RDCs can be effectively used to differentiate between enantiomers [75]. The structure of both enantiomers of this molecule are shown in Figure 4.1 and Figure 4.2

For this investigation (+)−IPC was chosen to be investigated as a proxy for a larger more complicated molecule such as a protein. It was hoped that due to the less complicated spectrum, any effect that reorienting the liquid crystal may have on the RDC values would be easily discerned.

A coupled-HSQC experiment has been used here to probe the J and RDC values for each C-H bond vector present in this molecule. This is very similar to a standard decoupled HSQC experiment which generates a single peak for each unique (in terms of chemical shift) C-H pair. In contrast, the coupled HSQC allows the evolution of a doublet of peaks for each C-H pair, with the splitting between the peaks being equal to the RDC + J-coupling value. There are two basic alterations to the standard HSQC pulse sequence that can lead to this result, the first is the removal of the 180° proton refocusing pulse from between the INEPT and retro-INEPT steps which results in the doublet being spread along the ^{13}C (indirect) dimension. The second method, which was used in these experiments, is to simply remove the broadband decoupling pulse for the duration of the acquisition. This now results in the doublet developing in the ^{1}H dimension (direct). The pulse sequences that lead to each of these three outcomes are displayed in Figures 4.3, 4.4, and 4.5.

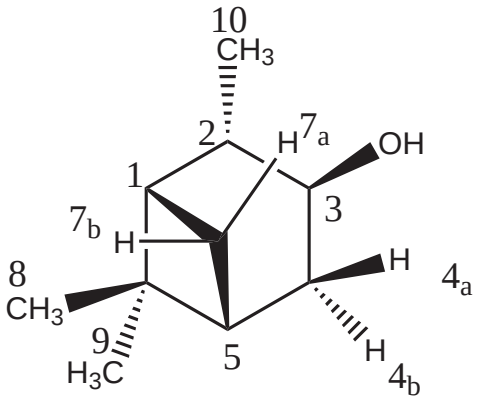

(1S,2S,3S,5R)-(+)-Isopinocampheol

Figure 4.1.: **Molecular Structure of (+)- Isopinocampheol:** Molecular Structure of (+)−Isopinocampheol with numbering used for assignment of the spectra

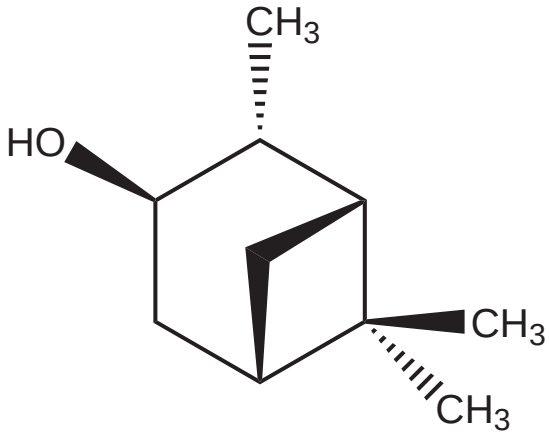

Figure 4.2.: **Molecular Structure of** (−)−**Isopinocampheol**

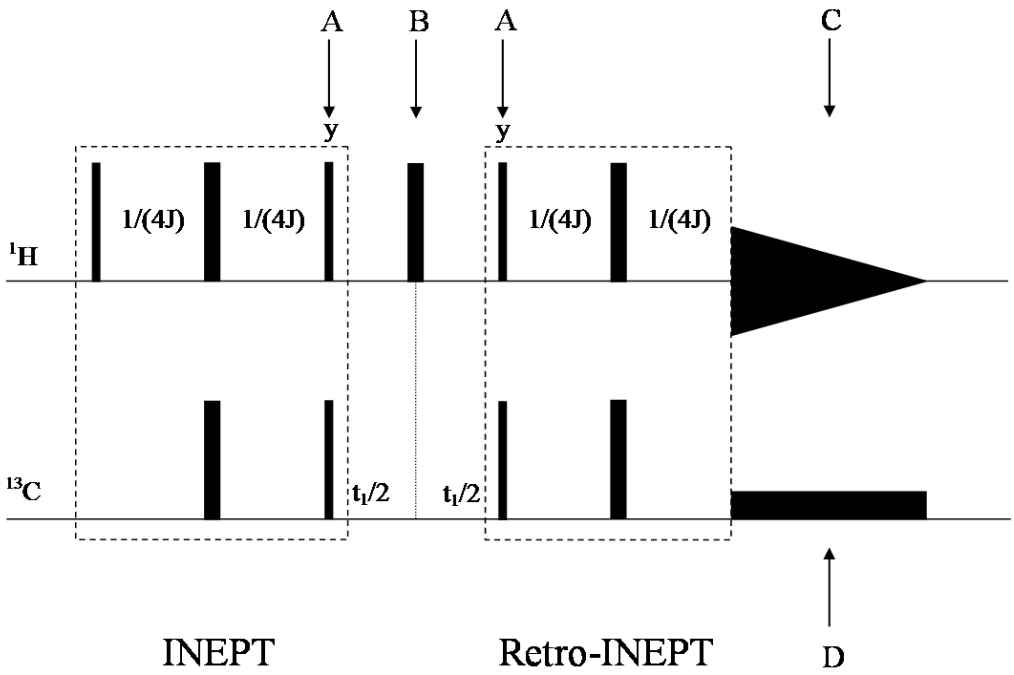

Figure 4.3.: **A HSQC Pulse Sequence:** The standard decoupled HSQC pulse sequence. Narrow bars and wide bars represent 90° and 180° pulses respectively along the x axis unless specified otherwise. Pulses A are the transfer steps where the magnetization is moved between the ^{1}H and ^{13}C nuclei. Pulse B removes the J coupling by refocusing the magnetization. C is the acquisition period on the ^{1}H channel. Pulse D is a long low powered pulse that decouples the ^{13}C nuclei by rapidly scrambling the magnetization on each ^{13}C nucleus while the ^{1}H signal is collected. [76].

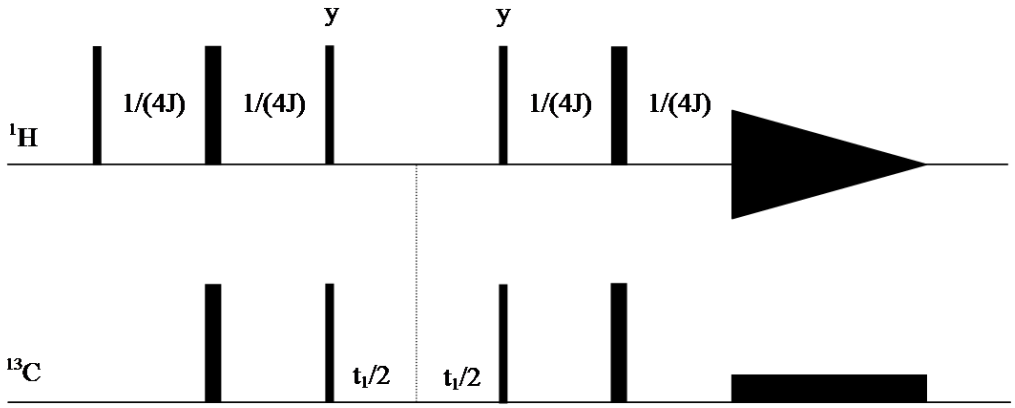

Figure 4.4.: **A coupled HSQC pulse sequence:** Narrow bars and wide bars represent 90° and 180° pulses respectively along the x axis unless specified otherwise. The removal of the 180° pulse between the INEPT and retro-INEPT periods allows the magnetization to continue to progress without refocusing and removing any J-coupling. This pulse sequence will result in any J-coupling or RDCs to be apparent along the indirect dimension [76].

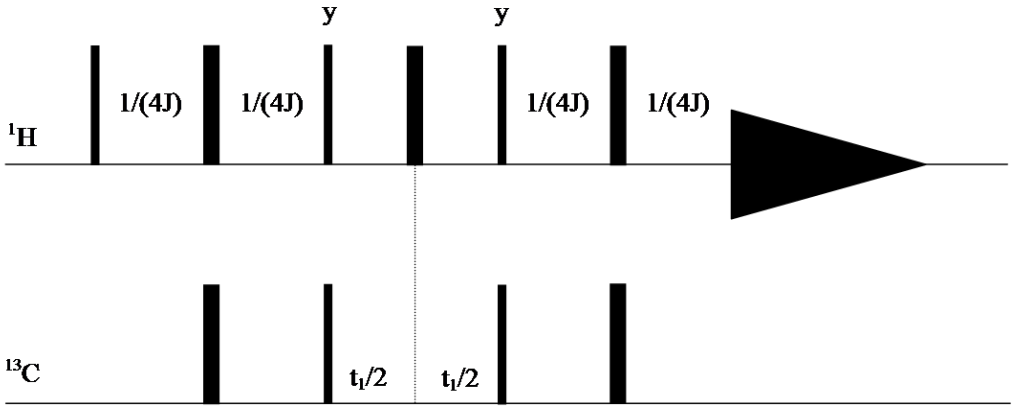

Figure 4.5.: **A coupled HSQC pulse sequence:** Narrow bars and wide bars represent 90° and 180° pulses respectively along the x axis unless specified otherwise. In this sequence the 180° pulse between the INEPT periods is returned and the broadband decoupling pulse on the F2 nuclei is removed during the acquisition. This allows both the J-coupling and RDC to develop in the direct dimension [76].

4.2. Experimental Method

An initial isotropic sample of (+)−IPC was prepared in order to determine the J-coupling values for each bond as well as allowing the assignment of the NMR peaks to each bond. A series of experiments were carried out in order to determine the peak assignments of (+)−IPC, including 1D ^{1}H and ^{13}C spectra, a decoupled HSQC spectrum, a coupled HSQC spectrum, a COSY spectrum, and a NOESY spectrum, each of which are provided in Appendix A. For these experiments a sample was created from 57.3 mg of (+)−IPC (Santa Cruz Biotechnology Inc.) and 0.633 mL of deuterochloroform (99.8% deuteration, SDS) were mixed in a standard 5 mm NMR tube before the experiments were carried out on a Bruker Avance spectrometer operating at a frequency of 500.13 MHz on the proton channel and 125.77 MHz on the carbon channel. The ^{1}H spectrum is displayed with assignments in Figure 4.6. The J-coupling values for each C-H bond of interest are displayed in Table 4.1.

A sample of (+)−IPC was now prepared with PBLG as the liquid crystal alignment medium using 55.8 mg of (+)−IPC, 147.3 mg of high molecular weight PBLG (150,000-300,000 daltons, Sigma Aldrich) and 0.633 mL of deuterochloroform. These were mixed together in a 1 mL Eppendorf tube on a vortex mixer before being placed into a first generation rheo-NMR tube. A sufficient volume of deuterochloroform was also added inside the inner 3 mm tube in order to allow a stable lock signal to be acquired (this gives a single ^{2}H peak which is unaffected by the presence of the PBLG liquid crystal). The homogeneity of the sample was now monitored by observing the peak width and relative height of the ^{2}H quadrupolar doublet from the deuterochloroform in the liquid crystal solution, with the same method of centrifugation that was outlined in Chapter 3.3.2.2 adopted when necessary. Before beginning each experiment on the sample a ^{2}H spectrum was captured without the application of any shear forces in order to determine the maximum possible splitting between the quadrupolar doublet.

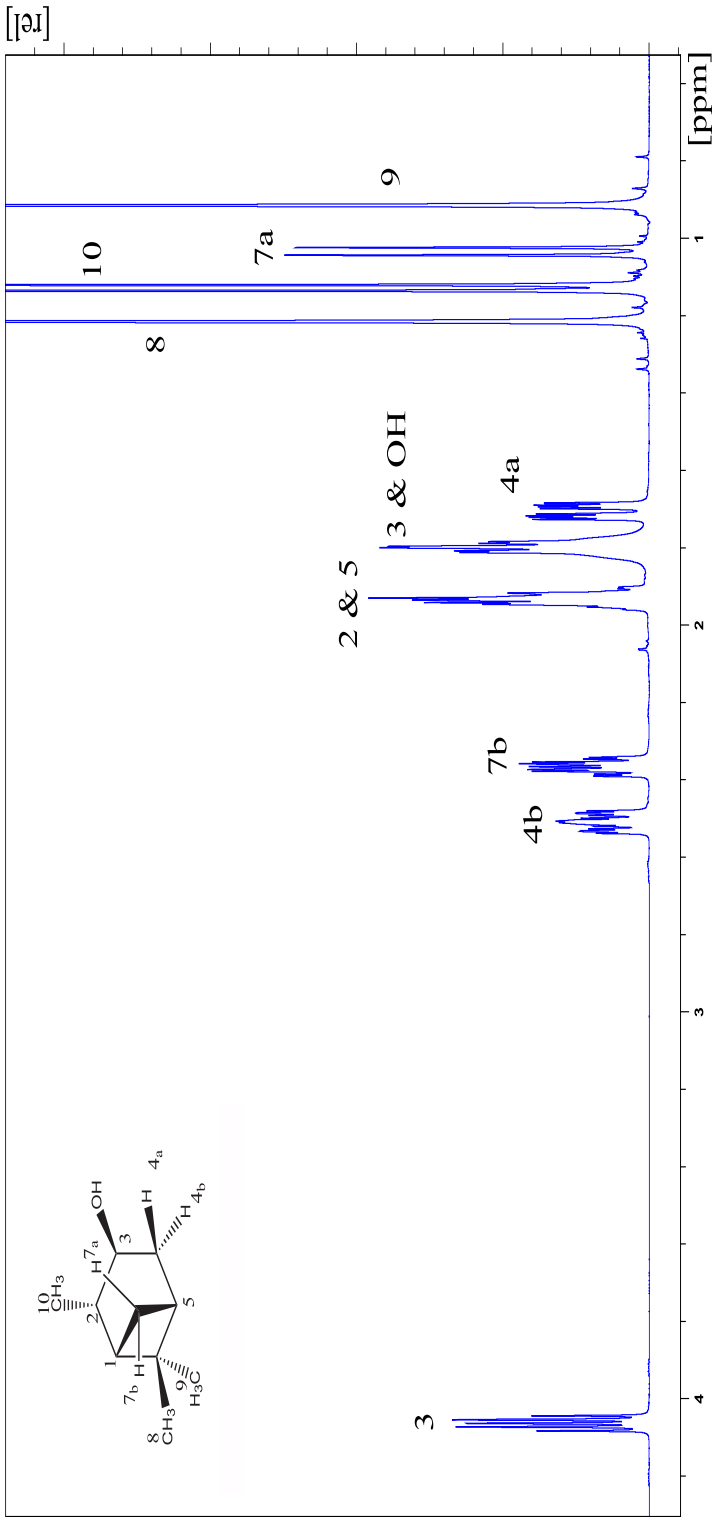

Figure 4.6.: **^{1}H spectrum of (+)-IPC:** ^{1}H spectrum of (+)-IPC in $CDCl_3$. Labels on molecular structure correspond to labeled peaks. Numbers under the peaks are the integral of each peak and correspond to the number of ^{1}H nuclei contributing to each peak

Table 4.1.: **J-Coupling values for (+)-IPC:** J-Coupling values for each labeled bond of (+)-IPC.

C-H Bond(s)	J-Coupling [Hz]
1	138.9 ± 0.1
2	125.7 ± 0.1
3	141.8 ± 0.1
4a	126.5 ± 0.1
4b	126.0 ± 0.1
5	137.7 ± 0.1
7a	136.8 ± 0.1
7b	144.5 ± 0.1
8	124.7 ± 0.1
9	122.9 ± 0.1
10	124.7 ± 0.1

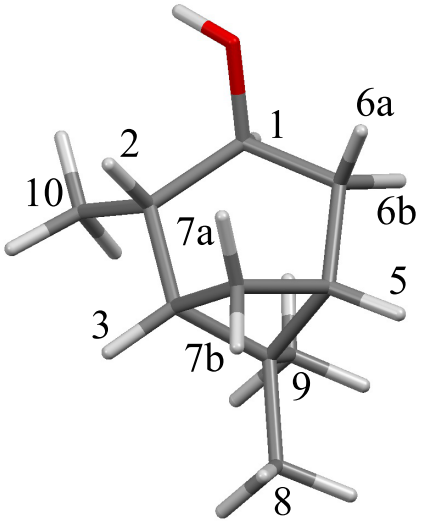

Figure 4.7.: **Computationally calculated model of (+)-IPC**

A variety of shear forces were then applied to the sample as outlined in Table 4.2. The quadrupolar splitting was monitored at each shear rate again using the ^{2}H spectrum which, as was noted in Chapters 2.5 and 3.3.2, allows the angle of the liquid crystal's director to be calculated. Once the quadrupolar splitting had reached a stable value, a coupled HSQC spectrum was acquired allowing the capture of the RDC and J-coupling values for each C-H bond vector in the molecule. Following the capture of the coupled HSQC a final ^{2}H spectrum is acquired to monitor if any changes in the alignment of the liquid crystal had occurred. This process is repeated for each unique shear rate, generating a number of data sets.

In order to obtain any meaningful data from the RDC values, a structural model of (+)-IPC had to be created. This was provided via computer modeling using a geometry optimized B3LYP/6-311+g (2d,p) calculation [77]. The calculated model is displayed in Figure 4.7. A coordinate file for the model can be found in Appendix B.

Table 4.2.: **Shear profiles applied to (+)-IPC:** Shear profiles applied to the (+)-IPC sample during acquisition of a coupled HSQC.

Avg. shear rate [s^{-1}]	Max shear rate [s^{-1}]	Max $\Delta\nu_Q$[a][b][Hz]	Initial $\Delta\nu_Q$[a][Hz]	Final $\Delta\nu_Q$[a][Hz]
0	0	276 ± 0.5	276 ± 0.5	276 ± 0.5
5.4	7.7	324.4 ± 0.5	76.2 ± 0.5	76.8 ± 0.5
9	12.8	385.6 ± 0.5	94.7 ± 0.5	98.9 ± 0.5
107.9	153.9	276 ± 0.5	133 ± 0.5	131 ± 0.5

[a] Quadrupolar splitting between the $CDCl_3$ doublet.
[b] Maximum quadrupolar splitting seen without any shear forces applied.

4.3. Results and Discussion

The effect of a shear force on the quadrupolar doublet seen in the ^2H spectra of liquid crystal solutions has already been clearly demonstrated in Chapter 3. However, to be useful it was necessary for the effect to be constant for the duration of the coupled-HSQC data collection. This could be verified by monitoring the splitting of the ^2H doublet. Figures 4.8, 4.9, 4.10, and 4.11 show an overlay of the ^2H spectra before and after each coupled-HSQC. Given there are not any significant changes in the splitting values as is noted in Table 4.2, it can be asserted that each RDC set obtained relates to a single set of alignments.

Promisingly, the RDC values obtained for each bond vector differed between all of the data sets obtained and are displayed in Table 4.3.

Each set of RDCs were fitted to the structural model using the RDC analysis program MSpin [78], and alignment tensors were found using the singular value decomposition method (a mathematical method for solving systems of simultaneous equations that may not have a single convergent answer. This is the method applied to solving for the alignment tensor seen in Equation 2.17). Each of these

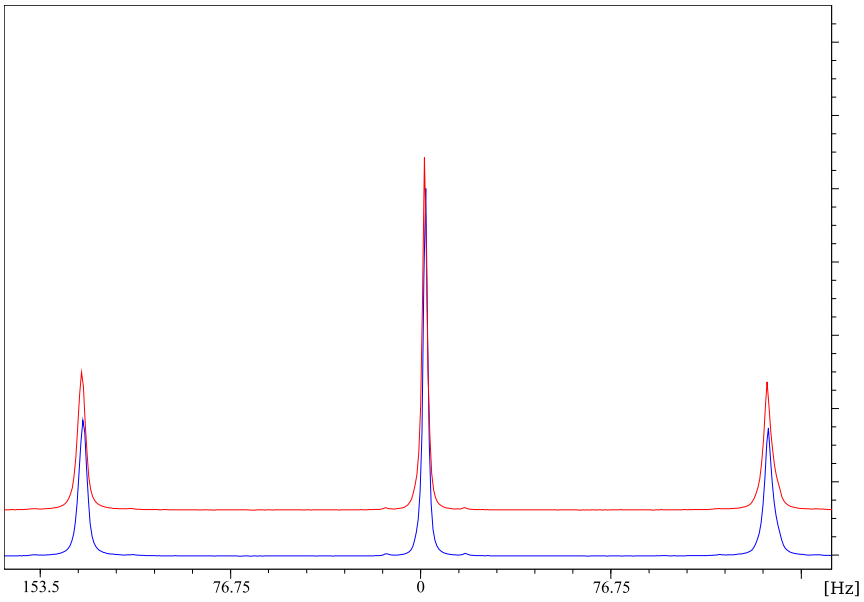

Figure 4.8.: **^{2}H spectra captured without the application of any shear forces:** ^{2}H spectra before and after coupled-HSQC experiment. The blue spectrum was captured immediately before the HSQC, the red spectrum was captured immediately after.

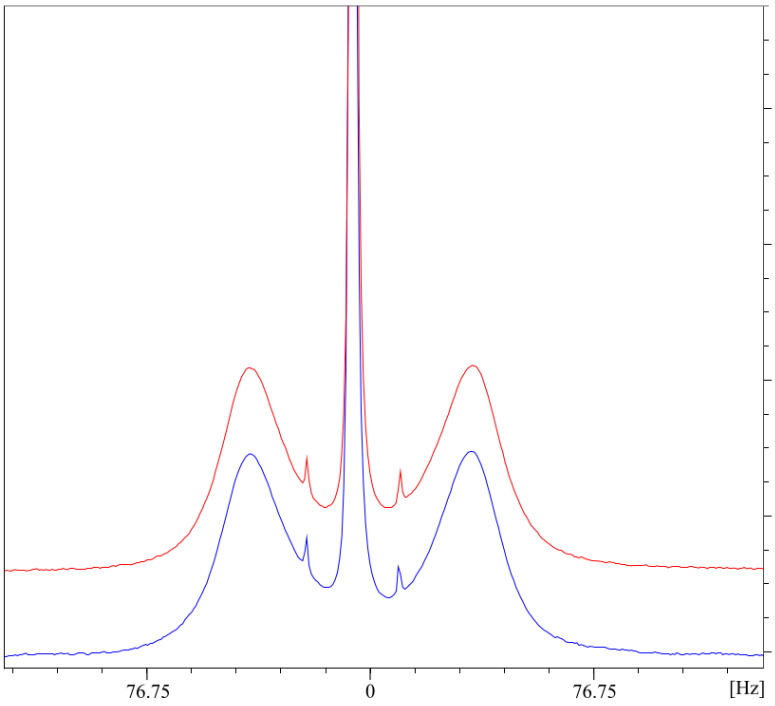

Figure 4.9.: **^{2}H spectra captured while under an average shear rate of 5.4 s^{-1}:** ^{2}H spectra before and after coupled-HSQC experiment while under an average shear rate of 5.4 s^{-1} . The blue spectrum was captured immediately before the HSQC, the red spectrum was captured immediately after.

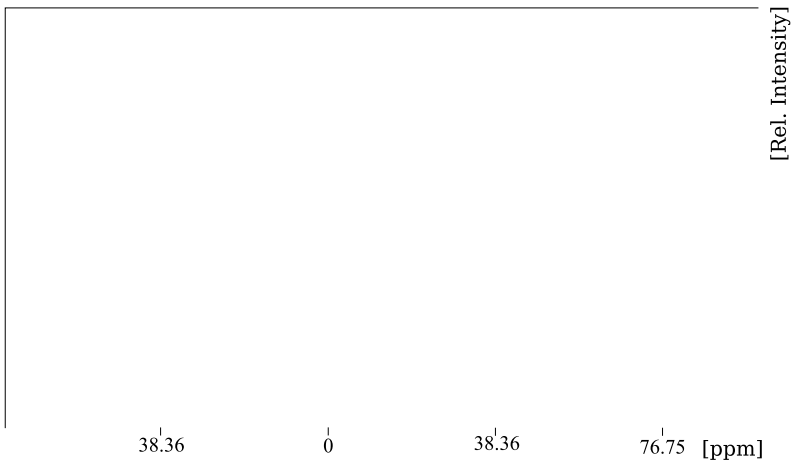

Figure 4.10.: **^{2}H spectra captured** while under an average shear rate of 9 s^{-1}**:** ^{2}H spectra before and after coupled-HSQC experiment while under an average shear rate of 9 s^{-1}. The blue spectrum was captured immediately before the HSQC, the red spectrum was captured immediately after.

Table 4.3.: **RDC values for (+)-IPC:** RDC values for IPC under various shear profiles.

C-H Bond	Avg. Shear rate of 0 s^{-1} RDC [Hz]	Avg. Shear rate of 5.4 s^{-1} RDC [Hz]	Avg. Shear rate of 9 s^{-1} RDC [Hz]	Avg. Shear rate of 107.9 s^{-1} RDC [Hz]
1	40.6 ± 0.1	−5.7 ± 0.1	−8.9 ± 0.1	−15.1 ± 0.1
2	−31.2 ± 0.1	1.0 ± 0.1	2.0 ± 0.1	2.0 ± 0.1
3	32.7 ± 0.1	−9.8 ± 0.1	−13.2 ± 0.1	−16.6 ± 0.1
4a	−25.2 ± 0.1	−1.5 ± 0.1	0.4 ± 0.1	−1.0 ± 0.1
4b	33.4 ± 0.1	−9.4 ± 0.1	−13.2 ± 0.1	−28.2 ± 0.1
5	−21.8 ± 0.1	7.0 ± 0.1	7.7 ± 0.1	11.2 ± 0.1
7a	−9.3 ± 0.1	9.4 ± 0.1	12.5 ± 0.1	17.6 ± 0.1
7b	−65.5 ± 0.1	−8.7 ± 0.1	−6.4 ± 0.1	−13.1 ± 0.1
8	0.6 ± 0.1	−3.5 ± 0.1	−5.7 ± 0.1	−8.5 ± 0.1
9	−26.8 ± 0.1	−0.4 ± 0.1	−1.0 ± 0.1	−1.0 ± 0.1
10	−23.1 ± 0.1	−4.4 ± 0.1	−5.8 ± 0.1	−4.1 ± 0.1

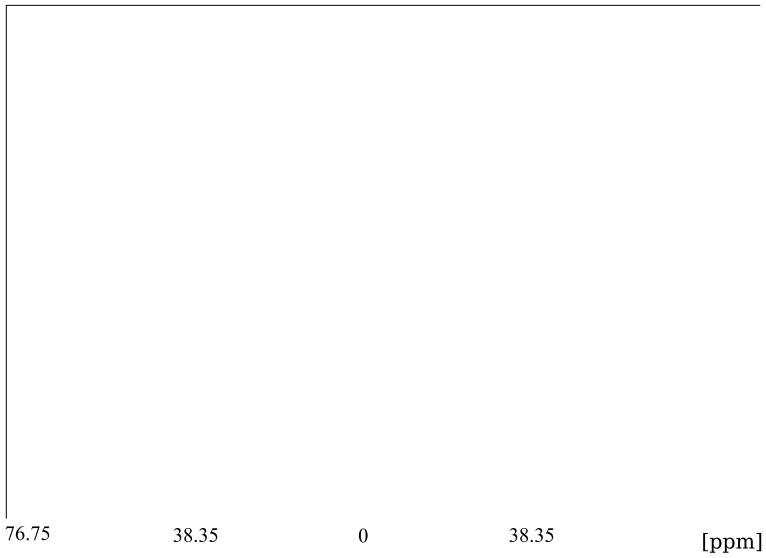

Figure 4.11.: **^{2}H spectra captured while under an average shear rate of 107.9 s^{-1}:** ^{2}H spectra before and after coupled-HSQC experiment while under an average shear rate of 107.9 s^{-1}. The blue spectrum was captured immediately before the HSQC, the red spectrum was captured immediately after.

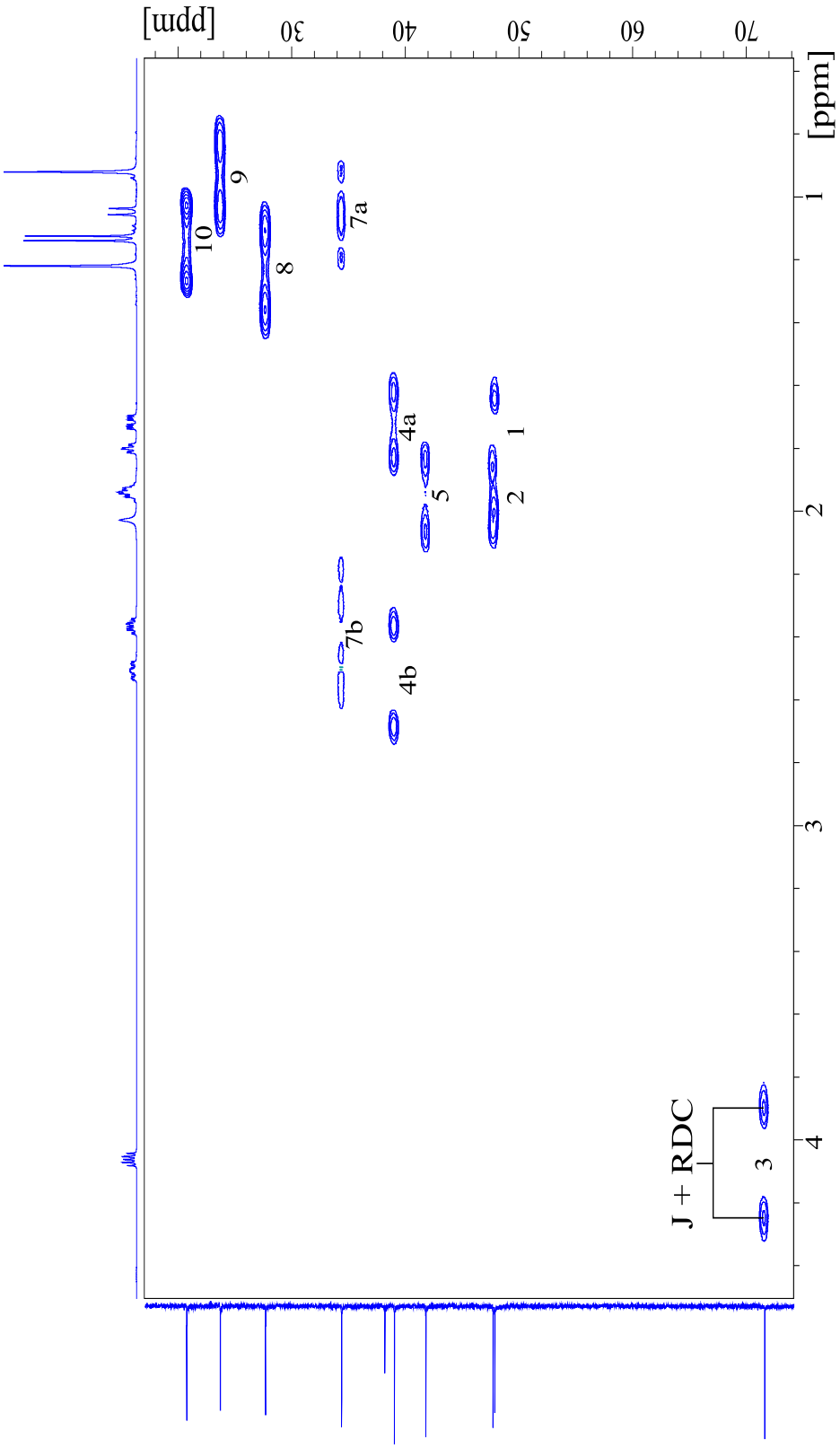

Figure 4.12.: **Coupled-HSQC obtained while no shear rate is applied.**

Table 4.4.: **RDCs obtained with no applied shear forces:** Measured vs. SVD calculated RDC results from MSpin under shear profile 19.

C-H Bond	Measured RDC [Hz]	SVD Calculated RDC [Hz]
1	40.6 ± 0.1	45.62
2	-31.2 ± 0.1	0.24
3	32.7 ± 0.1	14.24
4a	-25.2 ± 0.1	7.31
4b	33.4 ± 0.1	38.33
5	-21.8 ± 0.1	-8.88
7a	-9.3 ± 0.1	-32.21
7b	-65.5 ± 0.1	-33.20
8	0.6 ± 0.1	16.48
9	-26.8 ± 0.1	-5.38
10	-23.1 ± 0.1	-3.53

alignment tensors has an associated quality factor (Q), as described in Chapter 2.4.

It can be seen from Table 4.4 that the calculated RDC data do not match well to the measured RDC data obtained with no applied shear forces. The alignment tensor that was calculated from the set of measured RDCs is displayed in Equation 4.1. As could be expected from such poor fitting data the quality factor is very high with $Q = 0.675$.

$$\begin{bmatrix} 9.298 \times 10^{-4} & -1.773 \times 10^{-4} & 4.651 \times 10^{-5} \\ -1.773 \times 10^{-4} & -4.069 \times 10^{-4} & 2.873 \times 10^{-4} \\ 4.651 \times 10^{-5} & 2.873 \times 10^{-4} & -5.230 \times 10^{-4} \end{bmatrix} \tag{4.1}$$

Table 4.5 demonstrates the measured vs. SVD calculated RDC data for the RDCs measured whilst under an average shear rate of 5.4 s^{-1}, and demonstrates an

Table 4.5.: **RDCs obtained under an average applied shear rate of 5.4 s^{-1}:** Measured vs. SVD calculated RDC results from MSpin under an applied shear rate of 5.4 s^{-1}.

C-H Bond	Measured RDC [Hz]	SVD Calculated RDC [Hz]
1	-5.7 ± 0.1	-5.37
2	1.0 ± 0.1	2.15
3	-9.8 ± 0.1	-10.68
4a	-1.5 ± 0.1	1.61
4b	-9.4 ± 0.1	-7.91
5	7.0 ± 0.1	8.82
7a	9.4 ± 0.1	8.71
7b	-8.7 ± 0.1	-5.91
8	-3.5 ± 0.1	-1.22
9	-0.4 ± 0.1	3.06
10	-4.4 ± 0.1	-0.03

improved alignment between the calculated and measured RDCs. The alignment tensor that was extracted for this dataset is demonstrated in Equation 4.2, and has a much improved quality factor of $Q = 0.365$ associated with it.

$$\begin{bmatrix} -1.369 \times 10^{-4} & 2.810 \times 10^{-5} & -1.327 \times 10^{-4} \\ 2.810 \times 10^{-5} & -1.848 \times 10^{-5} & 3.390 \times 10^{-5} \\ -1.327 \times 10^{-4} & 3.390 \times 10^{-5} & 1.554 \times 10^{-4} \end{bmatrix} \tag{4.2}$$

The application of an average shear rate of 9 s^{-1} showed further improvement to the agreement between the measured and SVD calculated RDCs as is demonstrated in Table 4.6.

The alignment tensor extracted from the measured RDCs is demonstrated in Equation 4.3, and was found to have an associated quality factor of $Q = 0.329$

Table 4.6.: **RDCs obtained under an average applied shear rate of $9s^{-1}$:** Measured vs. SVD calculated RDC results from MSpin under an applied average shear rate of 9 s^{-1}.

C-H Bond	Measured RDC [Hz]	SVD Calculated RDC [Hz]
1	-8.9 ± 0.1	-8.52
2	2.0 ± 0.1	2.20
3	$-13.2\pm$	-13.06
4a	0.4 ± 0.1	2.52
4b	-13.2 ± 0.1	-12.06
5	7.7 ± 0.1	9.35
7a	12.5 ± 0.1	12.66
7b	-6.4 ± 0.1	-4.51
8	-5.7 ± 0.1	-2.59
9	-1.0 ± 0.1	3.84
10	-5.8 ± 0.1	0.21

Table 4.7.: **RDCs obtained under an average applied shear rate of 107.9 s^{-1}:** Measured vs. SVD calculated RDC results from MSpin under an applied average shear rate of 107.9 s^{-1}.

C-H Bond	Measured RDC [Hz]	SVD Calculated RDC [Hz]
1	-15.1 ± 0.1	-15.00
2	2.0 ± 0.1	1.50
3	-16.6 ± 0.1	-18.57
4a	-1.0 ± 0.1	6.30
4b	-28.2 ± 0.1	-21.95
5	11.2 ± 0.1	15.86
7a	17.6 ± 0.1	18.63
7b	-13.1 ± 0.1	-6.70
8	-8.5 ± 0.1	-3.72
9	-1.0 ± 0.1	5.62
10	-4.1 ± 0.1	-1.11

$$\begin{bmatrix} -2.173 \times 10^{-4} & 2.467 \times 10^{-5} & -1.467 \times 10^{-4} \\ 2.467 \times 10^{-5} & 1.012 \times 10^{-6} & 1.568 \times 10^{-5} \\ -1.467 \times 10^{-4} & 1.568 \times 10^{-5} & 2.163 \times 10^{-4} \end{bmatrix} \tag{4.3}$$

Increasing the average shear rate to 107.9 s^{-1} gave similar results to those obtained with an average shear rate of 1.8 s^{-1} and 9 s^{-1}. There is a good degree of alignment between the SVD calculated and measured RDCs for each C-H bond vectors displayed in Table 4.7.

The extracted alignment tensor generated by MSpin is demonstrated in Equation 4.4, and is found to have an associated quality factor of $Q = 0.343$.

$$\begin{bmatrix} -2.173 \times 10^{-4} & 2.467 \times 10^{-5} & -1.467 \times 10^{-4} \\ 2.467 \times 10^{-5} & 1.012 \times 10^{-6} & 1.568 \times 10^{-5} \\ -1.467 \times 10^{-4} & 1.568 \times 10^{-5} & 2.163 \times 10^{-4} \end{bmatrix} \tag{4.4}$$

The most obvious difference between each of these four sets of data is that between the data collected without the application of any shear forces and all others. There is very little agreement between the calculated and measured RDC values while under no applied shear forces which is then demonstrated again with the high quality factor of $Q = 0.675$. The three other sets of data showed significantly improved agreement between the calculated and measured RDCs, as well as improved Q factors. Although these Q factors are an improvement over the unsheared data set, they are still poor in comparison to reported data for this molecule [56].

The reasoning behind the poor quality factors for each data set are not understood. However, a possible explanation involves multiple orientations being present due to separation occurring over the duration of each experiment, although the ^{2}H results that were obtained do not provide sufficient evidence to substantiate this. In addition to this the low number of RDC data points for each shear profile will not allow any errors to be statistically removed which is likely to occur in larger molecules like a protein.

4.4. Conclusion

While most of the RDC data obtained in this chapter clearly does not allow suitable alignment tensors to be generated it is clear that the application of different shear forces has had an effect on the RDC values that are obtained. Notably the RDC data which was obtained under shear was of similar magnitude and order despite the difference in the shear forces applied, while also being

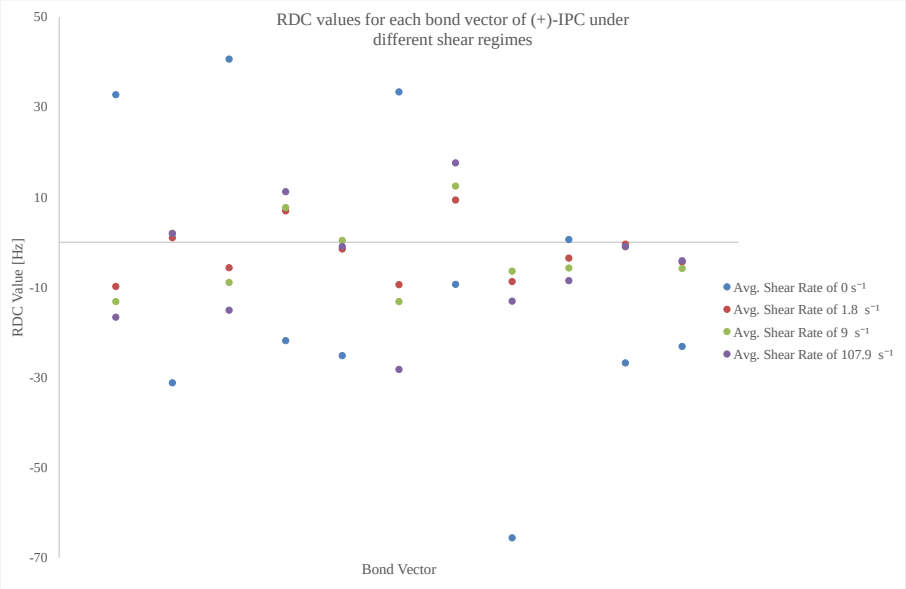

Figure 4.13.: **Comparison of (+)-IPC RDCs**: Comparison of RDC values for each bond in (+)-IPC under different shear profiles.

significantly different to that obtained without the application of any shear forces. These changes are best demonstrated in Figure 4.13.

While RDCs can be of use in determining the stereochemistry of small molecules, they are still yet to be widely applied (a Google Scholar search results in only 43 results for the strings “Residual Dipolar Couplings” and ”Small Organic Molecules”). The small number of internuclear vectors that can be probed with RDCs can potentially lead to results of limited quality, and this will only be exacerbated if adequate sample mixing and uniformity of alignments cannot be ensured. This, along with the already well proven and utilized NOE methods for determining stereochemistry, will likely limit the uptake of RDCs for small molecule analysis. The method should not however be completely discarded from the small molecule NMR toolkit as they can, in cases where limited or poor NOEs are available, still prove to be useful.

As this project intended to study the RDCs obtained from a protein system, where there are a significantly larger number of internuclear vectors present, instead of expending time on understanding and improving the results obtained in this chapter progress was made into a protein system which will be described next.

5. Ubiquitin

5.1. Introduction

Ubiquitin is a small (8.5 kDa) protein that, as its name suggests is found ubiquitously throughout eukaryotic cells and which consists of 76 amino acid residues. The structure and function of this protein has been extensively studied since its discovery in 1975 [79], and it has been found to be involved in a variety of biological processes including inflammation, translation, DNA repair, and endocytic trafficking, but most notably in protein degradation[80, 81, 82]. Two of the key structural features of ubiquitin are a C-terminus tail and the seven surface lysines. Each of these features allow the protein to be attached to a target protein through a process known as ubiquination, the discovery of which resulted in the Nobel Prize in Chemistry in 2004 being awarded to Ciechanover, Hershko, and Rose[83]. The process of ubiquination attaches one or more ubiquitin molecules to a protein which is targeted for degradation before the complex is then transferred to a proteasome where the degradation occurs. Due to the important role that ubiquitin plays in biological systems, and the ubiquitous nature, this protein has previously been extensively studied, resulting in a well-defined structural model being available both from X-Ray crystallographic methods (pdb entry: 1UBQ) [84], and solution state NMR [85, 86]. The well understood, relatively simple structure, along with the commercial availability of isotope labeled ubiquitin has resulted in ubiquitin being used as a model protein to display the effectiveness of

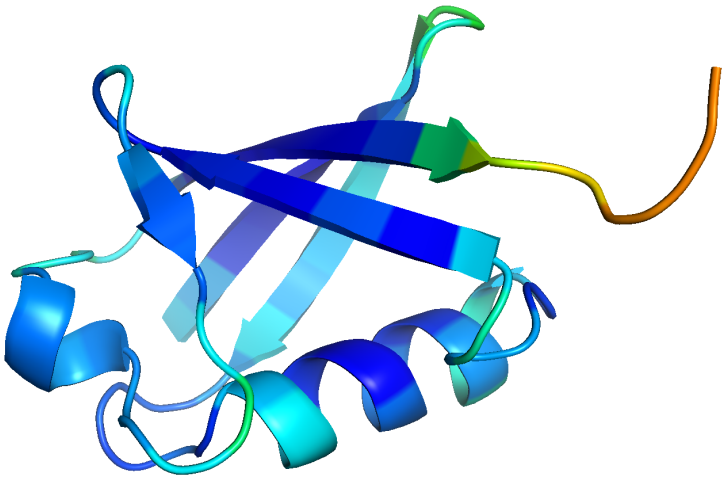

Figure 5.1.: **X-Ray crystallographic structure of Ubiquitin:** The structure obtained from X-Ray crystallographic study of ubiquitin. Resolution of 1.8 Å. [84]

new NMR techniques. In addition to this, ubiquitin has been used extensively to demonstrate the use of RDCs by various groups previously [57, 86, 87, 88, 89, 90]. Due to this information surrounding ubiquitin it was chosen as a model protein to investigate what effect the application of a shear force to the aligning phase may have on the RDCs that are captured.

5.2. Fitting of RDCs to a known structure

5.2.1. Introduction

Verifying that the RDCs captured are consistent with a known structure of ubiquitin is an important task. This verification process takes place through the calculation of an alignment tensor from experimentally measured RDC values and a previously known structure, before back calculating a set of RDC values from the alignment tensor and structure. If the original RDC values are consistent with the structure, the back calculated values should closely match the experimental values, and a low quality factor will be obtained. In the case of this study of ubiquitin the structure used for this calculation is an X-Ray crys-

tallographic structure with a resolution of 1.8 Å (1UBQ [84]). The verification process is even more important when multiple RDC datasets have been captured and utilized for a single target molecule, such as is the case here. The calculation of the alignment tensor can take place manually, as was described in Section 2.4, or more commonly by using a fitting program, such as MSpin [78] or PALES [48]. This fitting process yields a number of pieces of information, such as an alignment tensor, a set of back calculated RDCs, and a quality factor, Q. The RDC quality factor is commonly used as a cross-validation tool between a set of measured RDCs and a prior known structure. As an example, Q values for a high resolution structures of ubiquitin in published material are commonly accepted to be around 0.200 [91].

5.2.2. Experimental Method

100 mL of a pH 6.5 phosphate buffer which was used for all ubiquitin samples was prepared with 10 mM $KH_2PO_4$and 330 mM KCl. The pH was adjusted to 6.49 with 2 μL of 5 M HCl, and 20 μL of 5 M KOH. D_2O (99.9% deuteration, Cambridge Isotope Laboratories) was added up to 10% of the total volume to enable the spectrometer to gain a lock signal, as well as 0.0044g of trimethylsilyl propanoic acid (TSP) as an internal reference. 0.0285 g of NaN_3 was added as a bactericidal agent.

An isotropically tumbling ubiquitin sample was prepared from 0.001382 g of lyophilized ^{15}N labeled ubiquitin (Asla Biotech) and 0.3 mL of the aforementioned buffer. This sample was mixed thoroughly by inversion before loading into a standard 5 mm thin walled NMR tube (type 507-PP-7, Wilmad Glass Co.).

All NMR experiments in this section were carried out on a Bruker Avance 500 MHz NMR spectrometer operating at 500.13 MHz on the ^1H channel, and 50.68 MHz on the ^{15}N channel.

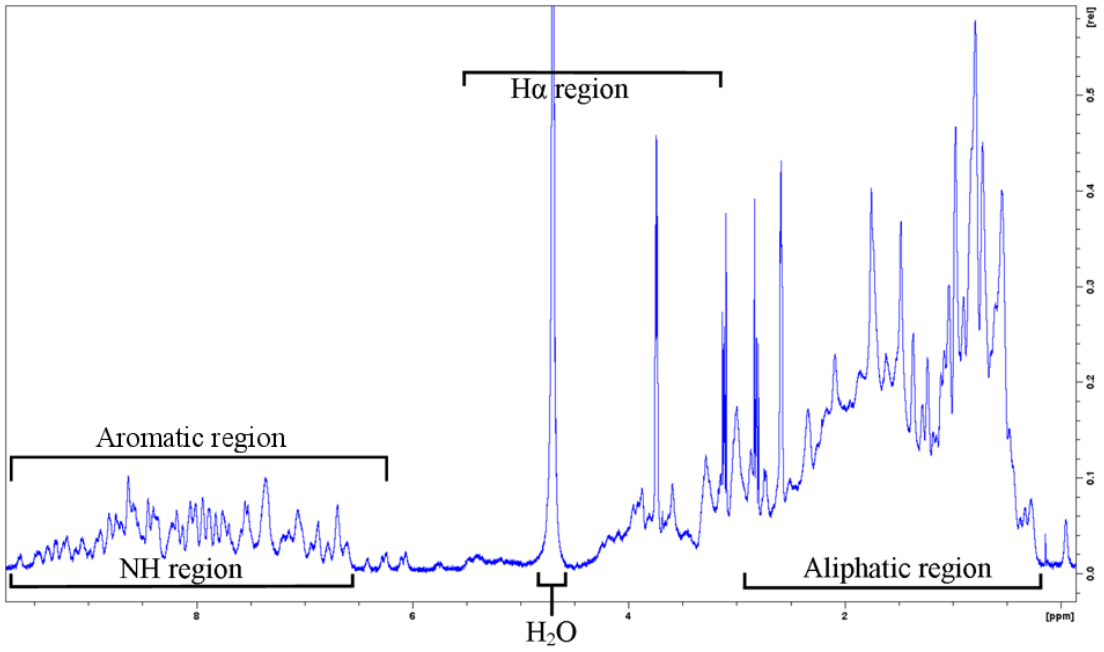

Figure 5.2.: **^{1}H spectrum of isotropic Ubiquitin:** Prepared in 10 mM phosphate buffer with regions of peaks labeled.

A 1D proton spectrum was captured using with a spectral width of 10.33 kHz, and 4 scans per spectrum and is displayed in Figure 5.2.

An HSQC experiment was then carried out with decoupling enabled, to allow each peak to be correctly labeled. This spectrum was acquired at 305 K with 2 scans per FID and a recycle delay of 1.2 seconds. The spectral width was set at 1.77 kHz for ^{15}N and 7 kHz for ^{1}H. The resultant spectrum is seen in Figure 5.3.

The IPAP-HSQC which was discussed in section 2.4 was now employed to capture the J-coupling values. The complete IPAP-HSQC had the spectral width set to 7 kHz for the ^{1}H channel and 1.77 kHz on the ^{15}N channel. Each FID used 4 scans per FID, and recycle delay of 1.2 seconds. As this is an interleaved spectrum, the FIDs are split using a built-in command in TopSpin 2.1 (Bruker BioSpin, Rheinstetten, Germany), 'SPLIT IPAP 2', which gives two resultant spectra, one with each N-H bond leading to an in-phase doublet, and the other an anti-phase doublet. The addition and subtraction of these spectra results in two spectra, one with the up field component of the doublet, and the other the corresponding down field component.

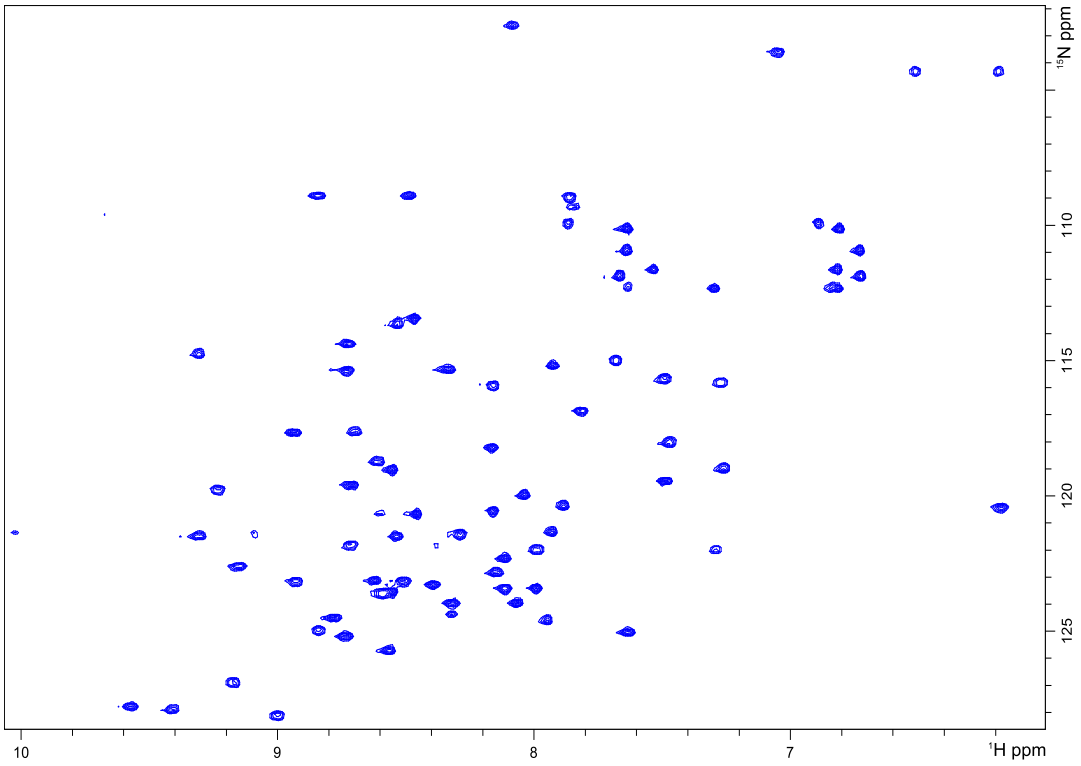

Figure 5.3.: **^{1}H -^{15}N HSQC of isotropic Ubiquitin:** Prepared in 10 mM phosphate buffer.

Next an anisotropically tumbling sample was next prepared using 0.00230 g of ^{15}N labeled ubiquitin, 0.33 mL of the phosphate buffer used previously, and 0.17 mL of 50 mg/mL bacteriophage Pf1 (Asla Biotech.). The sample was mixed with a vortex mixer before being loaded into a second generation rheo-NMR tube (as was described in Section 3.1.2).

Several shear profiles were applied to the sample while an IPAP-HSQC was recorded (outlined in Table 5.1). In addition to the IPAP-HSQC, a two ^{2}H spectra were recorded, one before the IPAP-HSQC, and one after. These ^{2}H spectra are used to calculate the liquid crystal's director angle, as well as ensuring that the sample is homogeneous for the duration of the IPAP-HSQC experiment.

The RDC values are extracted for each of the different shear profiles from each IPAP-HSQC spectrum. The extracted RDC values are then processed into an input file for PALES [48]. PALES requires both this input file and a structural

Table 5.1.: **Shear profiles applied to the anisotropic Ubiquitin sample**

Avg. shear rate [s^{-1}]	Max shear rate [s^{-1}]
0	0
17.98	25.66
215.82	307.88
0	0
1.80	2.57
0.72	1.03
71.94	103.63

model in-order to calculate an alignment tensor and other characterizing information that is extracted from the RDCs. The structural model that was used for these ubiquitin experiments is an X-ray crystallographic structure with a resolution of 1.8 Å (1UBQ)[84]. The input file and structural model are iteratively run through PALES, and RDC values that have poorer fits are removed in each iteration, until the values are largely in agreement. The values that have been removed are commented out in the input file with a '#'.

5.2.3. Results and Discussion

The first set of results from this set of experiments involved the capture of the J-coupling values for each of the N-H bonds present in the ubiquitin molecule. This was carried out by using an IPAP-HSQC which gives two component spectra, an in-phase component, and an anti-phase component, which are demonstrated in Figures 5.4, and 5.5. The anti-phase is then added to and subtracted from the in-

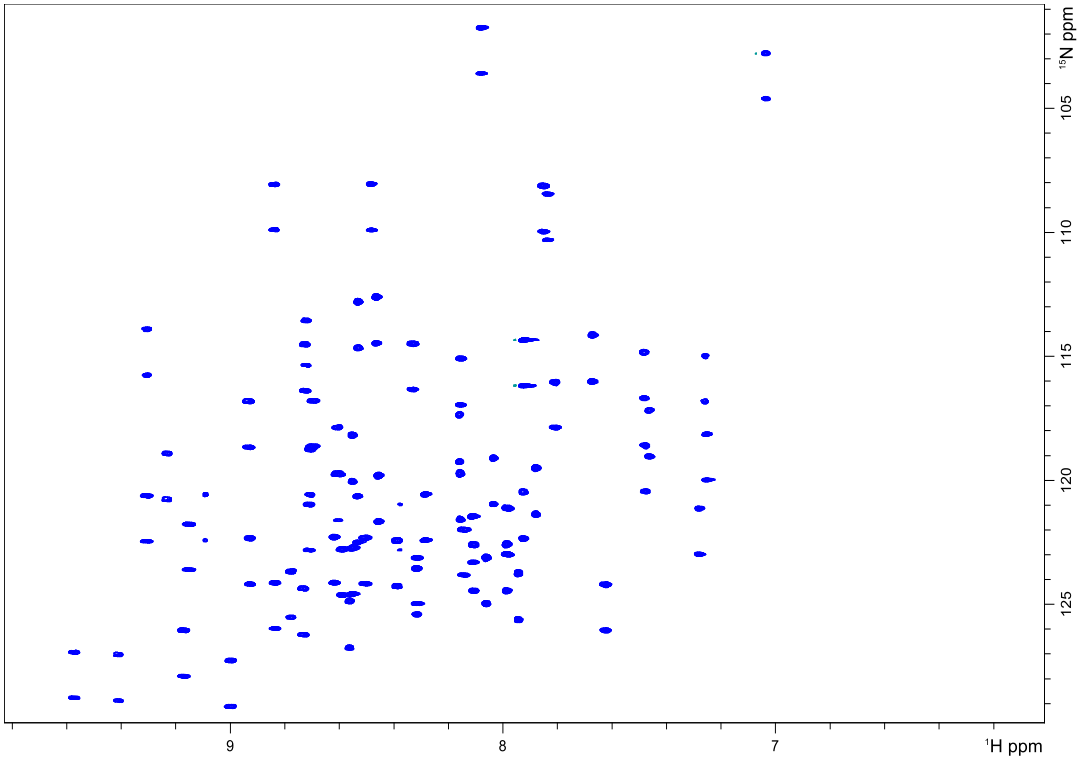

Figure 5.4.: **Isotropic Ubiquitin IPAP-HSQC In-phase component.**

phase spectrum resulting in two spectra, each of which contains one component of each doublet.

In the initial isotropic sample the J-coupling values were found as the difference in the F1 dimension location of each half of the doublet. The J-coupling values are given in Table 5.2.

Once the J-coupling had been determined, the RDC values from each of the different shear profiles could be extracted. An initial experiment was carried out on the anisotropically tumbling sample without the application of any shear forces, much in the same way that other groups have measured RDCs for proteins. The RDC values captured from this first experiment are shown in Table 5.3. The ^{2}H spectra (which are sensitive to the orientation of the liquid crystal director) that were captured before and after this experiment showed were found to have very little variation. As no shear forces were applied to this sample, it is assumed

Table 5.2.: **J-Coupling values for the N-H bonds of Ubiquitin**

Amino Acid	Residue Number	J-Coupling [Hz] [±0.05]	Amino Acid	Residue Number	J-Coupling [Hz][±0.05]
GLN	2	93.13	GLN	40	93.13
ILE	3	93.56	GLN	41	94.86
PHE	4	93.99	LEU	43	95.73
VAL	5	93.13	ILE	44	92.69
LYS	6	93.56	PHE	45	93.56
THR	7	94.42	GLY	47	93.12
LEU	8	94.42	ARG	48	93.13
LYS	11	94.42	LEU	50	96.16
THR	12	92.69	GLU	51	95.29
ILE	13	93.13	ASP	52	94.85
THR	14	93.56	ARG	54	95.73
LEU	15	95.30	THR	55	93.13
GLU	16	93.99	SER	57	93.99
VAL	17	93.99	ASP	58	98.76
GLU	18	93.13	TYR	59	95.73
SER	20	92.69	ASN	60	94.42
ILE	23	94.42	ILE	61	93.56
ASN	25	94.42	GLN	62	94.42
VAL	26	92.70	LYS	63	93.99
LYS	27	97.02	GLU	64	93.99
SER	28	96.59	SER	65	94.86
ALA	29	95.30	THR	66	92.26
ILE	30	94.42	LEU	67	93.99
ASP	32	94.42	HIS	68	95.29
LYS	33	93.99	LEU	69	93.56
GLU	34	90.96	VAL	70	94.43
GLY	35	93.99	LEU	71	96.59
ILE	36	91.39	GLY	76	93.56
ASP	39	94.86			

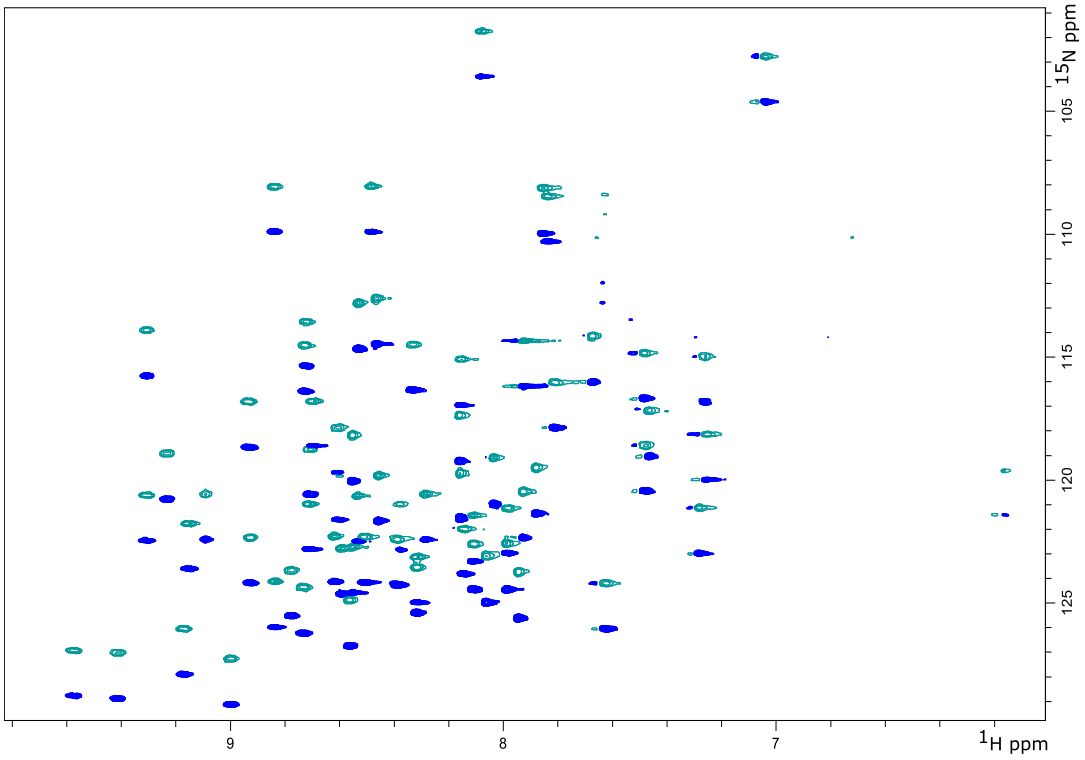

Figure 5.5.: **Isotropic Ubiquitin IPAP-HSQC Anti-phase component.**

that the director of the liquid crystal is aligned parallel with the magnetic field, $\mathbf{B_0}$. The two spectra are shown in Figure 5.6.

PALES generates an output file which contains the alignment tensor and other alignment parameters. The generated alignment tensor this set of RDCs is given in Equation 5.1.

$$\begin{bmatrix} -6.19 \times 10^{-6} & -3.6334 \times 10^{-10} & 1.0809 \times 10^{-7} \\ -3.6334 \times 10^{-10} & -5.833 \times 10^{-4} & 3.5274 \times 10^{-7} \\ 1.0809 \times 10^{-7} & 3.5274 \times 10^{-7} & 6.4524 \times 10^{-4} \end{bmatrix} \tag{5.1}$$

The five principal components of this alignment tensor are as follows; $Szz = 7.5067 \times 10^{-5}$, $Sxx - yy = 5.5277 \times 10^{-4}$, $Sxy = -9.1696 \times 10^{-5}$, $Sxz = -3.8469 \times 10^{-4}$, $Syz = 4.0694 \times 10^{-4}$.

Table 5.3.: **RDCs captured while under no shear:** The RDCs captured from the N-H bonds of ubiquitin while no shear forces are applied

Amino Acid	Residue Number	J-Coupling + RDC [Hz][±0.05]	RDC [Hz][±0.05]	Amino Acid	Residue Number	J-Coupling + RDC [Hz][±0.05]	RDC [Hz][±0.05]
GLN	2	86.19	-6.93	GLN	40	111.75	18.63
ILE	3	106.12	12.56	GLN	41	101.79	6.93
PHE	4	106.12	12.12	LEU	43	75.80	-19.92
VAL	5	98.76	5.63	ILE	44	76.66	-16.03
LYS	6	87.93	-5.63	PHE	45	76.23	-17.33
THR	7	81.43	-13.00	GLY	47	86.19	-6.93
LYS	11	82.30	-12.13	ARG	48	91.39	-1.73
THR	12	80.13	-12.56	LEU	50	77.96	-18.20
ILE	13	96.59	3.46	GLU	51	89.66	-5.63
THR	14	96.16	2.60	ASP	52	94.85	0.00
LEU	15	112.18	16.89	ARG	54	90.10	-5.63
GLU	16	91.39	-2.60	THR	55	87.50	-5.63
VAL	17	89.23	-4.76	SER	57	117.38	23.39
GLU	18	80.13	-13.00	ASP	58	108.29	9.53
SER	20	102.22	9.53	TYR	59	109.15	13.43
ILE	23	86.19	-8.23	ASN	60	96.59	2.16
ASN	25	93.12	-1.30	ILE	61	85.76	-7.80
VAL	26	95.29	2.60	GLN	62	111.32	16.89
LYS	27	79.26	-17.76	LYS	63	91.39	-2.60
SER	28	114.78	18.19	GLU	64	110.88	16.89
ALA	29	82.73	-12.56	SER	65	101.79	6.93
ILE	30	83.59	-10.83	THR	66	109.15	16.89
ASP	32	82.73	-11.69	LEU	67	106.12	12.13
LYS	33	90.09	-3.90	HIS	68	80.56	-14.73
GLU	34	77.54	-13.43	LEU	69	71.47	-22.09
GLY	35	100.05	6.06	VAL	70	81.86	-12.56
ILE	36	84.03	-7.35	LEU	71	77.54	-19.05
ASP	39	111.75	16.89	GLY	76	93.99	0.43

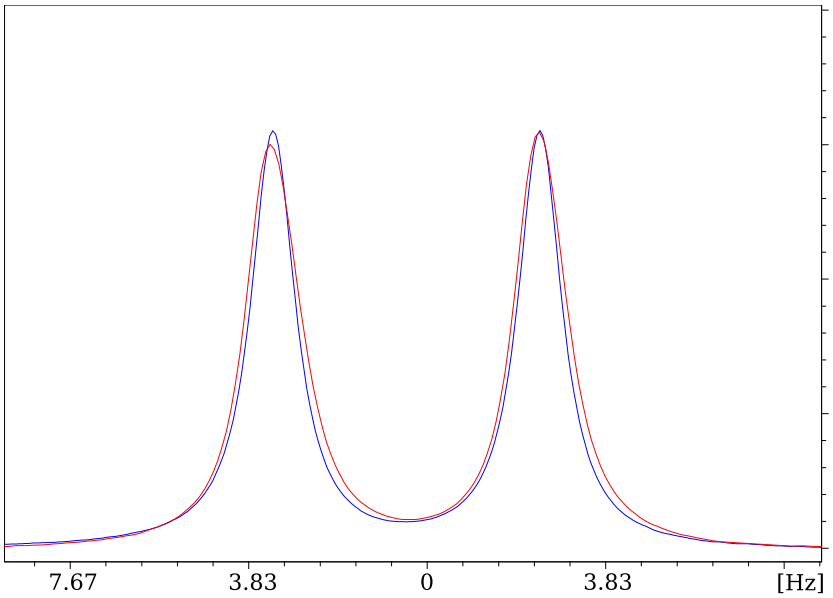

Figure 5.6.: **^{2}H spectra with no applied shear:** The blue spectrum is captured before the IPAP-HSQC. The red spectrum is taken directly after the IPAP-HSQC

Figure 5.7 allows it to be clearly seen that there is a strong correlation between the back calculated RDCs that were output by PALES using the alignment tensor, and the experimentally measured RDCs.

The associated quality factor for this alignment tensor is found to be $Q = 0.209$, with 36 RDC values being used in the final calculation. The PALES output file for this shear profile can be found in Appendix C.

The sample was now sheared at an average rate of 17.98 s^{-1}. The RDC values captured from this shear profile are displayed in Table 5.4. As this experiment was conducted in the presence of an applied shear force there were three ^{2}H spectra conducted, one without the application of any shear after the sample had equilibrated in the magnetic field for 30 minutes, one directly before the IPAP-HSQC, and the final one directly after the IPAP-HSQC (both while under shear). The two spectra captured before and after the IPAP-HSQC are shown in Figure 5.8.

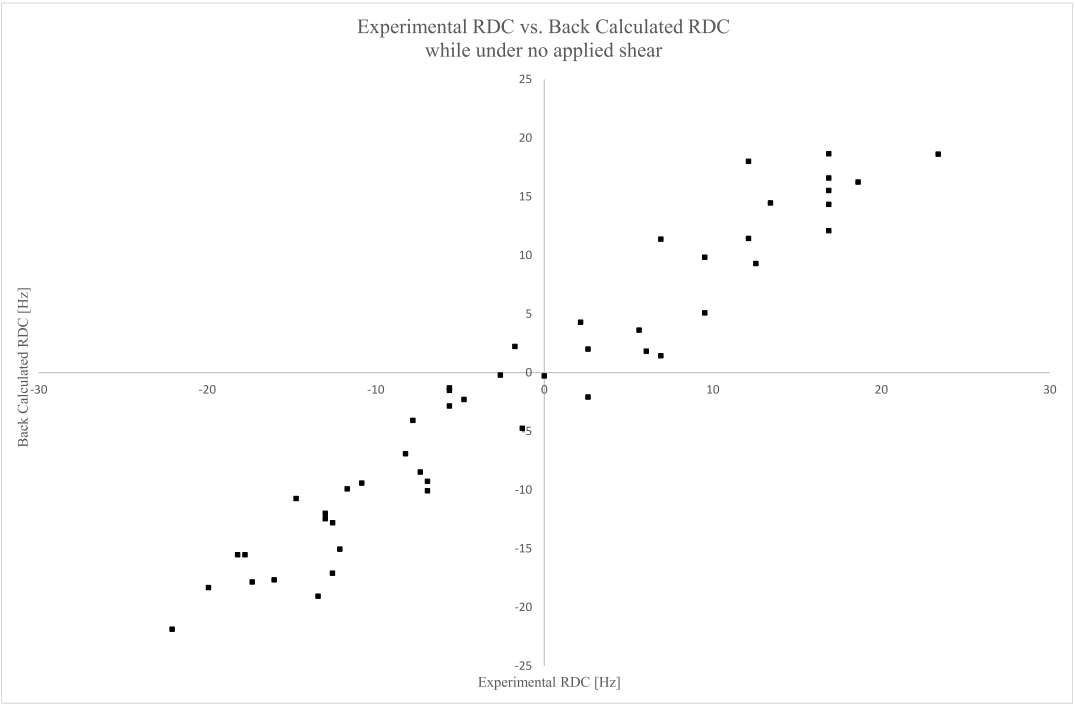

Figure 5.7.: **Experimentally measured RDCs vs. back calculated RDCs while no shear is applied:** Plot showing the relationship between the experimentally measured RDCs and the back calculated RDCs from PALES for all measured N-H bonds of ubiquitin while no shear is applied.

Table 5.4.: **RDCs captured at an average shear rate of 17.98 s^{-1} for N-H bonds of ubiquitin**

Amino Acid	Residue Number	J-Coupling + RDC [Hz][±0.05]	RDC [Hz][±0.05]	Amino Acid	Residue Number	J-Coupling + RDC [Hz][±0.05]	RDC [Hz][±0.05]
GLN	2	98.32	5.20	GLN	40	84.03	-9.10
ILE	3	89.66	-3.90	GLN	41	92.26	-2.60
PHE	4	90.09	-3.90	LEU	43	103.09	7.36
VAL	5	90.96	-2.16	ILE	44	100.05	7.36
LYS	6	96.16	2.60	PHE	45	100.92	7.36
THR	7	100.49	6.06	GLY	47	96.59	3.47
LYS	11	98.76	4.33	ARG	48	94.85	1.73
THR	12	99.19	6.50	LEU	50	100.92	4.76
ILE	13	92.26	-0.87	GLU	51	95.29	0.00
THR	14	92.69	-0.87	ASP	52	92.69	-2.16
LEU	15	88.36	-6.94	ARG	54	94.86	-0.87
GLU	16	95.29	1.30	THR	55	93.99	0.87
VAL	17	97.02	3.03	SER	57	84.03	-9.96
GLU	18	98.32	5.20	ASP	58	91.83	-6.93
SER	20	87.50	-5.20	TYR	59	87.50	-8.23
ILE	23	97.02	2.60	ASN	60	93.56	-0.87
ASN	25	95.72	1.30	ILE	61	96.59	3.03
VAL	26	91.83	-0.87	GLN	62	87.93	-6.49
LYS	27	101.35	4.33	LYS	63	96.16	2.16
SER	28	84.46	-12.13	GLU	64	87.50	-6.49
ALA	29	100.05	4.76	SER	65	92.26	-2.60
ILE	30	99.19	4.76	THR	66	85.76	-6.50
ASP	32	98.33	3.90	LEU	67	88.36	-5.64
LYS	33	95.72	1.73	HIS	68	100.05	4.76
GLU	34	97.02	6.06	LEU	69	103.09	9.53
GLY	35	92.26	-1.73	VAL	70	99.19	4.76
ILE	36	95.29	3.90	LEU	71	101.35	4.76
ASP	39	86.19	-8.67				

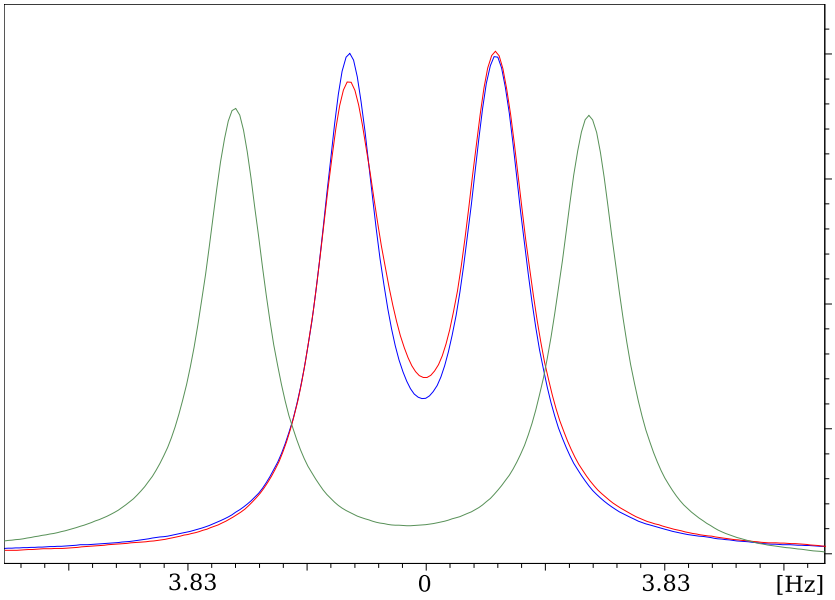

Figure 5.8.: **^{2}H spectra at an average shear rate of 17.98 s^{-1}:** The blue spectrum was recorded under shear before the IPAP-HSQC. The red spectrum was captured directly after the IPAP-HSQC while still under shear. The green spectrum was captured before the application of any shear forces and is used as a reference to allow calculation of the angle of the liquid crystal's director once the shear is applied.

By comparing the quadrupolar splitting between the ^{2}H doublet of the sample before shear is applied, and under an average shear rate of 17.98 s^{-1} it was found that the liquid crystal's director oriented at an angle of 76° relative to the magnetic field $\mathbf{B_0}$. Upon processing these RDC values with PALES an alignment tensor was extracted and is displayed in Equation 5.2. Again when the back calculated RDC values are plotted against the experimentally measured values there is a strong correlation, as is well demonstrated in Figure 5.9. This alignment tensor had a quality value of $Q = 0.244$. The full output of PALES for this shear profile can be found in Appendix C.

$$\begin{bmatrix} -8.60 \times 10^{-4} & 3.71 \times 10^{-4} & 1.67 \times 10^{-3} \\ 3.71 \times 10^{-4} & 1.32 \times 10^{-3} & -1.67 \times 10^{-3} \\ 1.67 \times 10^{-3} & -1.67 \times 10^{-3} & -4.68 \times 10^{-4} \end{bmatrix} \tag{5.2}$$

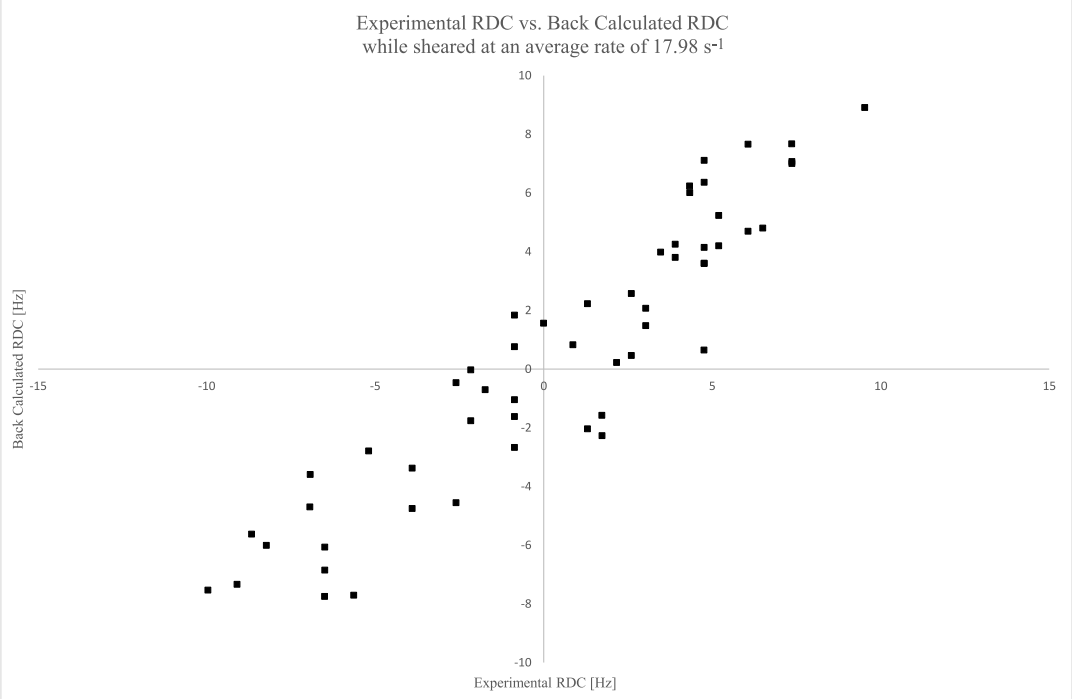

Figure 5.9.: **Experimentally measured RDCs vs. back calculated RDCs while at an average shear rate of 17.98 s^{-1}:** Plot showing the relationship between the experimentally measured RDCs and the back calculated RDCs from PALES for the analyzed N-H bonds of ubiquitin while under an average shear rate of 17.98 s^{-1}.

The five principal components of the alignment tensor for this shear profile are as follows; $Szz = -4.6834 \times 10^{-5}$, $Sxx - yy = -2.1887 \times 10^{-4}$, $Sxy = 3.7102 \times 10^{-5}$, $Sxz = 1.6720 \times 10^{-4}$, $Syz = -1.6662 \times 10^{-4}$.

The next shear profile involved the shear motor running at 12 Hz corresponding to an average shear rate of 215.82 s^{-1}, and was the highest shear rate at which a IPAP-HSQC was captured. The RDC values that were extracted are displayed in Table 5.5.

Again these RDC values were prepared into a PALES input file and iterated through PALES with the structural model, and an alignment tensor was extracted. The alignment tensor is displayed in Equation 5.3. This tensor had a quality factor of $Q = 0.179$ with 41 RDC values contributing to the derivation of this tensor.

Table 5.5.: RDCs captured at an average shear rate of 215.82 s^{-1} for N-H bonds of ubiquitin

Amino Acid	Residue Number	J-coupling + RDC [Hz][±0.05]	RDC [Hz][±0.05]	Amino Acid	Residue Number	J-coupling + RDC [Hz][±0.05]	RDC [Hz][±0.05]
GLN	2	96.16	3.03	GLN	40	86.63	-6.50
ILE	3	90.96	-2.61	GLN	41	91.82	-3.04
PHE	4	90.53	-3.47	LEU	43	100.49	4.76
LYS	6	96.16	2.60	PHE	45	98.76	5.20
THR	7	98.32	3.90	GLY	47	94.85	1.73
LYS	11	96.16	1.73	ARG	48	95.29	2.16
THR	12	96.59	3.90	LEU	50	102.22	6.07
ILE	13	93.12	-0.01	GLU	51	93.99	-1.30
THR	14	92.69	-0.87	ASP	52	94.86	0.01
LEU	15	90.53	-4.77	ARG	54	94.42	-1.30
GLU	16	95.73	1.73	THR	55	95.29	2.16
VAL	17	94.42	0.43	SER	57	86.63	-7.36
GLU	18	96.59	3.46	ASP	58	90.96	-7.80
SER	20	88.79	-3.90	TYR	59	89.23	-6.50
ILE	23	95.72	1.30	ASN	60	94.42	0.00
ASN	25	97.02	2.60	ILE	61	95.29	1.73
VAL	26	92.69	-0.01	GLN	62	90.96	-3.46
LYS	27	102.22	5.20	LYS	63	93.99	0.00
SER	28	90.53	-6.07	GLU	64	89.23	-4.76
ALA	29	95.72	0.43	SER	65	90.96	-3.90
ILE	30	96.59	2.16	THR	66	87.06	-5.20
ASP	32	99.62	5.20	LEU	67	91.39	-2.60
LYS	33	94.86	0.87	HIS	68	99.19	3.90
GLU	34	96.59	5.63	LEU	69	99.19	5.63
GLY	35	93.13	-0.87	VAL	70	98.32	3.89
ASP	39	87.93	-6.93	LEU	71	99.19	2.60

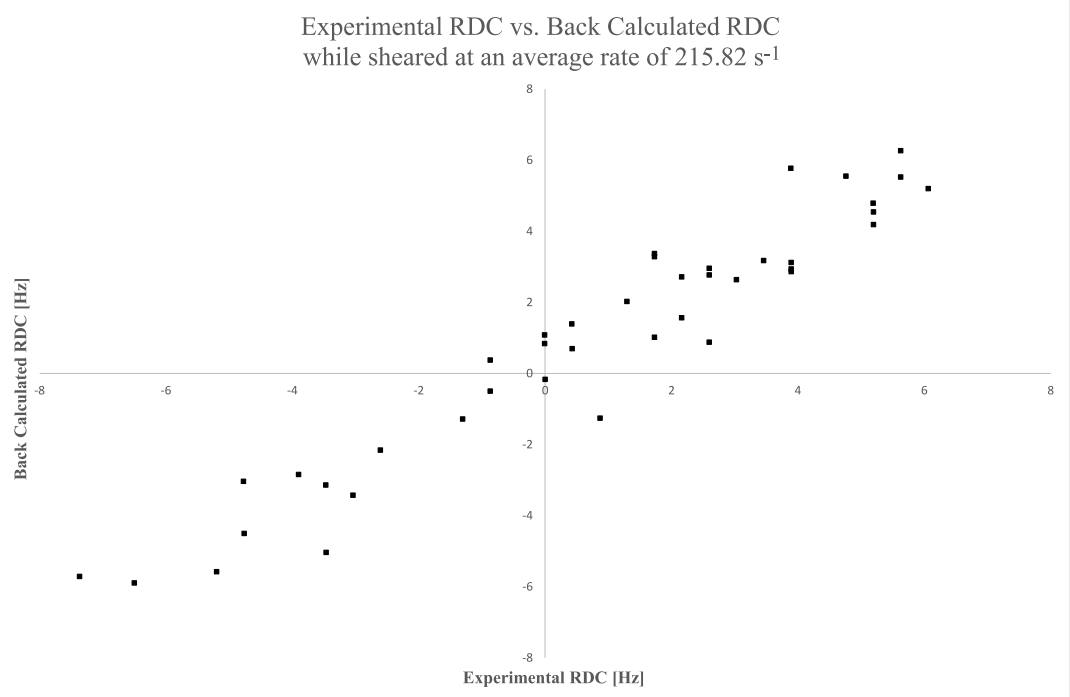

Figure 5.10.: **Experimentally measured RDCs vs. back calculated RDCs while at an average shear rate of 215.82 s^{-1}:** Plot showing the relationship between the experimentally measured RDCs and the back calculated RDCs from PALES for the analyzed N-H bonds of ubiquitin while at an average shear rate of 215.82 s^{-1}.

When the experimental and back calculated RDCs were plotted, once again there was found to be a strong correlation between the values for each N-H bond. This is demonstrated in Figure 5.10.

The PALES output from this shear profile can be found in Appendix C.

$$\begin{bmatrix} -5.73 \times 10^{-4} & 4.68 \times 10^{-4} & 1.21 \times 10^{-3} \\ 4.68 \times 10^{-4} & 1.13 \times 10^{-3} & -1.09 \times 10^{-3} \\ 1.21 \times 10^{-3} & -1.09 \times 10^{-3} & -5.54 \times 10^{-4} \end{bmatrix} \tag{5.3}$$

Extracting the five principal components of this alignment tensor yield the following; $Szz = -5.5432 \times 10^{-5}$, $Sxx - yy = -1.6997 \times 10^{-4}$, $Sxy = 4.6830 \times 10^{-5}$, $Sxz = 1.2076 \times 10^{-4}$, $Syz = -1.0846 \times 10^{-4}$.

The ^{2}H spectra from this shear profile allowed the angle of the liquid crystal director relative to the magnetic field $\mathbf{B_0}$ to be calculated. This angle was found

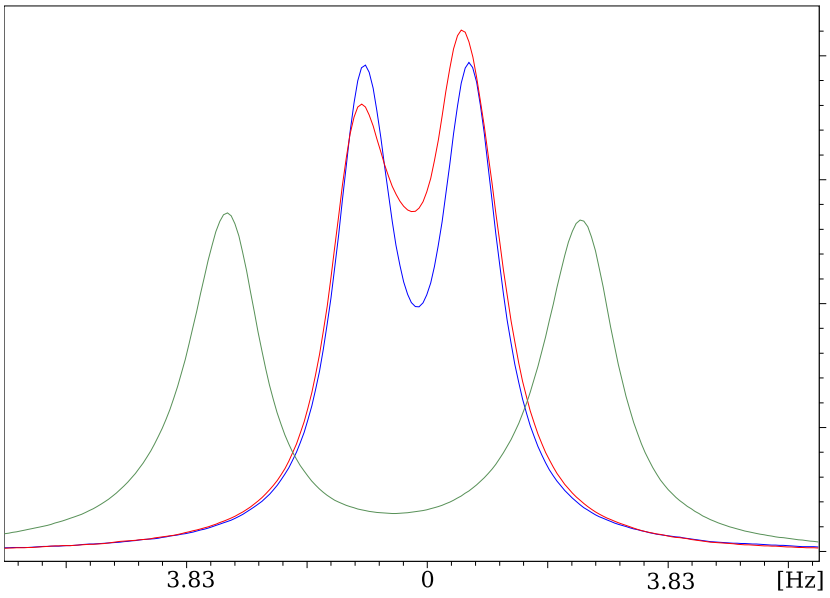

Figure 5.11.: **^{2}H spectra while under an average shear rate of 215.82 s^{-1}:** The blue spectrum was conducted before the IPAP-HSQC. The red spectrum was captured directly after the IPAP-HSQC. The green spectrum was captured before the application of any shear forces and is used to calculate the angle of the liquid crystal's director.

to be 68° . These ^{2}H spectra are displayed in Figure 5.11. It can be seen that spectrum captured directly after the IPAP-HSQC is somewhat different to that captured before. It appears that the quadrupolar splitting value has decreased slightly, indicating that the angle of the liquid crystal's director has also changed. Upon recalculating the angle of the director, it is found to be at 67° relative to $\mathbf{B_0}$, an insignificant change compared to the 68° that the spectra prior to the IPAP-HSQC indicated.

The RDC values, ^{2}H spectra, alignment tensors, and PALES output files for the four additional shear profiles are outlined in Appendix D.

5.2.4. Conclusion

All three RDC datasets displayed in this section, as well as those found in Appendix D all allow suitable alignment tensors to be found with relatively low quality factors. More importantly, the RDC values are different for each shear

profile, indicating that there is a change in the alignment of the ubiquitin with respect to the magnetic field. The ^{2}H spectra that were captured before and after each IPAP-HSQC indicated that there were no significant changes in the alignment of the liquid crystal for the duration of the experiments. This lack of change in the ^{2}H spectra leads to the assumption that there was no significant changes to the alignment of the liquid crystal material, and therefore also the ubiquitin molecules during the acquisition of the RDC data. This allowed the results from each shear profile to result in alignment tensors with low quality factors.

Interestingly, as was also seen in Chapter 4, there is a large notable difference between the RDC values obtained with no shear applied, and those that were captured under shear. In addition to this large difference between these two groups it has also been noted that the RDC values obtained under shear are of a similar order and magnitude. This was somewhat unexpected given the large variation in shear rates applied, and is yet to be fully understood.

5.3. Structural refinement using multiple RDC datasets

5.3.1. Introduction

Once it had been demonstrated that the capture of multiple sets of RDCs from a single sample was possible using the application of shear stresses to the alignment media, the question of the usefulness of this data was posed. While the calculation of an alignment tensor does demonstrate that the multiple RDC sets captured do all align well with the X-Ray crystal structure of ubiquitin, with different alignment tensors, they do nothing to help improve upon the structure, or provide further information. The most direct method for further investigation into the

usefulness of these RDC sets is the calculation of a molecular model of the target protein, ubiquitin.

The refinement of a protein's structure using NMR data involves a number of steps. First the assignment of each amine peak in the ^{15}N-HSQC must take place. This typically uses multiple different 3D NMR experiments, such as the HNCA, HN(CO)CA, HNCO, and HN(CA)CO experiment, all named by the order in which they pass the magnetization between the nuclei of each amino acid. These experiments allow the protein's primary sequence to be "walked" along, allowing each peak to be assigned to its corresponding amino acid. Once this is complete a series of further investigations can take place which gather structural restraints, which were all described in detail in Section 2.3. Some of these structural restraints may also include angular restraints such as the ψ and φ angles which can be generated from the Karplus equation, distance restraints obtained from NOEs, and orientational restraints from residual dipolar couplings (NOEs are the first port of call for most structure determinations).

Once the restraints have been gathered, they along with the sequence for the protein, are used in a simulated annealing process in a molecular mechanics program. Each of these restraints has a particular "energy" associated with the resultant structure fitting it within set bounds or not. Conformation which are inconsistent with the experimental restraints incur energy penalties which increase with their number and extent. The result is a set of lowest energy structures which best match the provided information.

Using this process, a series of ensembles were prepared from the captured RDC datasets and minimal synthetic NOE data generated from the X-ray structure. The RDC data is added incrementally in order to determine if an increased number of RDC sets provides a significant improvement to the refined structures.

5.3.2. Experimental Method

The simulated annealing of the ubiquitin molecule for this investigation was carried out using Crystallography and NMR System Solve (CNS-Solve) [92], a program which is commonly used for the refinement of NMR structures. Initially, a series of structures of increasing quality were prepared using solely synthetically generated NOE data (the number of NOEs used in each set of structures is outlined in Table 5.6). Each of these NOE datasets generated an ensemble of 10 structures, which were compared using PyMol [93] using the root-mean-square deviation (RMSD) to determine variance between each structure in the set. The RMSD for each ensemble can be calculated according to Equation 5.4 in which δ is the distance between N pairs of identical atoms. Only the main chain atoms for residues 1 - 70 were included in the calculations of RMSD for these ensembles (Cα, carbonyl carbon and oxygen, amide nitrogen). Residues 71 - 76 were excluded due to their location in the relatively unrestrained, flexible tail of the protein.

$$RMSD = \sqrt{\frac{1}{N}\sum_{i=1}^{N}\delta_i^2} \tag{5.4}$$

The RMSD value that is returned is an averaged distance value between the superposed atoms, in Ångström (Å).

Continuing on from this, sets of RDCs were added into the annealing process, and an ensemble of the lowest energy structures were again produced with each set of NOEs. This first set of RDC data that was introduced was collected without any shear forces.

This process was repeated a further three times, with an additional RDC data set being added each time, and the resulting ensemble of structures was collected. The three RDC datasets added are those captured with average shear rates of 17.98 s^{-1}, 215.82 s^{-1}, and again with no applied shear forces.

Table 5.6.: **RMSD for each ensemble:** The RMSD for each ensemble calculated with increasing numbers of RDC datasets .

Number of NOEs	No RDC sets RMSD [Å]	1 RDC set RMSD [Å]	2 RDC sets RMSD [Å]	3 RDC sets RMSD [Å]	4 RDC sets RMSD [Å]
261	5.55	4.86	4.392	2.825	4.292
351	4.07	3.747	4.491	3.684	3.582
440	2.66	2.75	1.773	2.544	2.458
532	2.80	1.644	2.8	2.09	2.591
619	2.70	1.864	1.427	1.278	1.629
711	1.64	1.214	1.653	1.679	1.635
792	1.97	0.925	1.178	0.942	1.183
880	1.42	0.794	0.892	0.822	0.84

5.3.3. Results and Discussion

The set of structures obtained with the use of 261 NOEs and no RDC data is displayed in Figure 5.12. It is clear from both the ensemble obtained, and an individual structure displayed in Figure 5.13 that the refinement of a structure using just 261 NOEs is not sufficient to obtain a structure that is comparable to that of the X-Ray structure displayed in Figure 5.1. However, the direction and relative orientation of the polypeptide chain that underpins the X-Ray structure is beginning to be displayed in this ensemble.

Figure 5.14a shows the ensemble that was obtained with 880 NOEs and no other structural restraints, and demonstrates a structure that is clearly defined to a much higher standard, and is beginning to become directly comparable to that of the X-Ray structure.

The RMSD results for all 8 NOE datasets are displayed in Table 5.6, and show a marked decrease in the RMSD of each ensemble as the number of NOEs used increases. While the overall trend is very clear there are two outliers to this, with

Figure 5.12.: **Ensemble of ubiquitin structures created with 261 NOEs:** This ensemble of ubiquitin structures was obtained using 261 NOEs and no other structural restraints.

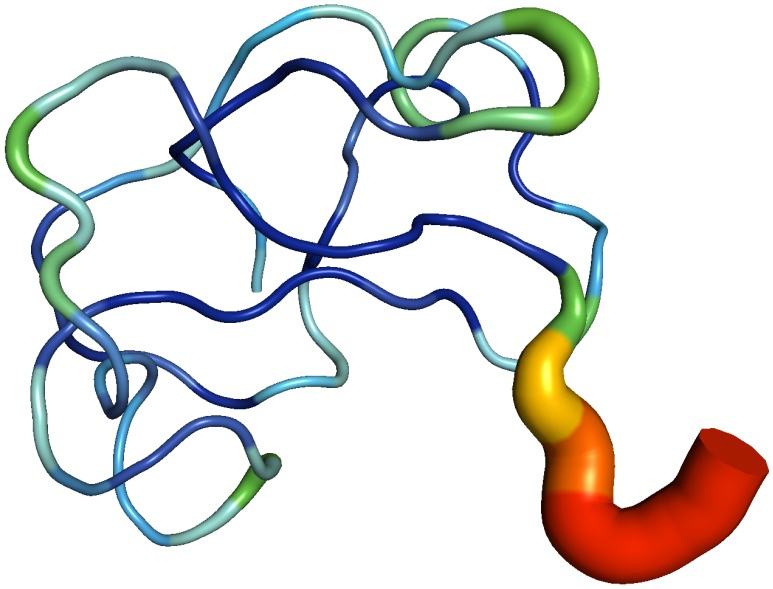

Figure 5.13.: **Single structure created for ubiquitin created with 261 NOEs:** A single structure from the ensemble obtained with 261 NOEs and no other structural restraints. This image is created with the structure being displayed as a "putty" plot. A putty plot simply shows areas of higher B factor as a larger cylinder, allowing easy determination of areas with high vibration motion or flexibility.

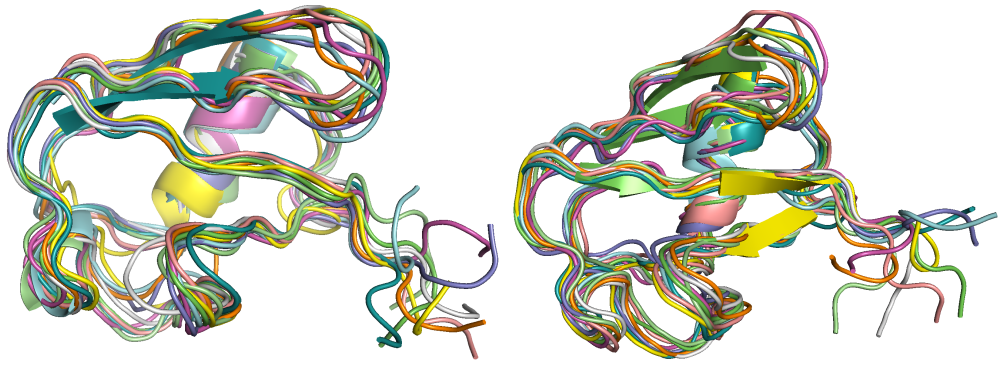

(a) (b)

Figure 5.14.: **The effect of adding RDC data to the simulated annealing process:** a) Ensemble of structures generated with 880 NOEs alone. b) Ensemble generated with 880 NOEs and an RDC data set obtained with no applied shear forces.

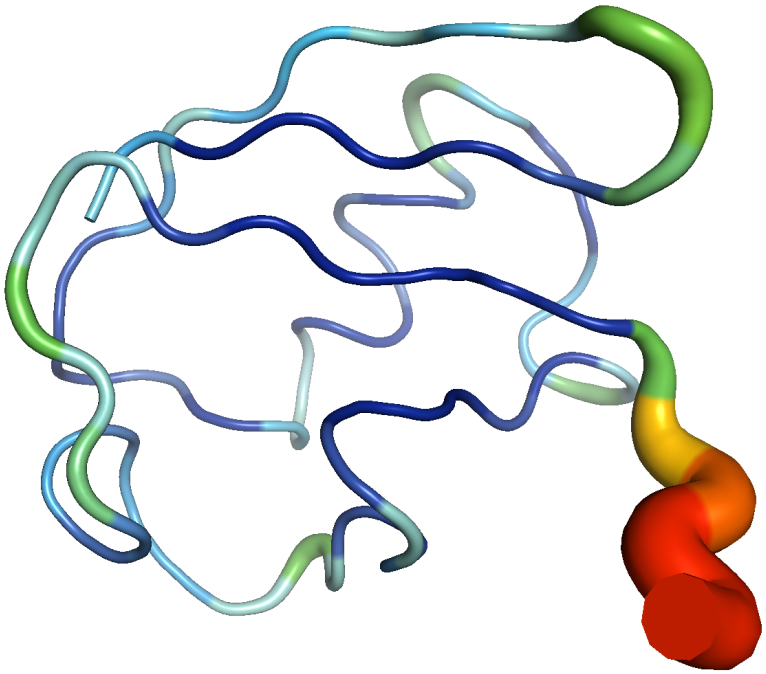

Figure 5.15.: **Single structure created for ubiquitin created with 880 NOEs:** A single structure from the ensemble obtained with 880 NOEs and no other structural restraints.

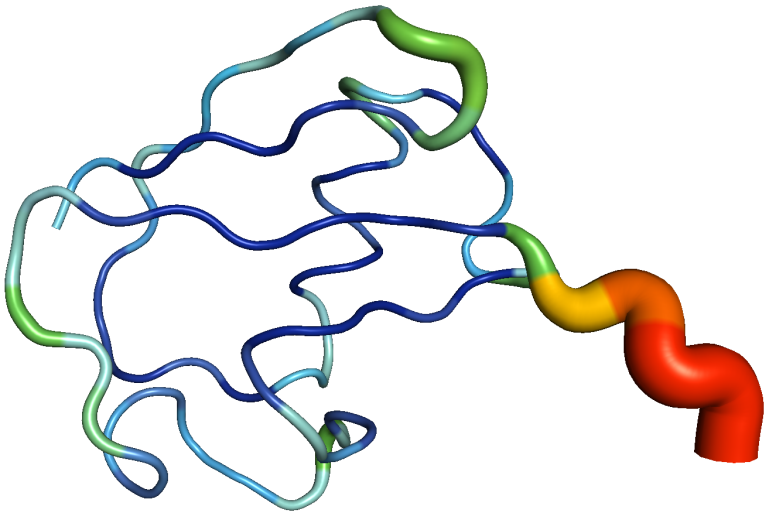

Figure 5.16.: **Single structure created for ubiquitin from 880 NOEs and an RDC set captured with no applied shear:** A single structure from the ensemble obtained with 880 NOEs and the RDC data from 880 NOEs and an RDC set captured with no applied shear.

the ensembles generated with 532 and 792 NOEs having higher than expected RMSD values. The reasons for this have not been investigated, however they are likely to be caused by a group of NOEs in each of those sets conflicting with the structure that is being developed.

The addition of the first RDC set into the annealing process resulted in a decrease in the RMSD for most of the ensembles generated, as can be seen in Table 5.6.

The results obtained from this show that the addition of one RDC data set results in higher quality ensembles of structures being obtained. This can be seen through the consistently lower RMSD values for the ensembles generated with RDC data in comparison to those generated solely with NOE data. Figure 5.17 demonstrates this well, showing that the RMSD values found when a single RDC data set is used are lower than that obtained with only NOE data. The addition of the remaining three RDC datasets is also displayed in Figure 5.17 and Table 5.6, and they all appear to show an improvement over the NOE only data set. The average of each of the RMSD values for those ensembles generated with

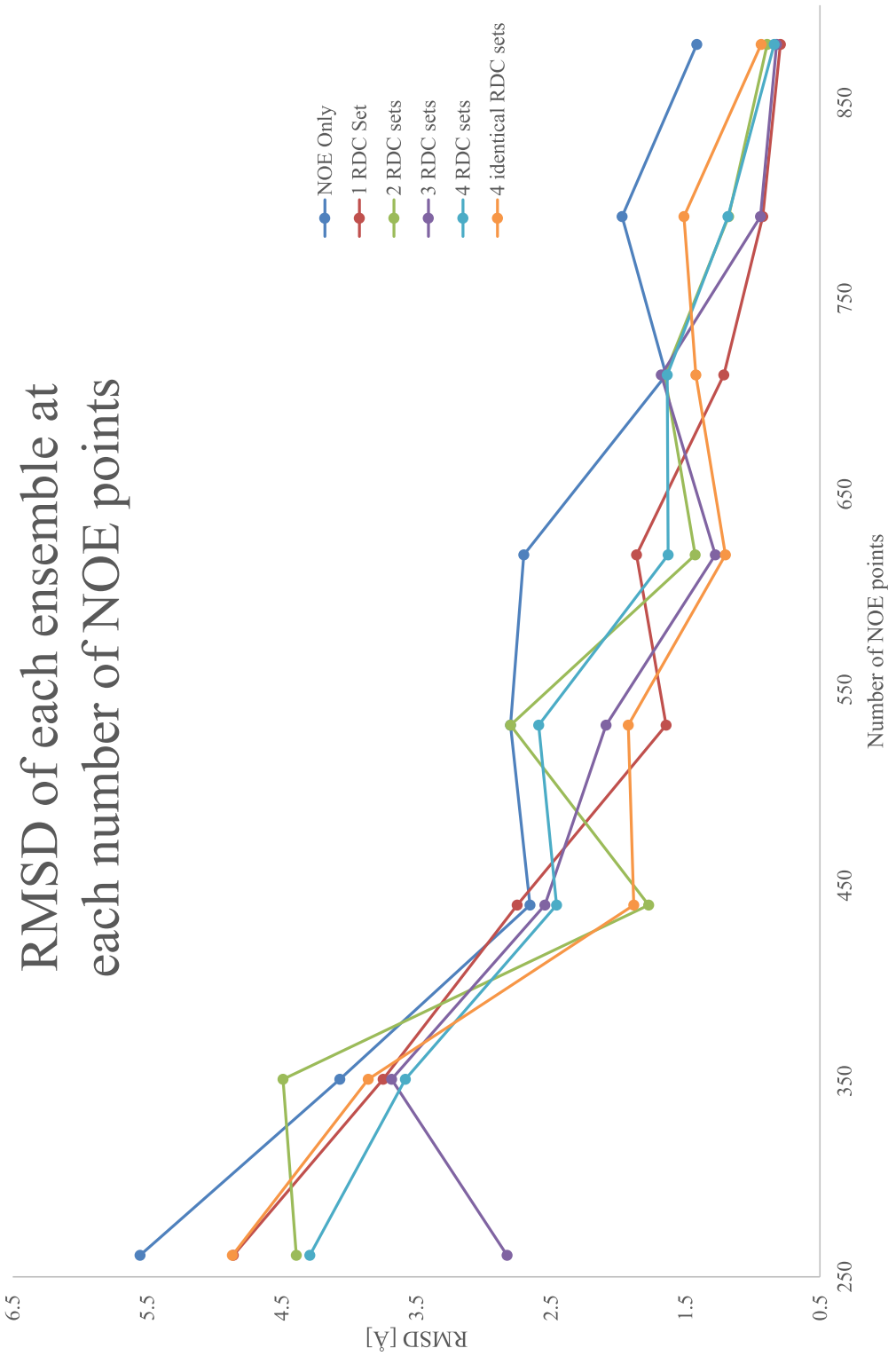

Figure 5.17.: **Plot of the RMSD for each ensemble generated**

Table 5.7.: **RMSD for each ensemble generated with 4 identical RDC datasets**

Number of NOEs	4 identical RDC datasets RMSD [Å]
261	4.867
351	3.857
440	1.883
532	1.924
619	1.202
711	1.422
792	1.511
880	0.937

RDC data was taken and plotted in Figure 5.18, showing a consistently lower value compared to that of the NOE only data.

It was noted that the addition of more than one RDC set did not appear to result in any further consistent improvement to the quality of the ensembles generated. One possible explanation of this result is that the RDC sets obtained are simply transformations of each other and contain no new information. In order to test this another set of ensembles were calculated with the same RDC set being applied four times. The results of this are displayed in Table 5.7 and Figure 5.17, and show very similar RMSD values compared to the results obtained with datasets recorded at different orientations of the director with respect to the magnetic field, $\mathbf{B_0}$. This supports the idea that the multiple RDC sets are not providing new information about the structure even though the alignment tensors are found to be different in each case, and the raw RDC values do not appear to be simply scaled versions of one another.

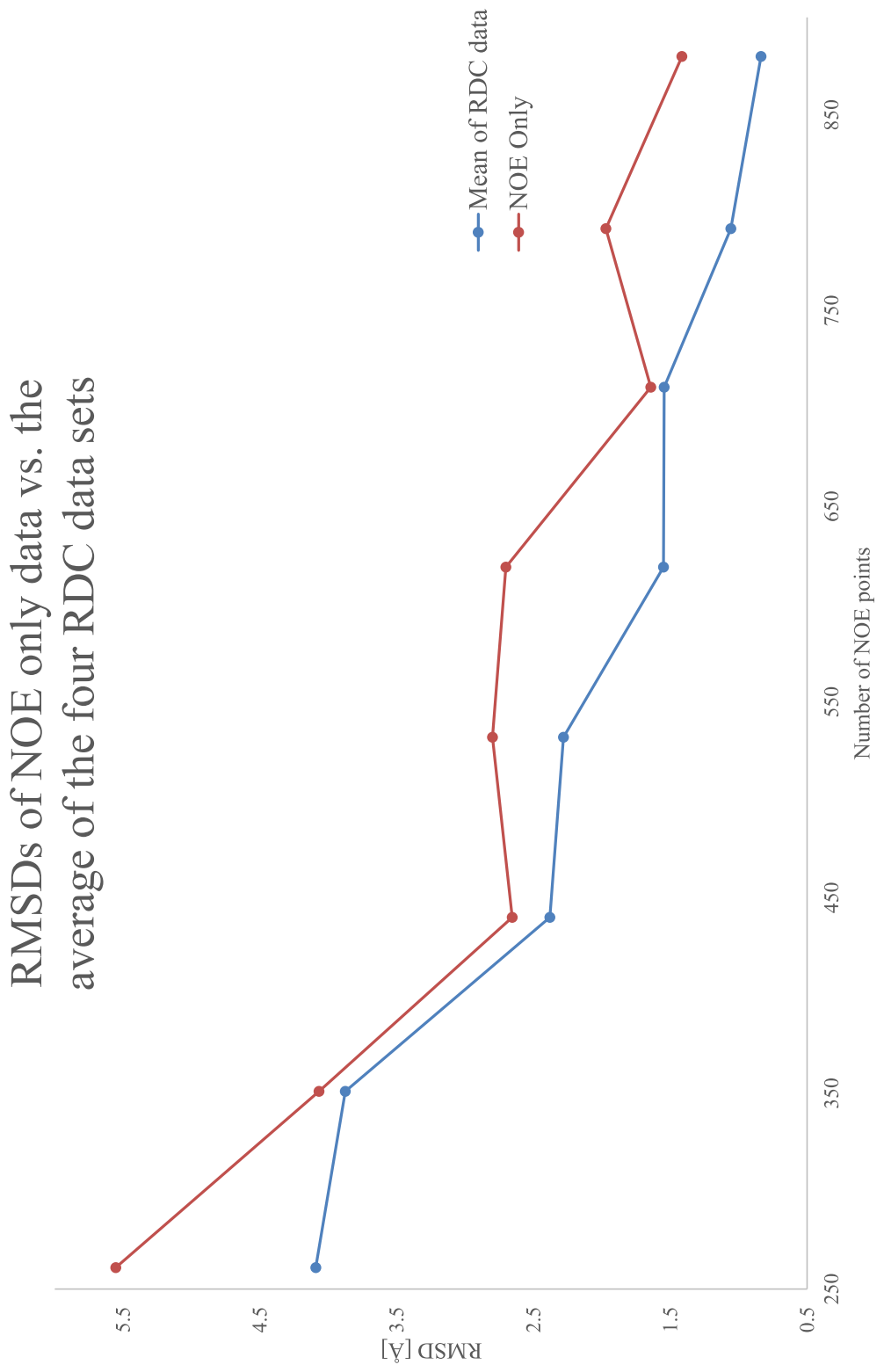

Figure 5.18.: **RMSD data for the average of the four RDC data ensembles and NOE only ensembles:** The mean of the four sets of ensembles generated from increasing amounts of RDC data plotted against the NOE only data.

Table 5.8.: **RMSD data for ensembles generated with experimental NOE data:** The RMSD for each ensemble of 10 structures calculated from sets of NOE data and a variety of RDC datasets.

Number of NOEs	No RDC sets RMSD [Å]	One RDC set RMSD [Å]	Two RDC sets RMSD [Å]	Three RDC sets RMSD [Å]	Four RDC sets RMSD [Å]
123	6.08	5.726	4.533	6.229	6.609
181	5.29	4.531	4.723	4.044	4.84
240	5.83	3.451	4.023	3.548	4.197
296	3.43	2.705	2.824	3.336	3.191
350	3.87	3.12	3.104	3.188	4.087
398	3.77	2.374	3.586	3.119	1.881
457	2.44	2.637	1.787	3.069	2.011
520	2.61	2.239	2.534	1.932	2.225
578	2.07	1.791	2.35	2.35	1.674

In order to determine if the results seen thus far were due to the use of a synthetic NOE data set or would be applicable to real experimental data, the same simulated annealing process was applied with sets of experimental NOEs extracted from the literature [86]. The NOEs in this set were randomized and a selections were made with the number of NOEs outlined in Table 5.8. These NOEs were again used in the same process as the prior synthetic data with 5 groupings of ensembles prepared, those with no RDC data, with one RDC data set, two RDC datasets, three RDC datasets, and four RDC datasets. The RDC datasets used were obtained under the application of average shear rates of 0 s^{-1}, 17.98 s^{-1}, 215.82 s^{-1}, and a repeat with no shear again, as is displayed in Table 5.8.

Similar to the results obtained with the synthetic NOE data, the addition of at least one set of RDC data did, for the most part, result in an improved ensemble of structures being obtained. Again as with the synthetic data, the addition of more than one RDC set did not appear to improve the structure further.

5.3.4. Conclusion

It is clear from the structures calculated in this section that increasing the number of NOEs used in the annealing process does significantly lower the RMSD of any ensemble generated. It is also demonstrated that including at least one set of RDC data does result in a lower RMSD for the ensembles generated (Figures 5.14 and 5.17).

Disappointingly the analysis of this data does lead to the conclusion that, no, capturing multiple RDC datasets from a single sample whose alignment media is reoriented by shear does not allow a higher quality structural model to be generated. The proposed reasoning behind these observations is that each additional RDC set is not providing any new information about the structure, and is just a trivial transformation of the previous data in some way.

6. Conclusions and Future Directions

6.1. Conclusion

The goals of this thesis can be broken up into several parts. Initially, the development of a method for controllably realigning multiple liquid crystalline phases was targeted. The three materials that were used for this were CTAB in D_2O, PBLG in $CDCl_3$, and finally bacteriophage Pf1 in H_2O / D_2O buffer. Each of these materials were prepared into a nematic liquid crystal phase and loaded into a rheo-NMR cell, before a variety shear forces were applied. By monitoring the ^2H spectrum of each material it was possible to calculate the average angle of the liquid crystals' directors relative to the magnetic field at any given time. When the different shear profiles were applied it was found that the ^2H spectrum responded, and in many cases, generated a new constant spectrum indicative of a stable alignment being formed. The work outlined in Chapter 3 clearly demonstrated that it is possible to controllably realign the director of each of the three liquid crystalline materials tested using shear.

The second part of this thesis investigated the capture of RDC data from a small molecule, and the effect that reorienting the director of the liquid crystal host media would have on the RDC values captured. This was carried out using a system comprised of (+)-isopinocampheol and PBLG in $CDCl_3$. It was hoped

that multiple RDC sets with low quality factors would be extracted from a single sample, simply through the controlled application of a shear force to the sample.

As is described in Chapter 4, this was not achieved. Although shear clearly changed the measured RDCs, the RDC data sets that were obtained could not be fitted to a high quality on to a structural model that was developed, even when the RDC set was taken from a sample without the application of any shear forces. The reasons for the poor quality data outlined in this chapter are not fully understood, but are theorized to be due to sample separation of the course of the experiment, something that is challenging to control with current experimental set up (the sheal at the top of the cell is imperfect which allows solvent evaporation). Another possible reason for the poor fit is the low number of dipolar couplings that are accessible, which may result in any errors in the captured couplings not being averaged out over a significantly large data set.

The final part of this thesis was the application of the two prior parts to a protein structure. RDCs are more commonly applied to the determination of protein structures than small molecules due in part to the significantly larger number of accessible dipolar couplings present. Given this it seemed prudent to attempt to apply this method of RDC capture to a protein sample, as is detailed in Chapter 5. The protein that was investigated was ubiquitin, a small widespread protein that has been extensively studied, and is commonly used to demonstrate new protein-NMR techniques. Ubiquitin along with an alignment media, bacteriophage Pf1, were placed into a rheo-NMR cell and RDC data sets were captured while under multiple shear rates. The initial analysis of these multiple data sets involved the fitting of the captured couplings to a structure that had been determined by X-Ray crystallography.

This fitting resulted in an alignment tensor being generated, from which a set of RDCs can be back calculated, and a quality factor extracted. Promisingly each of the shear profiles tested resulted in a different set of RDCs being captured,

which all had high quality factors. This was a positive outcome and showed that the multiple RDC data sets captured at different orientations were each still consistent with the structure of ubiquitin and their own alignment tensors.

Once it had been demonstrated that the multiple RDC sets were consistent with the already known structure, the usefulness of these multiple sets in improving a generated structure was tested. Through this process multiple ensembles of structures were prepared with different amounts of contributing NOE and RDC data taken into account as structural constraints, and the RMSD of each resulting ensemble was compared as a tool for the analysis of the quality of the structures. Four of the RDC sets captured from ubiquitin were used in this process along with synthetic NOE data generated from the X-Ray structure, and an experimental set of NOEs taken from the literature [86]. In both the synthetic and experimental NOE cases the addition of at least one set of RDCs to the simulated annealing process did result in a higher quality set of structures being generated, based on the lower RMSD values. However, the addition of more than one set of RDCs did not appear to result in any further improvement to the structures obtained. The addition of four identical RDC data sets resulted in very similar RMSD values to those obtained with unique RDC sets, indicating that the additional data was not providing any extra helpful information to the simulated annealing process.

6.2. Future Directions

This thesis has provided an insight into a number of different areas that could be persued. These include the intriguing effects that the application of different shear profiles have on nematic liquid crystal materials. As well as simply controlling the director of a liquid crystal material, the dynamic motions and micro scale orientations of the particles present in these samples is a large area that may be investigated in the future.

The application of RDCs for piecing together the structures of small organic molecules is an area that is still very much in its infancy. As was mentioned in Chapter 4, only 43 references to small organic molecule RDCs could be found in a literature search. It is clear that RDCs can be a very useful, albeit difficult, tool for determining the stereochemistry of a small molecule, and that this area will continue to develop and increase in popularity as it becomes more widely understood.

Protein structure determination is by far the largest current application of RDCs, and will no doubt continue to be so for the foreseeable future. As the alignment media that are currently available are somewhat limited and cannot easily be used with every target protein, there does need to be further development of methods, such as the ones tested in Chapter 5, that allow single alignment media to be tweaked so that multiple different RDC data sets can be extracted. While this thesis set out with this goal in mind, it did not adequately achieve results that allowed for the improvement of a protein's structure (despite the applied shear forces clearly having an effect). Other methods of tweaking the alignment media used such as the mixing of media, or mounting of physically restrained media in such a way that they can be rotated, or just simply the discovery of new alignment media may open the door to investigations like this improving the quality and quantity of RDC data that is able to be captured.

A. (+)-Isopinocampheol NMR Spectra

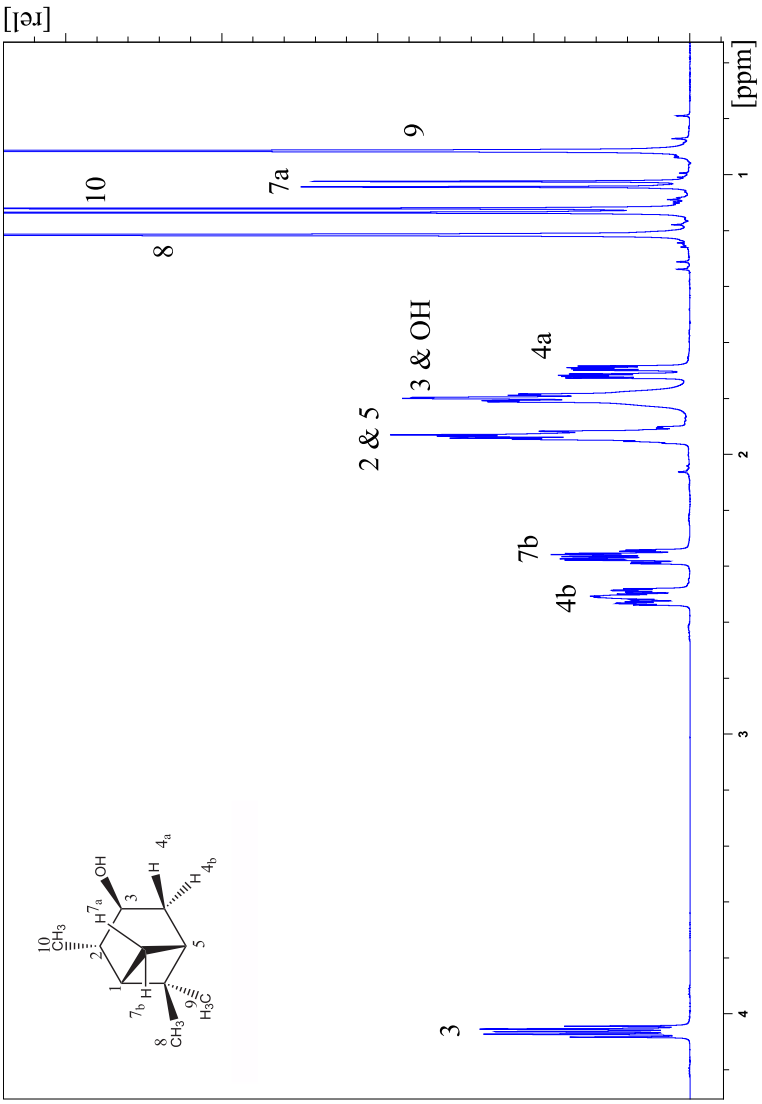

Figure A.1.: **^{1}H spectrum of (+)-IPC**

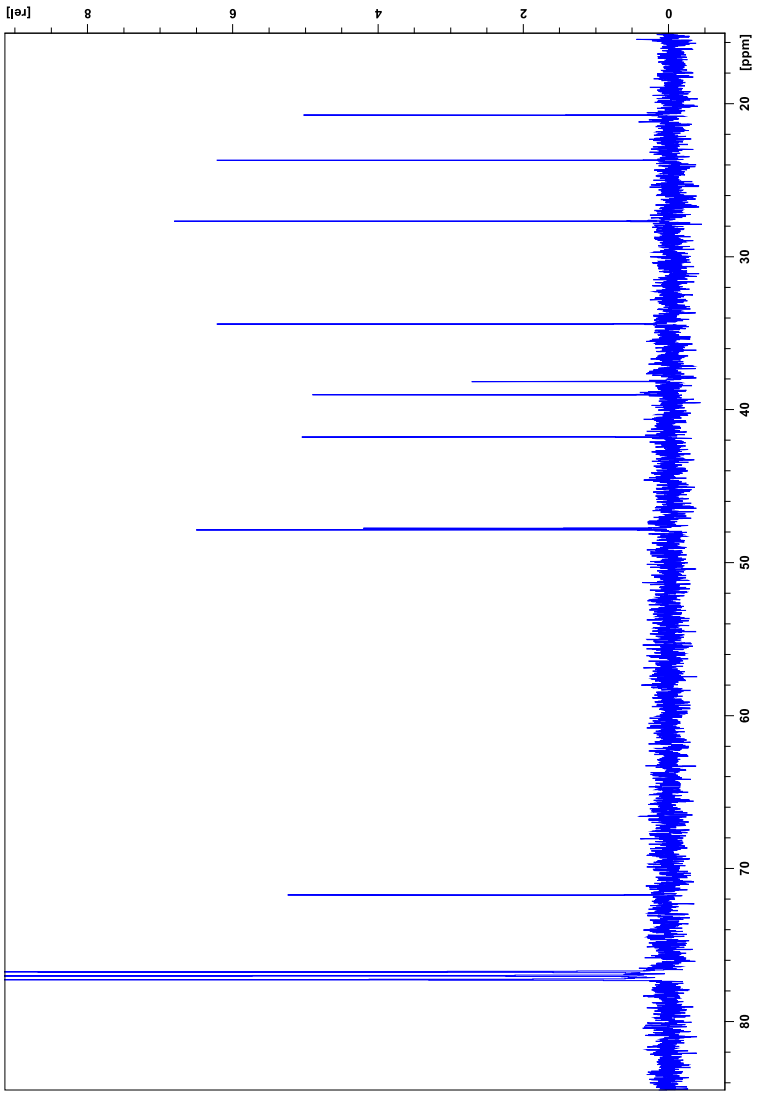

Figure A.2.: **^{13}C spectrum of (+)-IPC**

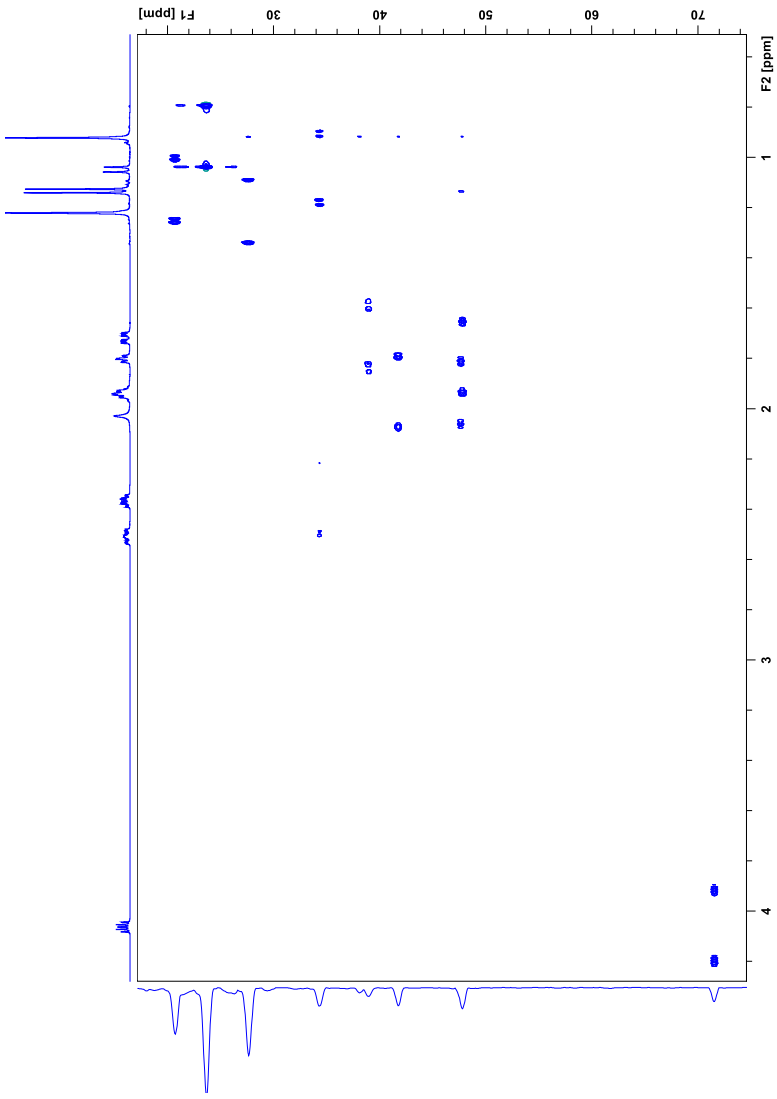

Figure A.3.: **Coupled HSQC spectrum of (+)-IPC**

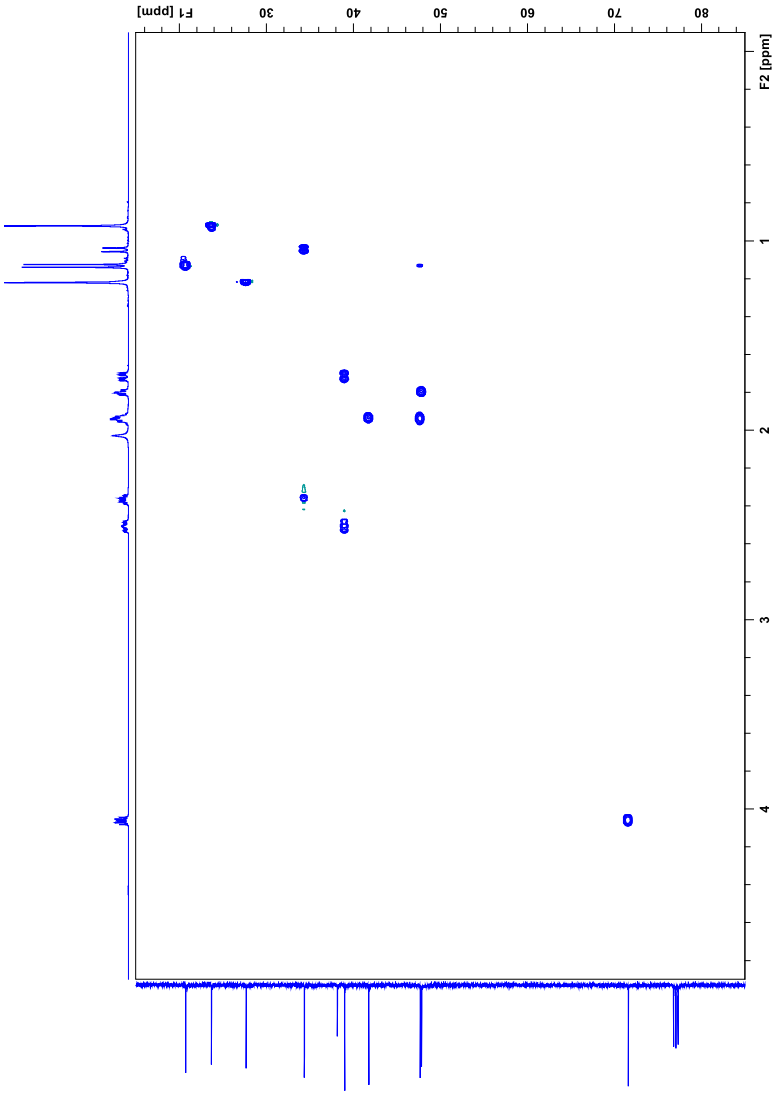

Figure A.4.: **Decoupled HSQC spectrum of (+)-IPC**

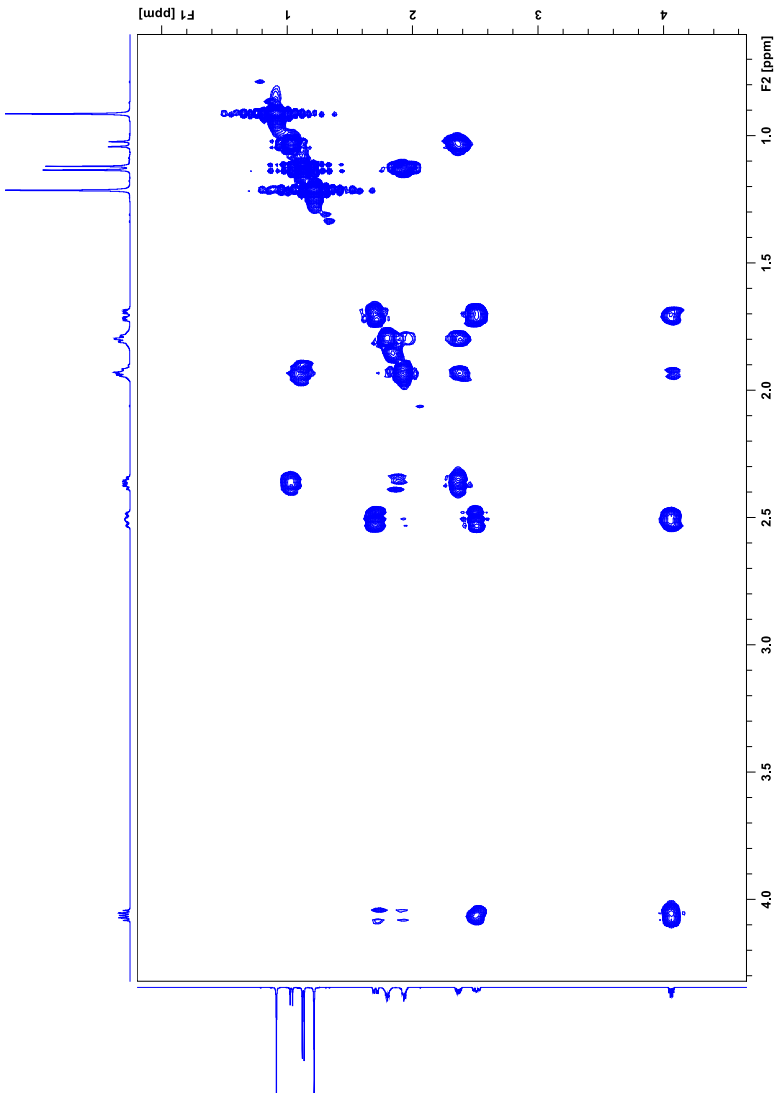

Figure A.5.: **COSY Spectrum of (+)-IPC**

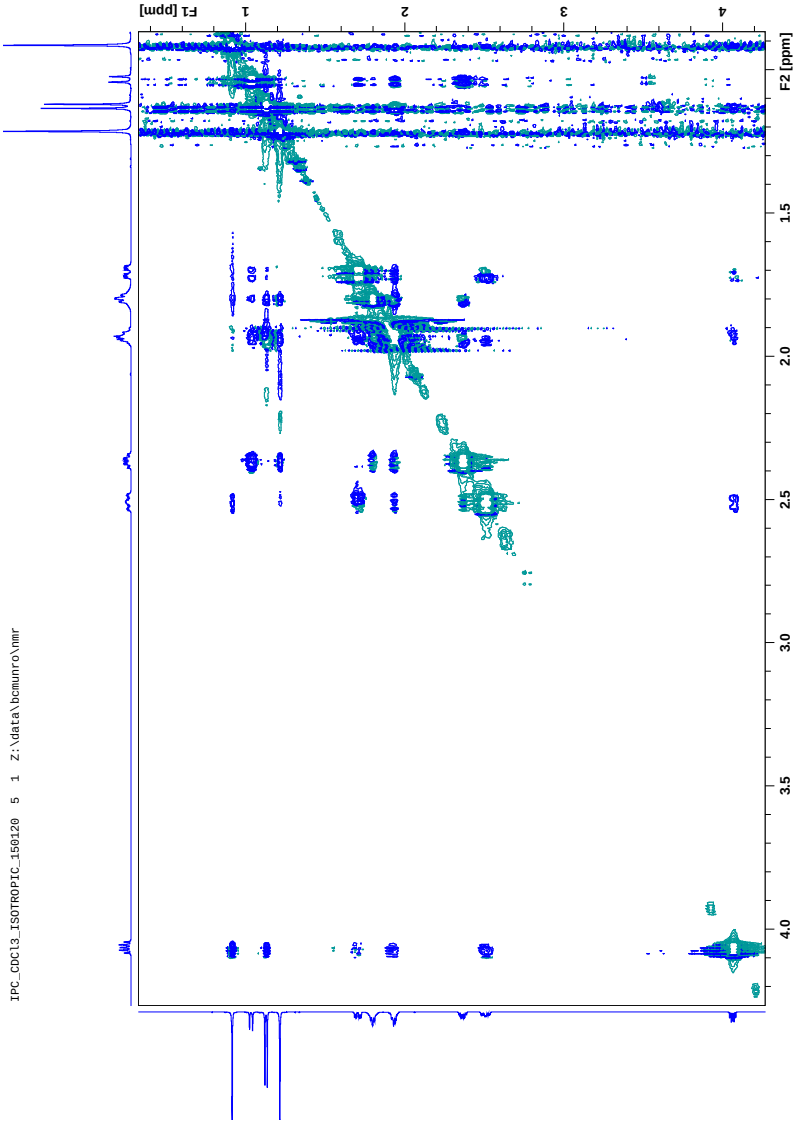

Figure A.6.: **NOESY Spectrum of (+)-IPC**

B. (+)-Isopinocampheol xyz Coordinates

XYZ formatted coordinates generated using Gaussian 09 with a geometry optimized B3LYP/6-311+g (2d,p) calculation of (1S,2S,3S,5R)- (+)- Isopinocampheol:

```
29
Molecule Name
C 0.45930 0.45530 -1.00020
C -1.51340 -0.26650 0.48180
C -1.01430 0.71470 -0.62840
C 1.39500 0.11240 0.22110
C 0.80420 -1.33450 0.08630
C -0.56660 -1.46430 0.76470
H 0.82280 1.21820 -1.69860
O -2.79470 -0.82870 0.15270
H -1.63460 0.30710 1.40990
C -1.31750 2.18110 -0.28660
H -1.59690 0.46330 -1.52490
C 1.26780 0.84790 1.55820
C 2.87700 0.16650 -0.18910
H -0.31650 -1.48570 -1.87560
H 1.45860 -2.16950 0.35980
H -0.45410 -1.58820 1.84790
H -1.06110 -2.36970 0.39600
C 0.57200 -1.03860 -1.41920
H 3.50350 -0.30450 0.57840
H 3.20760 1.20760 -0.28970
H 3.08430 -0.33610 -1.13710
H 0.25680 0.86110 1.96730
H 1.59860 1.88920 1.46160
H 1.91460 0.37360 2.30720
```

```
H -3.44310 -0.11660 0.10360
H -0.75880 2.52530 0.58930
H -2.38460 2.32910 -0.07640
H -1.05910 2.83710 -1.12550
H 1.43730 -1.25540 -2.04670
```

C. PALES output files for shear regimes 23, 24, and 25

PALES output file for shear regime 23

```
REMARK Molecular Alignment Simulation.
1_NO SHEAR_
Aligned With Magnet
REMARK Simulation parameters.
DATA PALES_MODE DC
DATA TENSOR_MODE SVD (Order Matrix Method)
REMARK Order matrix.
DATA SAUPE_MATRIX S(zz) S(xx-yy) S(xy) S(xz) S(yz)
DATA SAUPE 7.5067e-005 5.5277e-004 -9.1696e-005 -3.8469e-004 4.0694e-004
DATA IRREDUCIBLE_REP A0 A1R A1I A2R A2I
DATA IRREDUCIBLE 1.1901e-004 4.9795e-004 5.2675e-004 3.5776e-004 1.1869e-004
DATA IRREDUCIBLE GENERAL_MAGNITUDE 1.1615e-003
REMARK Mapping of coordinates.
DATA MAPPING_COOR Szz_d(x) Szz_d(y) Syy_d(x) Syy_d(y) Sxx_d(x) Sxx_d(y)
DATA MAPPING -0.35012 -0.72636 1.45845 -0.62546 0.54641 0.48352
DATA MAPPING INV 1.99852 0.72636 -1.08843 0.62546 -2.23505 -0.48352
REMARK Eigensystem & Euler angles for clockwise rotation about z, y',
z".
DATA EIGENVALUES (Sxx_d,Syy_d,Szz_d) -7.3905e-005 -5.9433e-004 6.6824e-004
DATA EIGENVECTORS (x_coor y_coor z_coor)
DATA EIGENVECTORS X_AXIS 7.2204e-001 5.1238e-001 4.6490e-001
DATA EIGENVECTORS Y_AXIS -1.8341e-001 7.8968e-001 -5.8547e-001
DATA EIGENVECTORS Z_AXIS 6.6710e-001 -3.3746e-001 -6.6415e-001
DATA Q_EULER_SOLUTIONS ALPHA BETA GAMMA
DATA Q_EULER_ANGLES 1 231.55 131.62 206.83
DATA Q_EULER_ANGLES 2 51.55 131.62 206.83
DATA Q_EULER_ANGLES 3 308.45 48.38 26.83
DATA Q_EULER_ANGLES 4 128.45 48.38 26.83
```

```
REMARK Euler angles (psi/theta/phi) for rotation about x, y, z.
DATA EULER_SOLUTIONS 2
DATA EULER_ANGLES 26.94 221.84 14.25
DATA EULER_ANGLES 206.94 -41.84 194.25
DATA Da 3.341183e-004
DATA Dr 1.734755e-004
DATA Aa 6.682367e-004
DATA Ar 3.469510e-004
DATA Da_HN 7.212011e+000
DATA Rhombicity 5.192038e-001
REMARK Dipolar couplings.
DATA N 48
DATA RMS 3.041
DATA Chi2 443.842
DATA CORR R 0.969
DATA Q SAUPE 0.172
DATA REGRESSION OFFSET -0.320 +/- 0.434 [Hz]
DATA REGRESSION SLOPE 0.936 +/- 0.035 [Hz]
DATA REGRESSION BAX SLOPE 0.967 +/- 0.025 [Hz]
VARS RESID_I RESNAME_I ATOMNAME_I RESID_J RESNAME_J ATOMNAME_J DI D_OBS
D D_DIFF DD W
FORMAT %4d %4s %4s %4d %4s %4s %9.2f %9.3f %9.3f %9.3f %.2f %.2f
67 LEU N 67 H -38350.80 12.1286 18.0103 -5.8817 1.0000 1.00
70 VAL N 70 H -38289.20 -12.5645 -17.1014 4.5369 1.0000 1.00
6 LYS N 6 H -38250.54 -5.6259 -1.3127 -4.3132 1.0000 1.00
45 PHE N 45 H -38275.33 -17.3288 -17.8460 0.5172 1.0000 1.00
43 LEU N 43 H -38260.30 -19.9238 -18.3379 -1.5858 1.0000 1.00
15 LEU N 15 H -38276.65 16.8878 12.0937 4.7941 1.0000 1.00
50 LEU N 50 H -38335.59 -18.1955 -15.5350 -2.6605 1.0000 1.00
5 VAL N 5 H -38258.15 5.6310 3.6117 2.0192 1.0000 1.00
44 ILE N 44 H -38288.26 -16.0262 -17.6781 1.6519 1.0000 1.00
68 HIS N 68 H -38274.68 -14.7287 -10.7349 -3.9937 1.0000 1.00
2 GLN N 2 H -38334.96 -6.9335 -9.2729 2.3393 1.0000 1.00
14 THR N 14 H -38264.76 2.6001 2.0034 0.5967 1.0000 1.00
17 VAL N 17 H -38288.70 -4.7643 -2.2956 -2.4687 1.0000 1.00
66 THR N 66 H -38322.75 16.8929 18.6563 -1.7635 1.0000 1.00
18 GLU N 18 H -38289.89 -12.9953 -11.9981 -0.9972 1.0000 1.00
4 PHE N 4 H -38267.91 12.1235 11.4392 0.6843 1.0000 1.00
27 LYS N 27 H -38307.07 -17.7596 -15.5323 -2.2273 1.0000 1.00
64 GLU N 64 H -38320.07 16.8929 15.5292 1.3637 1.0000 1.00
7 THR N 7 H -38263.76 -12.9953 -12.4664 -0.5289 1.0000 1.00
34 GLU N 34 H -38312.58 -13.4261 -19.0586 5.6324 1.0000 1.00
39 ASP N 39 H -38347.54 16.8878 14.3378 2.5500 1.0000 1.00
57 SER N 57 H -38257.26 23.3855 18.6215 4.7640 1.0000 1.00
55 THR N 55 H -38280.97 -5.6310 -1.5223 -4.1087 1.0000 1.00
35 GLY N 35 H -38288.68 6.0618 1.8261 4.2357 1.0000 1.00
```

```
3 ILE N 3 H -38317.43 12.5594 9.2997 3.2597 1.0000 1.00
60 ASN N 60 H -38339.95 2.1642 4.2984 -2.1342 1.0000 1.00
40 GLN N 40 H -38334.98 18.6263 16.2444 2.3819 1.0000 1.00
65 SER N 65 H -38339.35 6.9285 1.4378 5.4906 1.0000 1.00
59 TYR N 59 H -38353.05 13.4261 14.4532 -1.0270 1.0000 1.00
41 GLN N 41 H -38318.91 6.9285 11.3707 -4.4423 1.0000 1.00
61 ILE N 61 H -38276.63 -7.7952 -4.0846 -3.7106 1.0000 1.00
62 GLN N 62 H -38321.78 16.8929 16.5924 0.3005 1.0000 1.00
58 ASP N 58 H -38243.19 9.5285 9.8272 -0.2986 1.0000 1.00
47 GLY N 47 H -38246.38 -6.9285 -10.0747 3.1463 1.0000 1.00
20 SER N 20 H -38332.34 9.5285 5.0843 4.4442 1.0000 1.00
25 ASN N 25 H -38271.15 -1.3026 -4.7499 3.4473 1.0000 1.00
32 ASP N 32 H -38236.77 -11.6927 -9.9221 -1.7707 1.0000 1.00
52 ASP N 52 H -38311.95 0.0000 -0.2838 0.2838 1.0000 1.00
63 LYS N 63 H -38273.60 -2.6001 -0.2171 -2.3829 1.0000 1.00
23 ILE N 23 H -38277.13 -8.2310 -6.9292 -1.3019 1.0000 1.00
12 THR N 12 H -38213.81 -12.5594 -12.8058 0.2464 1.0000 1.0
30 ILE N 30 H -38341.30 -10.8311 -9.4235 -1.4076 1.0000 1.00
51 GLU N 51 H -38232.53 -5.6310 -2.8440 -2.7869 1.0000 1.00
69 LEU N 69 H -38311.90 -22.0880 -21.8844 -0.2035 1.0000 1.00
26 VAL N 26 H -38301.08 2.5950 -2.0830 4.6780 1.0000 1.00
11 LYS N 11 H -38261.09 -12.1286 -15.0582 2.9296 1.0000 1.00
36 ILE N 36 H -38296.96 -7.3542 -8.4809 1.1267 1.0000 1.00
48 ARG N 48 H -38261.30 -1.7334 2.2257 -3.9590 1.0000 1.00
```

PALES output file for shear regime 24

```
REMARK Molecular Alignment Simulation.
1_Sheared_1Hz
Rotated to approx.  70 degrees (2H LC spectra)
REMARK Simulation parameters.
DATA PALES_MODE DC
DATA TENSOR_MODE SVD (Order Matrix Method)
REMARK Order matrix.
DATA SAUPE_MATRIX S(zz) S(xx-yy) S(xy) S(xz) S(yz)
DATA SAUPE -4.6834e-005 -2.1887e-004 3.7102e-005 1.6720e-004 -1.6662e-004
DATA IRREDUCIBLE_REP A0 A1R A1I A2R A2I
DATA IRREDUCIBLE -7.4247e-005 -2.1643e-004 -2.1567e-004 -1.4166e-004
-4.8025e-005
DATA IRREDUCIBLE GENERAL_MAGNITUDE 4.8680e-004
REMARK Mapping of coordinates.
DATA MAPPING_COOR Szz_d(x) Szz_d(y) Syy_d(x) Syy_d(y) Sxx_d(x) Sxx_d(y)
DATA MAPPING -0.34563 -0.75945 1.49117 -0.60920 0.53904 0.46177
DATA MAPPING INV 1.93269 0.75945 -1.08526 0.60920 -2.27352 -0.46177
```

```
REMARK Eigensystem & Euler angles for clockwise rotation about z, y',
z".
DATA EIGENVALUES (Sxx_d,Syy_d,Szz_d) 4.0441e-005 2.4339e-004 -2.8383e-004
DATA EIGENVECTORS (x_coor y_coor z_coor)
DATA EIGENVECTORS X_AXIS 7.3783e-001 5.0705e-001 4.4554e-001
DATA EIGENVECTORS Y_AXIS -2.0089e-001 7.9512e-001 -5.7222e-001
DATA EIGENVECTORS Z_AXIS 6.4440e-001 -3.3269e-001 -6.8853e-001
DATA Q_EULER_SOLUTIONS ALPHA BETA GAMMA
DATA Q_EULER_ANGLES 1 232.10 133.51 207.31
DATA Q_EULER_ANGLES 2 52.10 133.51 207.31
DATA Q_EULER_ANGLES 3 307.90 46.49 27.31
DATA Q_EULER_ANGLES 4 127.90 46.49 27.31
REMARK Euler angles (psi/theta/phi) for rotation about x, y, z.
DATA EULER_SOLUTIONS 2
DATA EULER_ANGLES 25.79 220.12 15.23
DATA EULER_ANGLES 205.79 -40.12 195.23
DATA Da -1.419138e-004
DATA Dr -6.764876e-005
DATA Aa -2.838276e-004
DATA Ar -1.352975e-004
DATA Da_HN -3.063238e+000
DATA Rhombicity 4.766890e-001
REMARK Dipolar couplings.
DATA N 54
DATA RMS 1.812
DATA Chi2 177.280
DATA CORR R 0.932
DATA Q SAUPE 0.244
DATA REGRESSION OFFSET 0.105 +/- 0.235 [Hz]
DATA REGRESSION SLOPE 0.867 +/- 0.047 [Hz]
DATA REGRESSION BAX SLOPE 0.933 +/- 0.033 [Hz]
VARS RESID_I RESNAME_I ATOMNAME_I RESID_J RESNAME_J ATOMNAME_J DI D_OBS
D D_DIFF DD W
FORMAT %4d %4s %4s %4d %4s %4s %9.2f %9.3f %9.3f %9.3f %.2f %.2f
13 ILE N 13 H -38292.09 -0.8667 1.8358 -2.7025 1.0000 1.00
67 LEU N 67 H -38350.80 -5.6360 -7.7088 2.0728 1.0000 1.00
70 VAL N 70 H -38289.20 4.7643 7.1098 -2.3455 1.0000 1.00
6 LYS N 6 H -38250.54 2.6001 0.4600 2.1401 1.0000 1.00
45 PHE N 45 H -38275.33 7.3643 7.0052 0.3592 1.0000 1.00
43 LEU N 43 H -38260.30 7.3593 7.6722 -0.3130 1.0000 1.00
15 LEU N 15 H -38276.65 -6.9386 -4.6961 -2.2425 1.0000 1.00
50 LEU N 50 H -38335.59 4.7643 6.3645 -1.6003 1.0000 1.00
5 VAL N 5 H -38258.15 -2.1642 -1.7630 -0.4012 1.0000 1.00
44 ILE N 44 H -38288.26 7.3643 7.0668 0.2976 1.0000 1.00
68 HIS N 68 H -38274.68 4.7643 4.1469 0.6174 1.0000 1.00
2 GLN N 2 H -38334.96 5.1951 4.1990 0.9960 1.0000 1.00
```

```
14 THR N 14 H -38264.76 -0.8667 -1.0478 0.1811 1.0000 1.00
17 VAL N 17 H -38288.70 3.0309 1.4774 1.5535 1.0000 1.00
66 THR N 66 H -38322.75 -6.4977 -7.7492 1.2515 1.0000 1.00
18 GLU N 18 H -38289.89 5.1951 5.2323 -0.0372 1.0000 1.00
4 PHE N 4 H -38267.91 -3.9026 -4.7519 0.8493 1.0000 1.00
27 LYS N 27 H -38307.07 4.3284 6.2360 -1.9076 1.0000 1.00
64 GLU N 64 H -38320.07 -6.4926 -6.0701 -0.4224 1.0000 1.00
7 THR N 7 H -38263.76 6.0618 4.6931 1.3686 1.0000 1.00
34 GLU N 34 H -38312.58 6.0618 7.6627 -1.6009 1.0000 1.00
39 ASP N 39 H -38347.54 -8.6669 -5.6282 -3.0387 1.0000 1.00
57 SER N 57 H -38257.26 -9.9644 -7.5327 -2.4317 1.0000 1.00
55 THR N 55 H -38280.97 0.8667 0.8294 0.0373 1.0000 1.00
35 GLY N 35 H -38288.68 -1.7334 -0.7055 -1.0279 1.0000 1.00
3 ILE N 3 H -38317.43 -3.9026 -3.3773 -0.5254 1.0000 1.00
60 ASN N 60 H -38339.95 -0.8667 -1.6172 0.7505 1.0000 1.00
40 GLN N 40 H -38334.98 -9.0977 -7.3374 -1.7603 1.0000 1.00
65 SER N 65 H -38339.35 -2.6001 -0.4647 -2.1354 1.0000 1.00
33 LYS N 33 H -38332.41 1.7334 -2.2714 4.0048 1.0000 1.00
59 TYR N 59 H -38353.05 -8.2310 -6.0069 -2.2241 1.0000 1.00
41 GLN N 41 H -38318.91 -2.6001 -4.5561 1.9560 1.0000 1.00
61 ILE N 61 H -38276.63 3.0309 2.0732 0.9577 1.0000 1.00
54 ARG N 54 H -38277.99 -0.8667 -2.6730 1.8064 1.0000 1.00
62 GLN N 62 H -38321.78 -6.4926 -6.8515 0.3589 1.0000 1.00
58 ASP N 58 H -38243.19 -6.9285 -3.5932 -3.3353 1.0000 1.00
47 GLY N 47 H -38246.38 3.4718 3.9838 -0.5120 1.0000 1.00
20 SER N 20 H -38332.34 -5.1951 -2.7918 -2.4033 1.0000 1.00
25 ASN N 25 H -38271.15 1.2975 2.2266 -0.9291 1.0000 1.00
32 ASP N 32 H -38236.77 3.9026 4.2507 -0.3480 1.0000 1.00
52 ASP N 52 H -38311.95 -2.1642 -0.0283 -2.1359 1.0000 1.00
63 LYS N 63 H -38273.60 2.1642 0.2248 1.9394 1.0000 1.00
23 ILE N 23 H -38277.13 2.6001 2.5732 0.0268 1.0000 1.00
12 THR N 12 H -38213.81 6.5027 4.8056 1.6971 1.0000 1.00
30 ILE N 30 H -38341.30 4.7643 3.5938 1.1704 1.0000 1.00
51 GLU N 51 H -38232.53 0.0000 1.5621 -1.5621 1.0000 1.00
69 LEU N 69 H -38311.90 9.5285 8.9121 0.6165 1.0000 1.00
71 LEU N 71 H -38335.76 4.7643 3.6068 1.1575 1.0000 1.00
16 GLU N 16 H -38341.04 1.2975 -2.0400 3.3375 1.0000 1.00
26 VAL N 26 H -38301.08 -0.8667 0.7616 -1.6283 1.0000 1.00
29 ALA N 29 H -38277.41 4.7592 0.6468 4.1124 1.0000 1.00
11 LYS N 11 H -38261.09 4.3335 6.0142 -1.6808 1.0000 1.00
36 ILE N 36 H -38296.96 3.9026 3.8044 0.0982 1.0000 1.00
48 ARG N 48 H -38261.30 1.7283 -1.5779 3.3062 1.0000 1.00
```

PALES output file for shear regime 25

```
REMARK Molecular Alignment Simulation.
12Hz
REMARK Simulation parameters.
DATA PALES_MODE DC
DATA TENSOR_MODE SVD (Order Matrix Method)
REMARK Order matrix.
DATA SAUPE_MATRIX S(zz) S(xx-yy) S(xy) S(xz) S(yz)
DATA SAUPE -5.5432e-005 -1.6997e-004 4.6830e-005 1.2076e-004 -1.0846e-004
DATA IRREDUCIBLE_REP A0 A1R A1I A2R A2I
DATA IRREDUCIBLE -8.7878e-005 -1.5631e-004 -1.4039e-004 -1.1001e-004
-6.0617e-005
DATA IRREDUCIBLE GENERAL_MAGNITUDE 3.5715e-004
REMARK Mapping of coordinates.
DATA MAPPING_COOR Szz_d(x) Szz_d(y) Syy_d(x) Syy_d(y) Sxx_d(x) Sxx_d(y)
DATA MAPPING -0.33562 -0.77791 1.45646 -0.48632 0.35456 0.56763
DATA MAPPING INV 1.90240 0.77791 -1.32089 0.48632 -2.29436 -0.56763
REMARK Eigensystem & Euler angles for clockwise rotation about z, y',
z".
DATA EIGENVALUES (Sxx_d,Syy_d,Szz_d) 4.8018e-005 1.6661e-004 -2.1463e-004
DATA EIGENVECTORS (x_coor y_coor z_coor)
DATA EIGENVECTORS X_AXIS 7.6972e-001 3.4420e-001 5.3764e-001
DATA EIGENVECTORS Y_AXIS -6.7715e-002 8.8146e-001 -4.6738e-001
DATA EIGENVECTORS Z_AXIS 6.3478e-001 -3.2334e-001 -7.0179e-001
DATA Q_EULER_SOLUTIONS ALPHA BETA GAMMA
DATA Q_EULER_ANGLES 1 221.00 134.57 206.99
DATA Q_EULER_ANGLES 2 41.00 134.57 206.99
DATA Q_EULER_ANGLES 3 319.00 45.43 26.99
DATA Q_EULER_ANGLES 4 139.00 45.43 26.99
REMARK Euler angles (psi/theta/phi) for rotation about x, y, z.
DATA EULER_SOLUTIONS 2
DATA EULER_ANGLES 24.74 219.40 5.03
DATA EULER_ANGLES 204.74 -39.40 185.03
DATA Da -1.073136e-004
DATA Dr -3.953054e-005
DATA Aa -2.146272e-004
DATA Ar -7.906107e-005
DATA Da_HN -2.316386e+000
DATA Rhombicity 3.683646e-001
REMARK Dipolar couplings.
DATA N 41
DATA RMS 0.977
DATA Chi2 39.156
DATA CORR R 0.963
DATA Q SAUPE 0.179
```

```
DATA REGRESSION OFFSET 0.181 +/- 0.152 [Hz]
DATA REGRESSION SLOPE 0.919 +/- 0.041 [Hz]
DATA REGRESSION BAX SLOPE 0.955 +/- 0.029 [Hz]
VARS RESID_I RESNAME_I ATOMNAME_I RESID_J RESNAME_J ATOMNAME_J DI D_OBS
D D_DIFF DD W
FORMAT %4d %4s %4s %4d %4s %4s %9.2f %9.3f %9.3f %9.3f %.2f %.2f
13 ILE N 13 H -38292.09 -0.0051 0.8369 -0.8420 1.0000 1.00
70 VAL N 70 H -38289.20 3.8925 5.7710 -1.8785 1.0000 1.00
6 LYS N 6 H -38250.54 2.6001 0.8752 1.7249 1.0000 1.00
45 PHE N 45 H -38275.33 5.2001 4.5400 0.6602 1.0000 1.00
43 LEU N 43 H -38260.30 4.7643 5.5444 -0.7801 1.0000 1.00
15 LEU N 15 H -38276.65 -4.7693 -3.0375 -1.7318 1.0000 1.00
50 LEU N 50 H -38335.59 6.0668 5.1982 0.8686 1.0000 1.00
68 HIS N 68 H -38274.68 3.8976 3.1172 0.7804 1.0000 1.00
2 GLN N 2 H -38334.96 3.0309 2.6344 0.3965 1.0000 1.00
14 THR N 14 H -38264.76 -0.8667 -0.5014 -0.3653 1.0000 1.00
17 VAL N 17 H -38288.70 0.4308 0.6916 -0.2608 1.0000 1.00
66 THR N 66 H -38322.75 -5.1951 -5.5847 0.3896 1.0000 1.00
18 GLU N 18 H -38289.89 3.4617 3.1720 0.2897 1.0000 1.00
4 PHE N 4 H -38267.91 -3.4668 -3.1437 -0.3230 1.0000 1.00
27 LYS N 27 H -38307.07 5.1951 4.7853 0.4098 1.0000 1.00
64 GLU N 64 H -38320.07 -4.7592 -4.5076 -0.2516 1.0000 1.00
7 THR N 7 H -38263.76 3.8976 2.9338 0.9638 1.0000 1.00
34 GLU N 34 H -38312.58 5.6310 5.5207 0.1103 1.0000 1.00
57 SER N 57 H -38257.26 -7.3643 -5.7157 -1.6487 1.0000 1.00
55 THR N 55 H -38280.97 2.1642 1.5599 0.6043 1.0000 1.00
35 GLY N 35 H -38288.68 -0.8667 0.3715 -1.2382 1.0000 1.00
3 ILE N 3 H -38317.43 -2.6051 -2.1623 -0.4428 1.0000 1.00
40 GLN N 40 H -38334.98 -6.4977 -5.8985 -0.5991 1.0000 1.00
33 LYS N 33 H -38332.41 0.8718 -1.2600 2.1318 1.0000 1.00
41 GLN N 41 H -38318.91 -3.0360 -3.4291 0.3931 1.0000 1.00
61 ILE N 61 H -38276.63 1.7334 1.0129 0.7204 1.0000 1.00
54 ARG N 54 H -38277.99 -1.3026 -1.2892 -0.0133 1.0000 1.00
62 GLN N 62 H -38321.78 -3.4617 -5.0416 1.5799 1.0000 1.00
47 GLY N 47 H -38246.38 1.7334 3.2779 -1.5445 1.0000 1.00
20 SER N 20 H -38332.34 -3.8976 -2.8496 -1.0479 1.0000 1.00
25 ASN N 25 H -38271.15 2.6001 2.7686 -0.1685 1.0000 1.00
32 ASP N 32 H -38236.77 5.2001 4.1852 1.0149 1.0000 1.00
52 ASP N 52 H -38311.95 0.0051 -0.1713 0.1764 1.0000 1.00
23 ILE N 23 H -38277.13 1.2975 2.0208 -0.7233 1.0000 1.00
12 THR N 12 H -38213.81 3.8976 2.8592 1.0384 1.0000 1.00
30 ILE N 30 H -38341.30 2.1642 2.7115 -0.5473 1.0000 1.00
69 LEU N 69 H -38311.90 5.6310 6.2629 -0.6319 1.0000 1.00
71 LEU N 71 H -38335.76 2.6001 2.9533 -0.3533 1.0000 1.00
26 VAL N 26 H -38301.08 -0.0051 1.0773 -1.0824 1.0000 1.00
29 ALA N 29 H -38277.41 0.4257 1.3900 -0.9642 1.0000 1.00
```

```
11 LYS N 11 H -38261.09 1.7334 3.3704 -1.6370 1.0000 1.00
```

D. Further Shear Profiles

D.1. No Applied Shear (Repeated)

Alignment Tensor

$$\begin{bmatrix} 1.993 \times 10^{-4} & -7.881 \times 10^{-5} & -4.060 \times 10^{-4} \\ -7.881 \times 10^{-5} & -2.824 \times 10^{-4} & 3.769 \times 10^{-4} \\ -4.060 \times 10^{-4} & 3.769 \times 10^{-4} & 8.308 \times 10^{-5} \end{bmatrix} \tag{D.1}$$

PALES output file

```
REMARK Molecular Alignment Simulation.
2_Aligned_After_High_Shear_2
REMARK Simulation parameters.
DATA PALES_MODE DC
DATA TENSOR_MODE SVD (Order Matrix Method)
REMARK Order matrix.
DATA SAUPE_MATRIX S(zz) S(xx-yy) S(xy) S(xz) S(yz)
DATA SAUPE 8.3083e-005 4.8162e-004 -7.8806e-005 -4.0604e-004 3.7688e-004
DATA IRREDUCIBLE_REP A0 A1R A1I A2R A2I
DATA IRREDUCIBLE 1.3171e-004 5.2558e-004 4.8784e-004 3.1171e-004 1.0201e-004
DATA IRREDUCIBLE GENERAL_MAGNITUDE 1.1229e-003
REMARK Mapping of coordinates.
DATA MAPPING_COOR Szz_d(x) Szz_d(y) Syy_d(x) Syy_d(y) Sxx_d(x) Sxx_d(y)
DATA MAPPING -0.33915 -0.74624 -1.00415 0.64730 0.60679 0.43223
DATA MAPPING INV 1.96756 0.74624 1.50196 -0.64730 -2.24589 -0.43223
REMARK Eigensystem & Euler angles for clockwise rotation about z, y',
z".
DATA EIGENVALUES (Sxx_d,Syy_d,Szz_d) -1.0158e-004 -5.5629e-004 6.5787e-004
DATA EIGENVECTORS (x_coor y_coor z_coor)
```

Table D.1.: **RDCs captured while under no shear (Repeated):** RDCs captured from the N-H bonds of ubiquitin

Amino Acid	Residue Number	J-coupling + RDC [Hz][±0.05]	RDC [Hz][±0.05]	Amino Acid	Residue Number	J-coupling + RDC [Hz][±0.05]	RDC [Hz][±0.05]
GLN	2	86.19	-6.93	GLN	40	111.32	18.19
ILE	3	104.38	10.82	GLN	41	100.92	6.06
PHE	4	106.12	12.13	LEU	43	79.70	-16.03
VAL	5	98.33	5.20	ILE	44	74.50	-18.19
LYS	6	89.66	-3.90	PHE	45	80.13	-13.43
THR	7	82.30	-12.13	GLY	47	87.93	-5.20
LYS	11	82.73	-11.69	ARG	48	92.26	-0.87
THR	12	80.56	-12.13	LEU	50	84.90	-11.26
ILE	13	96.16	3.03	GLU	51	90.96	-4.33
THR	14	96.16	2.60	ASP	52	93.99	-0.86
LEU	15	108.29	12.99	ARG	54	90.09	-5.64
GLU	16	91.82	-2.17	THR	55	90.10	-3.03
VAL	17	88.36	-5.63	SER	57	116.09	22.09
GLU	18	81.43	-11.70	ASP	58	107.85	9.09
SER	20	102.22	9.53	TYR	59	112.61	16.89
ILE	23	87.93	-6.50	ASN	60	97.02	2.60
ASN	25	93.99	-0.43	ILE	61	86.62	-6.93
VAL	26	94.86	2.16	GLN	62	112.18	17.76
LYS	27	81.00	-16.03	LYS	63	90.09	-3.90
SER	28	123.01	26.42	GLU	64	109.58	15.60
ALA	29	84.46	-10.83	SER	65	100.05	5.20
ILE	30	83.60	-10.83	THR	66	107.42	15.16
ASP	32	86.20	-8.23	LEU	67	105.69	11.69
LYS	33	90.96	-3.03	HIS	68	80.57	-14.72
GLU	34	77.97	-13.00	LEU	69	73.63	-19.92
GLY	35	97.89	3.90	VAL	70	83.60	-10.83
ILE	36	80.13	-11.26	LEU	71	79.70	-16.89
ASP	39	110.01	15.15				

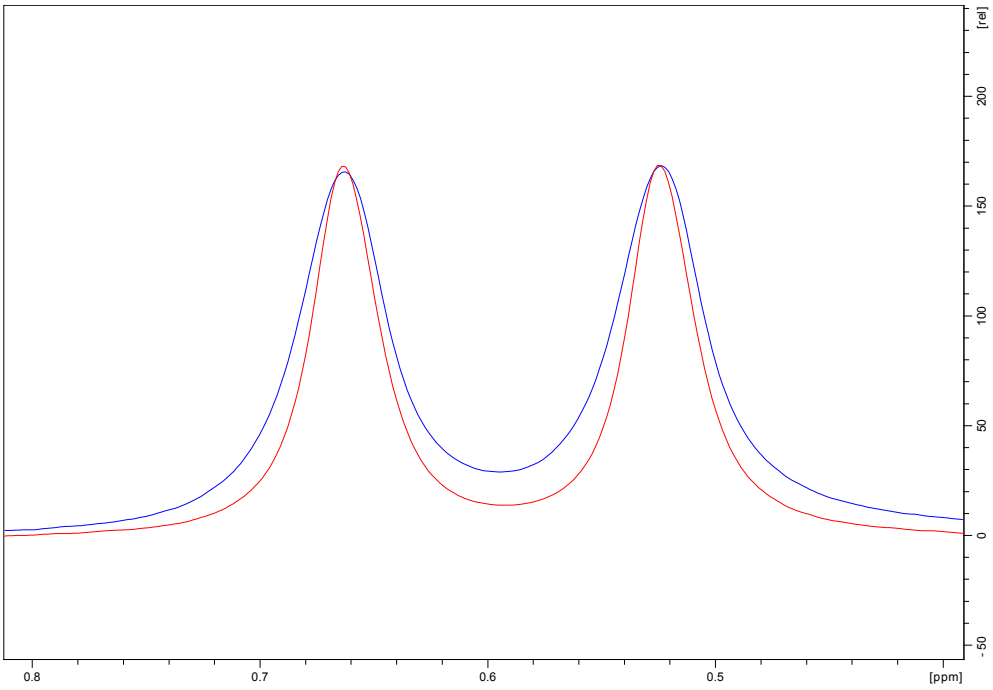

Figure D.1.: **^{2}H spectra while under no shear (Repeated):** The blue spectrum was conducted before the IPAP-HSQC. The red spectrum was captured directly after the IPAP-HSQC.

```
DATA EIGENVECTORS X_AXIS 7.1273e-001 5.6262e-001 4.1889e-001
DATA EIGENVECTORS Y_AXIS 2.4489e-001 -7.5920e-001 6.0303e-001
DATA EIGENVECTORS Z_AXIS 6.5730e-001 -3.2722e-001 -6.7888e-001
DATA Q_EULER_SOLUTIONS ALPHA BETA GAMMA
DATA Q_EULER_ANGLES 1 55.21 132.76 206.46
DATA Q_EULER_ANGLES 2 235.21 132.76 206.46
DATA Q_EULER_ANGLES 3 124.79 47.24 26.46
DATA Q_EULER_ANGLES 4 304.79 47.24 26.46
REMARK Euler angles (psi/theta/phi) for rotation about x, y, z.
DATA EULER_SOLUTIONS 2
DATA EULER_ANGLES 25.73 221.09 18.96
DATA EULER_ANGLES 205.73 -41.09 198.96
DATA Da 3.289340e-004
DATA Dr 1.515676e-004
DATA Aa 6.578680e-004
DATA Ar 3.031352e-004
DATA Da_HN 7.100107e+000
DATA Rhombicity 4.607841e-001
REMARK Dipolar couplings.
DATA N 46
DATA RMS 2.688
DATA Chi2 332.477
DATA CORR R 0.970
DATA Q SAUPE 0.157
DATA REGRESSION OFFSET -0.238 +/- 0.393 [Hz]
DATA REGRESSION SLOPE 0.940 +/- 0.035 [Hz]
DATA REGRESSION BAX SLOPE 0.969 +/- 0.025 [Hz]
VARS RESID_I RESNAME_I ATOMNAME_I RESID_J RESNAME_J ATOMNAME_J DI D_OBS
D D_DIFF DD W
FORMAT %4d %4s %4s %4d %4s %4s %9.2f %9.3f %9.3f %9.3f %.2f %.2f
6 LYS N 6 H -38250.54 -3.8976 -0.0926 -3.8050 1.0000 1.00
45 PHE N 45 H -38275.33 -13.4261 -15.8505 2.4244 1.0000 1.00
43 LEU N 43 H -38260.30 -16.0262 -16.9777 0.9515 1.0000 1.00
15 LEU N 15 H -38276.65 12.9902 11.2380 1.7523 1.0000 1.00
50 LEU N 50 H -38335.59 -11.2619 -13.5724 2.3105 1.0000 1.00
5 VAL N 5 H -38258.15 5.2001 4.8621 0.3380 1.0000 1.00
44 ILE N 44 H -38288.26 -18.1904 -15.4784 -2.7120 1.0000 1.00
2 GLN N 2 H -38334.96 -6.9335 -10.7705 3.8369 1.0000 1.00
14 THR N 14 H -38264.76 2.6001 3.2751 -0.6750 1.0000 1.00
17 VAL N 17 H -38288.70 -5.6310 -3.8882 -1.7427 1.0000 1.00
66 THR N 66 H -38322.75 15.1595 18.3851 -3.2256 1.0000 1.00
18 GLU N 18 H -38289.89 -11.6978 -13.1791 1.4813 1.0000 1.00
4 PHE N 4 H -38267.91 12.1286 11.6614 0.4672 1.0000 1.00
27 LYS N 27 H -38307.07 -16.0262 -13.3967 -2.6295 1.0000 1.00
64 GLU N 64 H -38320.07 15.5954 14.1733 1.4221 1.0000 1.00
7 THR N 7 H -38263.76 -12.1286 -10.4488 -1.6798 1.0000 1.00
```

```
34 GLU N 34 H -38312.58 -12.9953 -16.8725 3.8772 1.0000 1.00
39 ASP N 39 H -38347.54 15.1544 13.3327 1.8217 1.0000 1.00
57 SER N 57 H -38257.26 22.0930 17.6308 4.4623 1.0000 1.00
55 THR N 55 H -38280.97 -3.0309 -1.0776 -1.9533 1.0000 1.00
35 GLY N 35 H -38288.68 3.8976 1.7474 2.1502 1.0000 1.00
3 ILE N 3 H -38317.43 10.8210 7.8931 2.9279 1.0000 1.00
60 ASN N 60 H -38339.95 2.6001 4.2175 -1.6174 1.0000 1.00
40 GLN N 40 H -38334.98 18.1904 16.8555 1.3349 1.0000 1.00
65 SER N 65 H -38339.35 5.1951 1.6464 3.5487 1.0000 1.00
59 TYR N 59 H -38353.05 16.8878 14.4841 2.4037 1.0000 1.00
41 GLN N 41 H -38318.91 6.0618 10.8734 -4.8116 1.0000 1.00
61 ILE N 61 H -38276.63 -6.9335 -4.7596 -2.1739 1.0000 1.00
62 GLN N 62 H -38321.78 17.7596 16.0970 1.6626 1.0000 1.00
58 ASP N 58 H -38243.19 9.0927 8.3636 0.7290 1.0000 1.00
47 GLY N 47 H -38246.38 -5.1951 -8.1708 2.9757 1.0000 1.00
20 SER N 20 H -38332.34 9.5336 5.9322 3.6014 1.0000 1.00
25 ASN N 25 H -38271.15 -0.4308 -4.3756 3.9448 1.0000 1.00
32 ASP N 32 H -38236.77 -8.2260 -8.7999 0.5739 1.0000 1.00
52 ASP N 52 H -38311.95 -0.8616 -1.1999 0.3383 1.0000 1.00
63 LYS N 63 H -38273.60 -3.9026 -0.7697 -3.1329 1.0000 1.00
23 ILE N 23 H -38277.13 -6.4977 -5.0505 -1.4472 1.0000 1.00
12 THR N 12 H -38213.81 -12.1286 -10.9099 -1.2187 1.0000 1.00
30 ILE N 30 H -38341.30 -10.8260 -7.4181 -3.4080 1.0000 1.00
51 GLU N 51 H -38232.53 -4.3335 -3.8669 -0.4666 1.0000 1.00
69 LEU N 69 H -38311.90 -19.9238 -19.9004 -0.0234 1.0000 1.00
16 GLU N 16 H -38341.04 -2.1693 4.5622 -6.7314 1.0000 1.00
26 VAL N 26 H -38301.08 2.1642 -0.7778 2.9420 1.0000 1.00
11 LYS N 11 H -38261.09 -11.6927 -14.9077 3.2150 1.0000 1.00
36 ILE N 36 H -38296.96 -11.2569 -9.9725 -1.2843 1.0000 1.00
48 ARG N 48 H -38261.30 -0.8667 2.9174 -3.7841 1.0000 1.00
```

D.2. Shear at an average rate of 1.80 s^{-1}

Alignment Tensor

$$\begin{bmatrix} -6.82 \times 10^{-5} & 4.20 \times 10^{-5} & 1.44 \times 10^{-4} \\ 4.20 \times 10^{-5} & 1.17 \times 10^{-4} & -1.40 \times 10^{-4} \\ 1.44 \times 10^{-4} & -1.40 \times 10^{-4} & -4.86 \times 10^{-5} \end{bmatrix} \tag{D.2}$$

PALES output file

```
REMARK Molecular Alignment Simulation
```

Table D.2.: **RDCs captured while under an average shear rate of 1.80 s^{-1}:** RDCs captured from the N-H bonds of ubiquitin

Amino Acid	Residue Number	J-Coupling + RDC [Hz][±0.05]	RDC [Hz][±0.05]	Amino Acid	Residue Number	J-Coupling + RDC [Hz][±0.05]	RDC [Hz][±0.05]
GLN	2	97.02	3.90	GLN	40	84.90	-8.23
ILE	3	90.10	-3.47	GLN	41	92.69	-2.17
PHE	4	90.09	-3.90	LEU	43	100.49	4.76
VAL	5	90.53	-2.60	ILE	44	99.62	6.93
LYS	6	96.16	2.60	PHE	45	100.05	6.50
THR	7	98.75	4.33	GLY	47	95.72	2.60
LYS	11	97.89	3.47	ARG	48	93.99	0.87
THR	12	97.45	4.76	LEU	50	102.65	6.49
ILE	13	92.70	-0.43	GLU	51	93.99	-1.30
THR	14	92.69	-0.87	ASP	52	93.56	-1.30
LEU	15	89.66	-5.64	ARG	54	94.86	-0.87
GLU	16	95.29	1.30	THR	55	93.99	0.86
VAL	17	96.16	2.16	SER	57	86.19	-7.80
GLU	18	97.89	4.76	ASP	58	91.82	-6.93
SER	20	89.66	-3.03	TYR	59	86.19	-9.53
ILE	23	97.02	2.60	ASN	60	93.13	-1.30
ASN	25	97.45	3.03	ILE	61	96.59	3.03
VAL	26	92.26	-0.44	GLN	62	87.50	-6.93
LYS	27	100.49	3.46	LYS	63	94.86	0.87
SER	28	85.33	-11.26	GLU	64	87.50	-6.49
ALA	29	98.76	3.46	SER	65	92.69	-2.17
ILE	30	98.32	3.90	THR	66	86.19	-6.07
ASP	32	97.89	3.47	LEU	67	89.66	-4.33
LYS	33	94.85	0.87	HIS	68	100.49	5.20
GLU	34	97.02	6.06	LEU	69	100.92	7.36
GLY	35	93.13	-0.87	VAL	70	99.19	4.76
ILE	36	93.99	2.60	LEU	71	101.79	5.20
ASP	39	88.79	-6.07				

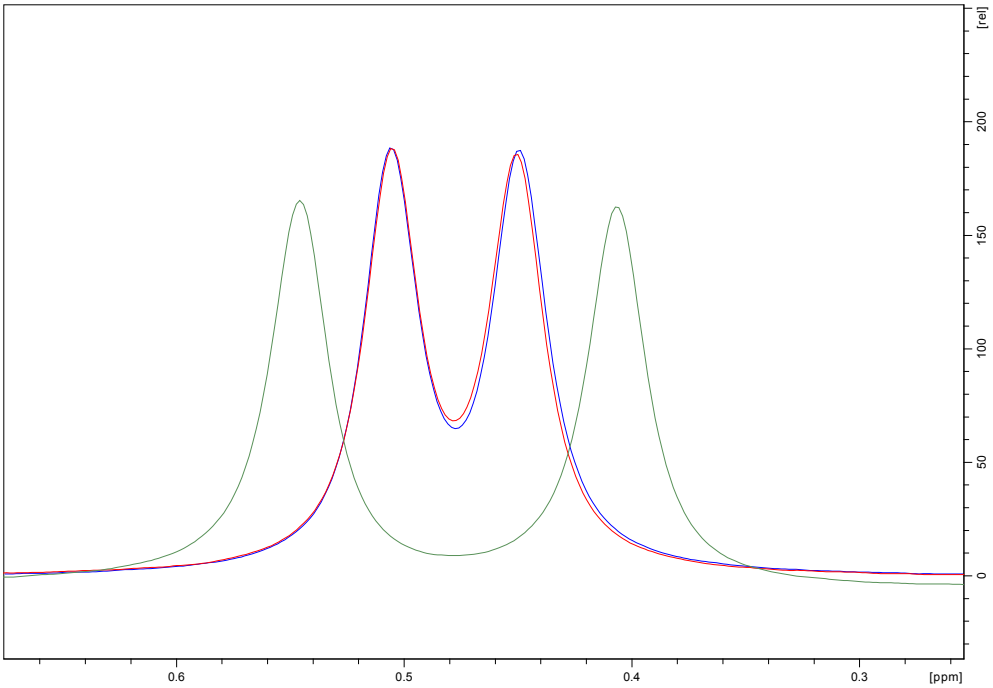

Figure D.2.: **^{2}H spectra while under an average shear rate of 1.80 s^{-1}:** The blue spectrum was conducted before the IPAP-HSQC. The red spectrum was captured directly after the IPAP-HSQC. The green spectrum was captured before the application of any shear forces and is used to calculate the angle of the liquid crystals director.

```
0.1Hz_Shear
REMARK Simulation parameters.
DATA PALES_MODE DC
DATA TENSOR_MODE SVD (Order Matrix Method)
REMARK Order matrix.
DATA SAUPE_MATRIX S(zz) S(xx-yy) S(xy) S(xz) S(yz)
DATA SAUPE -4.8578e-005 -1.8492e-004 4.1958e-005 1.4380e-004 -1.3976e-004
DATA IRREDUCIBLE_REP A0 A1R A1I A2R A2I
DATA IRREDUCIBLE -7.7013e-005 -1.8614e-004 -1.8091e-004 -1.1968e-004
-5.4312e-005
DATA IRREDUCIBLE GENERAL_MAGNITUDE 4.1861e-004
REMARK Mapping of coordinates.
DATA MAPPING_COOR Szz_d(x) Szz_d(y) Syy_d(x) Syy_d(y) Sxx_d(x) Sxx_d(y)
DATA MAPPING -0.35309 -0.76804 1.47812 -0.58324 0.48902 0.48099
DATA MAPPING INV 1.90657 0.76804 -1.14411 0.58324 -2.29613 -0.48099
REMARK Eigensystem & Euler angles for clockwise rotation about z, y',
z".
DATA EIGENVALUES (Sxx_d,Syy_d,Szz_d) 4.5761e-005 2.0234e-004 -2.4810e-004
DATA EIGENVECTORS (x_coor y_coor z_coor)
DATA EIGENVECTORS X_AXIS 7.5505e-001 4.6459e-001 4.6265e-001
DATA EIGENVECTORS Y_AXIS -1.6589e-001 8.1803e-001 -5.5073e-001
DATA EIGENVECTORS Z_AXIS 6.3433e-001 -3.3908e-001 -6.9473e-001
DATA Q_EULER_SOLUTIONS ALPHA BETA GAMMA
DATA Q_EULER_ANGLES 1 229.97 134.01 208.13
DATA Q_EULER_ANGLES 2 49.97 134.01 208.13
DATA Q_EULER_ANGLES 3 310.03 45.99 28.13
DATA Q_EULER_ANGLES 4 130.03 45.99 28.13
REMARK Euler angles (psi/theta/phi) for rotation about x, y, z.
DATA EULER_SOLUTIONS 2
DATA EULER_ANGLES 26.02 219.37 12.39
DATA EULER_ANGLES 206.02 -39.37 192.39
DATA Da -1.240483e-004
DATA Dr -5.219151e-005
DATA Aa -2.480967e-004
DATA Ar -1.043830e-004
DATA Da_HN -2.677608e+000
DATA Rhombicity 4.207353e-001
REMARK Dipolar couplings.
DATA N 47
DATA RMS 1.210
DATA Chi2 68.757
DATA CORR R 0.960
DATA Q SAUPE 0.189
DATA REGRESSION OFFSET 0.187 +/- 0.172 [Hz]
DATA REGRESSION SLOPE 0.916 +/- 0.040 [Hz]
DATA REGRESSION BAX SLOPE 0.955 +/- 0.028 [Hz]
```

```
VARS RESID_I RESNAME_I ATOMNAME_I RESID_J RESNAME_J ATOMNAME_J DI D_OBS
D D_DIFF DD W
FORMAT %4d %4s %4s %4d %4s %4s %9.2f %9.3f %9.3f %9.3f %.2f %.2f
13 ILE N 13 H -38292.09 -0.4308 1.4304 -1.8612 1.0000 1.00
67 LEU N 67 H -38350.80 -4.3335 -6.5756 2.2421 1.0000 1.00
70 VAL N 70 H -38289.20 4.7592 6.2692 -1.5100 1.0000 1.00
6 LYS N 6 H -38250.54 2.6001 0.7154 1.8847 1.0000 1.00
45 PHE N 45 H -38275.33 6.4977 5.8069 0.6908 1.0000 1.00
43 LEU N 43 H -38260.30 4.7592 6.4584 -1.6992 1.0000 1.00
15 LEU N 15 H -38276.65 -5.6360 -3.7360 -1.9000 1.0000 1.00
50 LEU N 50 H -38335.59 6.4926 5.6891 0.8034 1.0000 1.00
5 VAL N 5 H -38258.15 -2.6001 -1.3494 -1.2507 1.0000 1.00
44 ILE N 44 H -38288.26 6.9335 6.0624 0.8711 1.0000 1.00
68 HIS N 68 H -38274.68 5.1951 3.6509 1.5442 1.0000 1.00
2 GLN N 2 H -38334.96 3.8976 3.5375 0.3601 1.0000 1.00
14 THR N 14 H -38264.76 -0.8667 -0.6910 -0.1757 1.0000 1.00
17 VAL N 17 H -38288.70 2.1642 1.1914 0.9728 1.0000 1.00
66 THR N 66 H -38322.75 -6.0668 -6.5326 0.4658 1.0000 1.00
18 GLU N 18 H -38289.89 4.7592 4.3210 0.4382 1.0000 1.00
4 PHE N 4 H -38267.91 -3.9026 -3.8257 -0.0769 1.0000 1.00
27 LYS N 27 H -38307.07 3.4617 5.4692 -2.0075 1.0000 1.00
64 GLU N 64 H -38320.07 -6.4926 -5.1809 -1.3117 1.0000 1.00
7 THR N 7 H -38263.76 4.3284 3.8747 0.4537 1.0000 1.00
34 GLU N 34 H -38312.58 6.0618 6.5501 -0.4884 1.0000 1.00
39 ASP N 39 H -38347.54 -6.0668 -4.6080 -1.4588 1.0000 1.00
57 SER N 57 H -38257.26 -7.8002 -6.6094 -1.1908 1.0000 1.00
55 THR N 55 H -38280.97 0.8616 1.2106 -0.3490 1.0000 1.00
35 GLY N 35 H -38288.68 -0.8667 -0.3770 -0.4897 1.0000 1.00
3 ILE N 3 H -38317.43 -3.4668 -2.6375 -0.8292 1.0000 1.00
60 ASN N 60 H -38339.95 -1.2975 -1.5505 0.2530 1.0000 1.00
40 GLN N 40 H -38334.98 -8.2310 -6.5046 -1.7264 1.0000 1.00
65 SER N 65 H -38339.35 -2.1693 -0.5003 -1.6689 1.0000 1.00
33 LYS N 33 H -38332.41 0.8667 -1.6719 2.5386 1.0000 1.00
41 GLN N 41 H -38318.91 -2.1693 -4.0995 1.9303 1.0000 1.00
61 ILE N 61 H -38276.63 3.0309 1.5313 1.4996 1.0000 1.00
54 ARG N 54 H -38277.99 -0.8667 -2.1898 1.3231 1.0000 1.00
62 GLN N 62 H -38321.78 -6.9285 -6.0551 -0.8734 1.0000 1.00
47 GLY N 47 H -38246.38 2.6001 3.6269 -1.0268 1.0000 1.00
20 SER N 20 H -38332.34 -3.0309 -2.7040 -0.3269 1.0000 1.00
25 ASN N 25 H -38271.15 3.0309 2.4550 0.5759 1.0000 1.00
32 ASP N 32 H -38236.77 3.4668 4.1083 -0.6416 1.0000 1.00
52 ASP N 52 H -38311.95 -1.2975 -0.0721 -1.2254 1.0000 1.00
63 LYS N 63 H -38273.60 0.8667 0.5219 0.3448 1.0000 1.00
23 ILE N 23 H -38277.13 2.6001 2.3379 0.2622 1.0000 1.00
12 THR N 12 H -38213.81 4.7643 3.9058 0.8585 1.0000 1.00
30 ILE N 30 H -38341.30 3.8976 3.1815 0.7161 1.0000 1.00
```

Table D.3.: **RDCs captured while under shear at an average rate of 0.72 s^{-1}:** RDCs captured from the N-H bonds of ubiquitin

Amino Acid	Residue Number	J-Coupling + RDC [Hz][±0.05]	RDC [Hz][±0.05]	Amino Acid	Residue Number	J-Coupling + RDC [Hz][±0.05]	RDC [Hz][±0.05]
GLN	2	89.23	-3.90	ASP	39	107.42	12.56
ILE	3	100.49	6.92	GLN	40	97.89	4.76
PHE	4	103.95	9.96	GLN	41	99.62	4.76
VAL	5	96.59	3.47	LEU	43	82.73	-13.00
LYS	6	90.96	-2.60	ILE	44	87.50	-5.20
THR	7	85.76	-8.66	PHE	45	83.60	-9.96
LEU	8	84.90	-9.53	GLY	47	89.23	-3.89
LYS	11	87.93	-6.50	LEU	50	90.10	-6.06
THR	12	81.43	-11.26	GLU	51	78.40	-16.89
ILE	13	96.59	3.47	ASP	52	91.83	-3.03
THR	14	94.42	0.87	ARG	54	92.70	-3.03
LEU	15	105.69	10.40	THR	55	90.53	-2.60
GLU	16	92.70	-1.30	SER	57	110.89	16.89
VAL	17	89.23	-4.76	ASP	58	102.22	3.46
GLU	18	84.90	-8.23	TYR	59	104.38	8.66
SER	20	99.19	6.50	ASN	60	95.72	1.30
ILE	23	89.22	-5.20	ILE	61	89.22	-4.33
ASN	25	93.99	-0.43	GLN	62	105.69	11.26
VAL	26	93.99	1.30	LYS	63	91.82	-2.17
LYS	27	85.76	-11.26	GLU	64	99.62	5.63
SER	28	111.32	14.72	SER	65	99.62	4.76
ALA	29	91.39	-3.90	THR	66	104.39	12.13
ILE	30	87.93	-6.50	LEU	67	100.92	6.93
ASP	32	91.83	-2.60	HIS	68	86.63	-8.66
LYS	33	93.99	0.01	LEU	69	96.59	3.03
GLU	34	84.46	-6.50	VAL	70	86.63	-7.80
GLY	35	96.16	2.16	LEU	71	86.20	-10.39

```
69 LEU N 69 H -38311.90 7.3643 7.5232 -0.1589 1.0000 1.00
26 VAL N 26 H -38301.08 -0.4359 0.9634 -1.3993 1.0000 1.00
11 LYS N 11 H -38261.09 3.4668 4.8048 -1.3380 1.0000 1.00
36 ILE N 36 H -38296.96 2.6001 3.2436 -0.6435 1.0000 1.00
```

D.3. Shear at an average rate of 0.72 s^{-1}

Alignment Tensor

$$\begin{bmatrix} 1.20 \times 10^{-4} & -3.43 \times 10^{-5} & -2.27 \times 10^{-4} \\ -3.43 \times 10^{-5} & -1.52 \times 10^{-4} & 2.53 \times 10^{-4} \\ -2.27 \times 10^{-4} & 2.53 \times 10^{-4} & 3.16 \times 10^{-5} \end{bmatrix} \tag{D.3}$$

PALES output file

```
REMARK Molecular Alignment Simulation.
GearBox 2Hz
```

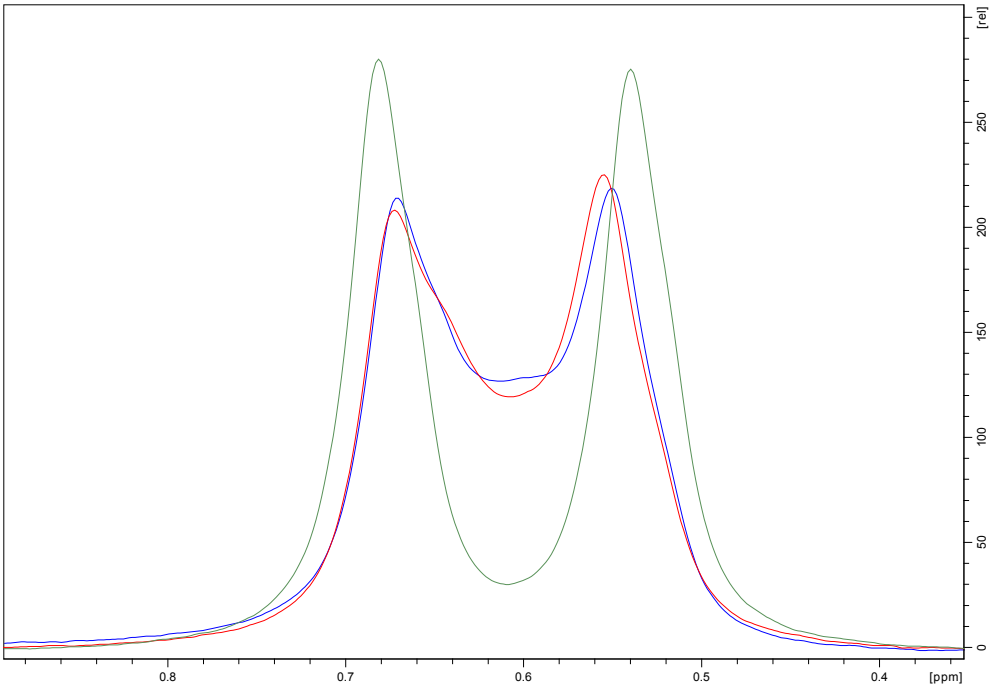

Figure D.3.: **^{2}H spectra while under shear at an average rate of 0.72 s^{-1}:** The blue spectrum was conducted before the IPAP-HSQC. The red spectrum was captured directly after the IPAP-HSQC. The green spectrum was captured before the application of any shear forces and is used to calculate the angle of the liquid crystals director.

```
REMARK Simulation parameters.
DATA PALES_MODE DC
DATA TENSOR_MODE SVD (Order Matrix Method)
REMARK Order matrix.
DATA SAUPE_MATRIX S(zz) S(xx-yy) S(xy) S(xz) S(yz)
DATA SAUPE 3.1613e-005 2.7248e-004 -3.4325e-005 -2.2674e-004 2.5312e-004
DATA IRREDUCIBLE_REP A0 A1R A1I A2R A2I
DATA IRREDUCIBLE 5.0118e-005 2.9349e-004 3.2765e-004 1.7635e-004 4.4431e-005
DATA IRREDUCIBLE GENERAL_MAGNITUDE 6.7501e-004
REMARK Mapping of coordinates.
DATA MAPPING_COOR Szz_d(x) Szz_d(y) Syy_d(x) Syy_d(y) Sxx_d(x) Sxx_d(y)
DATA MAPPING -0.38011 -0.74538 -0.97361 0.67797 0.61064 0.39289
DATA MAPPING INV 1.92843 0.74538 1.47321 -0.67797 -2.29159 -0.39289
REMARK Eigensystem & Euler angles for clockwise rotation about z, y',
z".
DATA EIGENVALUES (Sxx_d,Syy_d,Szz_d) -2.5304e-005 -3.5544e-004 3.8074e-004
DATA EIGENVECTORS (x_coor y_coor z_coor)
DATA EIGENVECTORS X_AXIS 7.2923e-001 5.6713e-001 3.8286e-001
DATA EIGENVECTORS Y_AXIS 2.4553e-001 -7.3913e-001 6.2721e-001
DATA EIGENVECTORS Z_AXIS 6.3869e-001 -3.6338e-001 -6.7825e-001
DATA Q_EULER_SOLUTIONS ALPHA BETA GAMMA
DATA Q_EULER_ANGLES 1 58.60 132.71 209.64
DATA Q_EULER_ANGLES 2 238.60 132.71 209.64
DATA Q_EULER_ANGLES 3 121.40 47.29 29.64
DATA Q_EULER_ANGLES 4 301.40 47.29 29.64
REMARK Euler angles (psi/theta/phi) for rotation about x, y, z.
DATA EULER_SOLUTIONS 2
DATA EULER_ANGLES 28.18 219.69 18.61
DATA EULER_ANGLES 208.18 -39.69 198.61
DATA Da 1.903706e-004
DATA Dr 1.100443e-004
DATA Aa 3.807411e-004
DATA Ar 2.200885e-004
DATA Da_HN 4.109187e+000
DATA Rhombicity 5.780530e-001
REMARK Dipolar couplings.
DATA N 46
DATA RMS 2.569
DATA Chi2 303.482
DATA CORR R 0.928
DATA Q SAUPE 0.249
DATA REGRESSION OFFSET 0.109 +/- 0.361 [Hz]
DATA REGRESSION SLOPE 0.863 +/- 0.052 [Hz]
DATA REGRESSION BAX SLOPE 0.933 +/- 0.037 [Hz]
VARS RESID_I RESNAME_I ATOMNAME_I RESID_J RESNAME_J ATOMNAME_J DI D_OBS
D D_DIFF DD W
```

```
FORMAT %4d %4s %4s %4d %4s %4s %9.2f %9.3f %9.3f %9.3f %.2f %.2f
67 LEU N 67 H -38350.80 6.9285 10.0324 -3.1039 1.0000 1.00
70 VAL N 70 H -38289.20 -7.8002 -8.9063 1.1061 1.0000 1.00
6 LYS N 6 H -38250.54 -2.6001 -0.4434 -2.1567 1.0000 1.00
45 PHE N 45 H -38275.33 -9.9593 -10.6313 0.6720 1.0000 1.00
43 LEU N 43 H -38260.30 -12.9953 -10.2870 -2.7083 1.0000 1.00
15 LEU N 15 H -38276.65 10.3952 6.5979 3.7973 1.0000 1.00
50 LEU N 50 H -38335.59 -6.0618 -8.2048 2.1430 1.0000 1.00
5 VAL N 5 H -38258.15 3.4668 2.0608 1.4060 1.0000 1.00
68 HIS N 68 H -38274.68 -8.6618 -6.0040 -2.6579 1.0000 1.00
8 LEU N 8 H -38323.86 -9.5285 -8.0776 -1.4510 1.0000 1.00
2 GLN N 2 H -38334.96 -3.8976 -6.3173 2.4197 1.0000 1.00
14 THR N 14 H -38264.76 0.8667 1.2226 -0.3559 1.0000 1.00
17 VAL N 17 H -38288.70 -4.7643 -2.4266 -2.3377 1.0000 1.00
66 THR N 66 H -38322.75 12.1286 10.3461 1.7825 1.0000 1.00
18 GLU N 18 H -38289.89 -8.2310 -7.9989 -0.2321 1.0000 1.00
4 PHE N 4 H -38267.91 9.9593 6.4355 3.5238 1.0000 1.00
27 LYS N 27 H -38307.07 -11.2619 -8.5410 -2.7209 1.0000 1.00
64 GLU N 64 H -38320.07 5.6310 8.1974 -2.5665 1.0000 1.00
7 THR N 7 H -38263.76 -8.6618 -7.4775 -1.1843 1.0000 1.00
34 GLU N 34 H -38312.58 -6.4977 -10.8088 4.3111 1.0000 1.00
39 ASP N 39 H -38347.54 12.5594 7.7538 4.8056 1.0000 1.00
55 THR N 55 H -38280.97 -2.6001 -0.3015 -2.2986 1.0000 1.00
35 GLY N 35 H -38288.68 2.1642 2.4979 -0.3338 1.0000 1.00
3 ILE N 3 H -38317.43 6.9234 4.7969 2.1265 1.0000 1.00
60 ASN N 60 H -38339.95 1.2975 2.8263 -1.5288 1.0000 1.00
40 GLN N 40 H -38334.98 4.7643 9.0213 -4.2570 1.0000 1.00
65 SER N 65 H -38339.35 4.7592 1.5013 3.2579 1.0000 1.00
33 LYS N 33 H -38332.41 0.0051 3.0845 -3.0795 1.0000 1.00
59 TYR N 59 H -38353.05 8.6568 8.0602 0.5966 1.0000 1.00
41 GLN N 41 H -38318.91 4.7643 6.6226 -1.8584 1.0000 1.00
61 ILE N 61 H -38276.63 -4.3335 -3.1162 -1.2172 1.0000 1.00
62 GLN N 62 H -38321.78 11.2619 9.8180 1.4439 1.0000 1.00
58 ASP N 58 H -38243.19 3.4617 5.0245 -1.5628 1.0000 1.00
47 GLY N 47 H -38246.38 -3.8925 -5.3995 1.5070 1.0000 1.00
20 SER N 20 H -38332.34 6.5027 2.4449 4.0578 1.0000 1.00
25 ASN N 25 H -38271.15 -0.4308 -1.8399 1.4091 1.0000 1.00
32 ASP N 32 H -38236.77 -2.5950 -4.5886 1.9936 1.0000 1.00
52 ASP N 52 H -38311.95 -3.0258 -0.1218 -2.9040 1.0000 1.00
63 LYS N 63 H -38273.60 -2.1693 1.0943 -3.2636 1.0000 1.00
23 ILE N 23 H -38277.13 -5.2001 -3.8356 -1.3646 1.0000 1.00
12 THR N 12 H -38213.81 -11.2619 -7.8113 -3.4507 1.0000 1.00
30 ILE N 30 H -38341.30 -6.4977 -5.2726 -1.2251 1.0000 1.00
16 GLU N 16 H -38341.04 -1.2975 2.8633 -4.1609 1.0000 1.00
26 VAL N 26 H -38301.08 1.2975 -0.8779 2.1754 1.0000 1.00
29 ALA N 29 H -38277.41 -3.9026 -0.1155 -3.7871 1.0000 1.00
```

Table D.4.: **RDCs captured while under shear at an average rate of 71.94 s^{-1}:** RDCs captured from the N-H bonds of ubiquitin

Amino Acid	Residue Number	J-Coupling + RDC [Hz][±0.05]	RDC [Hz][±0.05]	Amino Acid	Residue Number	J-Coupling + RDC [Hz][±0.05]	RDC [Hz][±0.05]
GLN	2	96.59	3.47	ASP	39	90.53	-4.33
ILE	3	90.10	-3.47	GLN	40	90.10	-3.03
PHE	4	91.39	-2.60	GLN	41	93.13	-1.73
VAL	5	90.53	-2.60	LEU	43	99.19	3.46
LYS	6	94.85	1.30	ILE	44	97.89	5.20
THR	7	97.89	3.47	PHE	45	97.89	4.33
LEU	8	98.76	4.33	GLY	47	94.42	1.30
LYS	11	97.45	3.03	LEU	50	99.62	3.47
THR	12	98.33	5.64	GLU	51	99.62	4.33
ILE	13	92.69	-0.44	ASP	52	94.42	-0.43
THR	14	93.13	-0.43	ARG	54	94.42	-1.30
LEU	15	90.96	-4.33	THR	55	94.42	1.30
GLU	16	94.85	0.86	SER	57	88.36	-5.63
VAL	17	97.02	3.03	ASP	58	93.13	-5.63
GLU	18	96.16	3.03	TYR	59	85.33	-10.40
SER	20	90.53	-2.16	ASN	60	93.56	-0.86
ILE	23	94.43	0.01	ILE	61	95.29	1.73
ASN	25	95.29	0.87	GLN	62	90.53	-3.90
VAL	26	92.26	-0.44	LYS	63	95.29	1.30
LYS	27	100.06	3.04	GLU	64	87.93	-6.06
SER	28	90.96	-5.63	SER	65	92.26	-2.60
ALA	29	98.32	3.03	THR	66	87.50	-4.76
ILE	30	97.02	2.60	LEU	67	89.66	-4.33
ASP	32	97.45	3.03	HIS	68	97.02	1.73
LYS	33	93.56	-0.43	LEU	69	89.66	-3.89
GLU	34	95.73	4.76	VAL	70	97.89	3.46
GLY	35	92.69	-1.30	LEU	71	100.49	3.90

```
11 LYS N 11 H -38261.09 -6.4977 -9.6803 3.1827 1.0000 1.00
```

D.4. Shear at an average rate of 71.94 s^{-1}

Alignment Tensor

$$\begin{bmatrix} -4.39 \times 10^{-5} & 1.90 \times 10^{-5} & 1.11 \times 10^{-4} \\ 1.90 \times 10^{-5} & 7.56 \times 10^{-5} & -1.01 \times 10^{-4} \\ 1.11 \times 10^{-4} & -1.01 \times 10^{-4} & -3.17 \times 10^{-5} \end{bmatrix} \tag{D.4}$$

PALES output file

```
REMARK Molecular Alignment Simulation.
4Hz
REMARK Simulation parameters.
DATA PALES_MODE DC
DATA TENSOR_MODE SVD (Order Matrix Method)
```

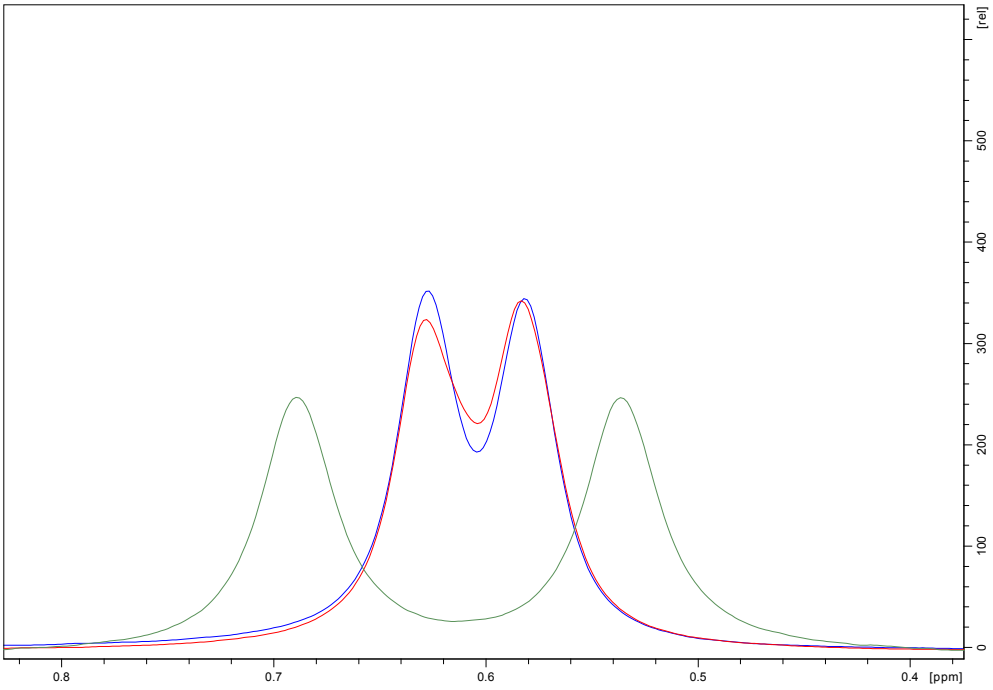

Figure D.4.: **^{2}H spectra while under shear at an average rate of 71.94 s^{-1}:** The blue spectrum was conducted before the IPAP-HSQC. The red spectrum was captured directly after the IPAP-HSQC. The green spectrum was captured before the application of any shear forces and is used to calculate the angle of the liquid crystals director.

```
REMARK Order matrix.
DATA SAUPE_MATRIX S(zz) S(xx-yy) S(xy) S(xz) S(yz)
DATA SAUPE -3.1720e-005 -1.1957e-004 1.9033e-005 1.1115e-004 -1.0095e-004
DATA IRREDUCIBLE_REP A0 A1R A1I A2R A2I
DATA IRREDUCIBLE -5.0286e-005 -1.4387e-004 -1.3067e-004 -7.7390e-005
-2.4637e-005
DATA IRREDUCIBLE GENERAL_MAGNITUDE 3.0210e-004
REMARK Mapping of coordinates.
DATA MAPPING_COOR Szz_d(x) Szz_d(y) Syy_d(x) Syy_d(y) Sxx_d(x) Sxx_d(y)
DATA MAPPING -0.34033 -0.78135 -0.99099 0.63489 0.60537 0.40090
DATA MAPPING INV 1.89008 0.78135 1.53843 -0.63489 -2.28712 -0.40090
REMARK Eigensystem & Euler angles for clockwise rotation about z, y',
z".
DATA EIGENVALUES (Sxx_d,Syy_d,Szz_d) 3.0287e-005 1.4779e-004 -1.7808e-004
DATA EIGENVECTORS (x_coor y_coor z_coor)
DATA EIGENVECTORS X_AXIS 7.2876e-001 5.6268e-001 3.9025e-001
DATA EIGENVECTORS Y_AXIS 2.6848e-001 -7.5906e-001 5.9309e-001
DATA EIGENVECTORS Z_AXIS 6.2994e-001 -3.2744e-001 -7.0424e-001
DATA Q_EULER_SOLUTIONS ALPHA BETA GAMMA
DATA Q_EULER_ANGLES 1 56.66 134.77 207.47
DATA Q_EULER_ANGLES 2 236.66 134.77 207.47
DATA Q_EULER_ANGLES 3 123.34 45.23 27.47
DATA Q_EULER_ANGLES 4 303.34 45.23 27.47
REMARK Euler angles (psi/theta/phi) for rotation about x, y, z.
DATA EULER_SOLUTIONS 2
DATA EULER_ANGLES 24.94 219.05 20.22
DATA EULER_ANGLES 204.94 -39.05 200.22
DATA Da -8.903778e-005
DATA Dr -3.916731e-005
DATA Aa -1.780756e-004
DATA Ar -7.833462e-005
DATA Da_HN -1.921898e+000
DATA Rhombicity 4.398954e-001
REMARK Dipolar couplings.
DATA N 46
DATA RMS 0.999
DATA Chi2 45.940
DATA CORR R 0.941
DATA Q SAUPE 0.217
DATA REGRESSION OFFSET 0.003 +/- 0.143 [Hz]
DATA REGRESSION SLOPE 0.888 +/- 0.048 [Hz]
DATA REGRESSION BAX SLOPE 0.945 +/- 0.034 [Hz]
VARS RESID_I RESNAME_I ATOMNAME_I RESID_J RESNAME_J ATOMNAME_J DI D_OBS
D D_DIFF DD W
FORMAT %4d %4s %4s %4d %4s %4s %9.2f %9.3f %9.3f %9.3f %.2f %.2f
13 ILE N 13 H -38292.09 -0.4359 0.7774 -1.2133 1.0000 1.00
```

```
67 LEU N 67 H -38350.80 -4.3335 -4.9235 0.5901 1.0000 1.00
70 VAL N 70 H -38289.20 3.4566 4.0686 -0.6120 1.0000 1.00
6 LYS N 6 H -38250.54 1.2975 0.0102 1.2873 1.0000 1.00
45 PHE N 45 H -38275.33 4.3335 4.0328 0.3007 1.0000 1.00
43 LEU N 43 H -38260.30 3.4617 4.5738 -1.1121 1.0000 1.00
15 LEU N 15 H -38276.65 -4.3335 -2.7433 -1.5902 1.0000 1.00
50 LEU N 50 H -38335.59 3.4668 3.5656 -0.0988 1.0000 1.00
5 VAL N 5 H -38258.15 -2.6001 -1.3892 -1.2109 1.0000 1.00
44 ILE N 44 H -38288.26 5.2001 3.9968 1.2034 1.0000 1.00
68 HIS N 68 H -38274.68 1.7334 2.1727 -0.4393 1.0000 1.00
8 LEU N 8 H -38323.86 4.3335 3.6707 0.6628 1.0000 1.00
2 GLN N 2 H -38334.96 3.4668 3.0698 0.3969 1.0000 1.00
14 THR N 14 H -38264.76 -0.4308 -0.9444 0.5136 1.0000 1.00
17 VAL N 17 H -38288.70 3.0309 1.3977 1.6332 1.0000 1.00
66 THR N 66 H -38322.75 -4.7643 -4.8170 0.0527 1.0000 1.00
18 GLU N 18 H -38289.89 3.0309 3.6630 -0.6321 1.0000 1.00
4 PHE N 4 H -38267.91 -2.6001 -3.0415 0.4414 1.0000 1.00
27 LYS N 27 H -38307.07 3.0360 3.4680 -0.4320 1.0000 1.00
7 THR N 7 H -38263.76 3.4668 2.5517 0.9151 1.0000 1.00
34 GLU N 34 H -38312.58 4.7643 4.3800 0.3843 1.0000 1.00
39 ASP N 39 H -38347.54 -4.3335 -3.2904 -1.0430 1.0000 1.00
57 SER N 57 H -38257.26 -5.6310 -4.5089 -1.1220 1.0000 1.00
55 THR N 55 H -38280.97 1.2975 0.3990 0.8985 1.0000 1.00
35 GLY N 35 H -38288.68 -1.3026 -0.5539 -0.7487 1.0000 1.00
3 ILE N 3 H -38317.43 -3.4668 -1.7675 -1.6992 1.0000 1.00
60 ASN N 60 H -38339.95 -0.8616 -1.0144 0.1528 1.0000 1.00
40 GLN N 40 H -38334.98 -3.0309 -4.7910 1.7601 1.0000 1.00
65 SER N 65 H -38339.35 -2.6001 -0.3747 -2.2254 1.0000 1.00
33 LYS N 33 H -38332.41 -0.4257 -1.6194 1.1937 1.0000 1.00
41 GLN N 41 H -38318.91 -1.7334 -2.7681 1.0347 1.0000 1.00
61 ILE N 61 H -38276.63 1.7334 1.5551 0.1783 1.0000 1.00
54 ARG N 54 H -38277.99 -1.3026 -1.7822 0.4796 1.0000 1.00
62 GLN N 62 H -38321.78 -3.8976 -4.2506 0.3530 1.0000 1.00
47 GLY N 47 H -38246.38 1.3026 2.0882 -0.7857 1.0000 1.00
20 SER N 20 H -38332.34 -2.1642 -1.9570 -0.2072 1.0000 1.00
25 ASN N 25 H -38271.15 0.8667 1.2742 -0.4075 1.0000 1.00
32 ASP N 32 H -38236.77 3.0309 2.3777 0.6532 1.0000 1.00
52 ASP N 52 H -38311.95 -0.4308 0.1414 -0.5722 1.0000 1.00
63 LYS N 63 H -38273.60 1.2975 0.1525 1.1450 1.0000 1.00
23 ILE N 23 H -38277.13 0.0051 1.2125 -1.2074 1.0000 1.00
30 ILE N 30 H -38341.30 2.6001 1.8325 0.7676 1.0000 1.00
71 LEU N 71 H -38335.76 3.9026 2.0672 1.8355 1.0000 1.00
16 GLU N 16 H -38341.04 0.8616 -0.8452 1.7068 1.0000 1.00
26 VAL N 26 H -38301.08 -0.4359 0.1819 -0.6178 1.0000 1.00
11 LYS N 11 H -38261.09 3.0309 3.8423 -0.8114 1.0000 1.00
```

Bibliography

[1] Sanger, F.; M.L. Anson, K. B.; Edsall, J. T., Eds.; Advances in Protein Chemistry, Vol. 7; Academic Press, 1952; pp 1 – 67.

[2] Pauling, L.; Corey, R. B.; Branson, H. R. *Proceedings of the National Academy of Sciences* **1951**, *37*, 205–211.

[3] Linderstrøm-Lang, K. U. *Lane Medical Lectures: proteins and enzymes*; Stanford University Press, 1952; Vol. 6.

[4] Bragg, W.; James, R.; Bosanquet, C. *Philosophical Magazine Series 6* **1921**, *41*, 309–337.

[5] Bragg, W.; James, R.; Bosanquet, C. *Philosophical Magazine Series 6* **1921**, *42*, 1–17.

[6] Kendrew, J. C.; Bodo, G.; Dintzis, H. M.; Parrish, R.; Wyckoff, H.; Phillips, D. C. *Nature* **1958**, *181*, 662–666.

[7] Fasman, G. *Circular Dichroism and the Conformational Analysis of Biomolecules*; Siberian School of Algebra and Logic; Springer US, 1996.

[8] Saunders, M.; Wishnia, A.; Kirkwood, J. G. *Journal of the American Chemical Society* **1957**, *79*, 3289–3290.

[9] Havel, T. F.; Wüthrich, K. *Journal of molecular biology* **1985**, *182*, 281–294.

[10] Harris, R. K. *Nuclear Magnetic Resonance Spectroscopy*; Longman Scientific and Technical, 1989.

[11] Lepper, C.; Edwards, P.; Schuster, E.; Brown, J.; Dykstra, R.; Callaghan, P.; Williams, M. *Physical Review E* **2010**, *82*, 041712.

[12] Lepper, C.; Edwards, P. J.; Dykstra, R.; Williams, M. A. *Soft Matter* **2011**, *7*, 10291–10298.

[13] Hornak, J. P.; *Basics of NMR.*; 1997. `http://www.cis.rit.edu/htbooks/nmr/nmr-main.htm`.

[14] Gunther, H. *NMR Spectroscopy: Basic Principles, Concepts and Applications in Chemistry*, 3rd ed.; Wiley, 2013.

[15] Levitt, M. H. *Spin Dynamics: Basics of Nuclear Magnetic Resonance*, 2nd ed.; Wiley, 2008.

[16] Macomber, R. S. *A Complete Introduction to Modern NMR Spectroscopy*; Wiley, 1998.

[17] Keeler, J. *Understanding NMR Spectroscopy*, 2nd ed.; Wiley, 2010.

[18] Blake, P. R.; Lee, B.; Summers, M. F.; Adams, M. W.; Park, J.-B.; Zhou, Z. H.; Bax, A. *Journal of Biomolecular NMR* **1992**, *2*, 527–533.

[19] Blake, P. R.; Park, J. B.; Adams, M. W.; Summers, M. F. *Journal of the American Chemical Society* **1992**, *114*, 4931–4933.

[20] Dingley, A. J.; Cordier, F.; Grzesiek, S. *Concepts in Magnetic Resonance* **2001**, *13*, 103–127.

[21] Hahn, E.; Maxwell, D. *Physical Review* **1952**, *88*, 1070.

[22] Minch, M. J. *Concepts in Magnetic Resonance* **1994**, *6*, 41–56.

[23] Karplus, M. *The Journal of Chemical Physics* **1959**, *30*, 11–15.

[24] Karplus, M. *Journal of the American Chemical Society* **1963**, *85*, 2870–2871.

[25] Haasnoot, C.; de Leeuw, F. A.; Altona, C. *Tetrahedron* **1980**, *36*, 2783–2792.

[26] Freeman, R.; Anderson, W. *The Journal of Chemical Physics* **1962**, *37*, 2053–2073.

[27] Anderson, W.; Freeman, R. *The Journal of Chemical Physics* **1962**, *37*, 85–103.

[28] Overhauser, A. W. *Physical Review* **1953**, *92*, 411.

[29] Carver, T.; Slichter, C. *Physical Review* **1953**, *92*, 212.

[30] Friebolin, H. *Basic One- and Two-Dimensional NMR Spectroscopy. 5th Edition*; Wiley-VCH, 2011.

[31] Reich, H. J.; *The Nuclear Overhauser Effect*; 2014. `http://www.chem.wisc.edu/areas/reich/nmr/08-tech-02-noe.htm`.

[32] Keeler, J. *Understanding NMR Spectroscopy*, 2nd ed.; Wiley, 2010.

[33] Harris, R. K.; Becker, E. D.; Cabral de Menezes, S. M.; Goodfellow, R.; Granger, P. *Solid State Nuclear Magnetic Resonance*, *22*, 458 – 483.

[34] Clendinen, C. S.; Lee-McMullen, B.; Williams, C. M.; Stupp, G. S.; Vandenborne, K.; Hahn, D. A.; Walter, G. A.; Edison, A. S. *Analytical Chemistry* **2014**, *86*, 9242–9250.

[35] Morris, G. A.; Freeman, R. *Journal of the American Chemical Society* **1979**, *101*, 760–762.

[36] Martin, G. E.; Zektzer, A. S. *Two dimensional NMR methods for establishing molecular connectivity*, 1988.

[37] Simpson, J. H. *Organic Structure Determination Using 2-D NMR Spectroscopy: A Problem-Based Approach*, 2nd ed.; Academic Press, 2012.

[38] III, A. G. P.; Fairbrother, W. J.; Cavanagha, J.; Skelton, N. J.; Rance;, M. *Protein NMR Spectroscopy: Principles and Practice*, 2nd ed.; Academic Press, 2006.

[39] Bodenhausen, G.; Ruben, D. J. *Chemical Physics Letters* **1980**, *69*, 185–189.

[40] Brunner, E. *Concepts in Magnetic Resonance* **2001**, *13*, 238–259.

[41] Apperley, D. C.; Harris, R. K.; Hidgkinson, P. *Solid State NMR: Basic Principles and Practice*, 1st ed.; Momentum Press, 2012.

[42] Saupe, A.; Englert, G. *Physical Review Letters* **1963**, *11*, 462–464.

[43] Deloche, B.; Samulski, E. T. *Macromolecules* **1981**, *14*, 575–581.

[44] Saupe, A. *Zeitschrift für Naturforschung A* **1964**, *19*, 161–171.

[45] Ottiger, M.; Delaglio, F.; Bax, A. *Journal of Magnetic Resonance* **1998**, *131*, 373 – 378.

[46] Clore, G. M.; Starich, M. R.; Bewley, C. A.; Cai, M.; Kuszewski, J. *Journal of the American Chemical Society* **1999**, *121*, 6513–6514.

[47] Clore, G. M.; Garrett, D. S. *Journal of the American Chemical Society* **1999**, *121*, 9008–9012.

[48] Zweckstetter, M. *Nat. Protoc.* **2008**, *3*, 679–90.

[49] Siebert, H.; Grabowski, D. A.; Schmidt, C. *Rheologica acta* **1997**, *36*, 618–627.

[50] Veron, A.; Gomes, A. E.; Leal, C. R.; Van Der Klink, J.; Martins, A. F. *Molecular Crystals and Liquid Crystals* **1999**, *331*, 499–507.

[51] Chandrasekhar, S. *Liquid Crystals*; Cambridge University Press, 1992.

[52] Meiboom, S.; Hewitt, R. *Physical Review Letters* **1973**, *30*, 261.

[53] Ashton, L.; Dusting, J.; Imomoh, E.; Balabani, S.; Blanch, E. W. *Biophysical journal* **2010**, *98*, 707–714.

[54] Maa, Y.-F.; Hsu, C. C. *Biotechnology and Bioengineering* **1996**, *51*, 458–465.

[55] Kakubayashi, M.; Master's thesis; Massey University; 2008.

[56] Marx, A.; Thiele, C. *Chemistry* **2009**, *15*, 254–60.

[57] Zweckstetter, M.; Bax, A. *Journal of Biomolecular NMR* **2001**, *20*, 365–377.

[58] Prestegard, J.; Bougault, C.; Kishore, A. *Chemical reviews* **2004**, *104*, 3519–3540.

[59] Lipsitz, R. S.; Tjandra, N. *Annual Review of Biophysics and Biomolecular Structure* **2004**, *33*, 387–413.

[60] Kramer, F.; Deshmukh, M. V.; Kessler, H.; Glaser, S. J. *Concepts in Magnetic Resonance* **2004**, *21A*, 10–21.

[61] Blackledge, M. *Progress in Nuclear Magnetic Resonance Spectroscopy* **2005**, *46*, 23–61.

[62] Yan, J.; Delaglio, F.; Kaerner, A.; Kline, A. D.; Mo, H.; Shapiro, M. J.; Smitka, T. A.; Stephenson, G. A.; Zartler, E. R. *J Am Chem Soc* **2004**, *126*, 5008–17; Journal of the American Chemical Society.

[63] Prestegard, J. H.; al Hashimi, H. M.; Tolman, J. R. *Quarterly reviews of biophysics* **2000**, *33*, 371–424.

[64] Ose, V.; *The Electron Microscopy picture of pf1 preparation*; 2015. `http://www.asla-biotech.com/phage.JPG`.

[65] Jaspe, J.; Hagen, S. J. *Biophys J* **2006**, *91*, 3415–24; Biophysical journal.

[66] Hill, E. K.; Krebs, B.; Goodall, D. G.; Howlett, G. J.; Dunstan, D. E. *Biomacromolecules* **2006**, *7*, 10–13; PMID: 16398490.

[67] Edwards, P. J.; Kakubayashi, M.; Dykstra, R.; Pascal, S. M.; Williams, M. A. *Biophysical Journal* **2010**, *98*, 1986 – 1994.

[68] Arnold, L.; Marx, A.; Thiele, C. M.; Reggelin, M. *Chemistry* **2010**, *16*, 10342–6; Chemistry.

[69] Gil, R. R.; Gayathri, C.; Tsarevsky, N. V.; Matyjaszewski, K. *The Journal of Organic Chemistry* **2008**, *73*, 840–848.

[70] Kummerlowe, G.; Luy, B. *Trends in Analytical Chemistry* **2009**, *28*, 483–493.

[71] Mangoni, A.; Esposito, V.; Randazzo, A. *Chemical Communications* **2003**, 154–155.

[72] Thiele, C. M. *European Journal of Organic Chemistry* **2008**, *2008*, 5673–5685.

[73] Schuetz, A.; Murakami, T.; Takada, N.; Junker, J.; Hashimoto, M.; Griesinger, C. *Angewandte Chemie* **2008**, *120*, 2062–2064.

[74] Fehér, K.; Berger, S.; Kövér, K. E. *Journal of Magnetic Resonance* **2003**, *163*, 340–346.

[75] Marx, A.; Schmidts, V.; Thiele, C. M. *Magnetic Resonance in Chemistry* **2009**, *47*, 734–40.

[76] Pascal, S. M. *NMR Primer: An HSQC-Based Approach*; IM Publications, 2008.

[77] Scuseria, G.; Robb, M.; Cheeseman, J.; Scalmani, G.; Barone, V.; Mennucci, B.; Petersson, G.; Nakatsuji, H.; Caricato, M.; Li, X.; et al. *Gaussian Inc, Wallingford CT.* **2009**.

[78] Navarro-Vázquez, A. *Magnetic Resonance in Chemistry* **2012**, *50*, S73–S79.

[79] Goldstein, G.; Scheid, M.; Hammerling, U.; Schlesinger, D.; Niall, H.; Boyse, E. *Proceedings of the National Academy of Sciences* **1975**, *72*, 11–15.

[80] Finley, D.; Varshavsky, A. *Trends in Biochemical Sciences* **1985**, *10*, 343–347.

[81] Jentsch, S. *Annual Review of Genetics* **1992**, *26*, 179–207.

[82] Hochstrasser, M. *Annual Review of Genetics* **1996**, *30*, 405–439.

[83] Hershko, A.; Ciechanover, A.; Heller, H.; Haas, A. L.; Rose, I. A. *Proceedings of the National Academy of Sciences* **1980**, *77*, 1783–1786.

[84] Vijay-Kumar, S.; Bugg, C. E.; Cook, W. J. *J Mol Biol* **1987**, *194*, 531–544.

[85] Di Stefano, D. L.; Wand, A. J. *Biochemistry* **1987**, *26*, 7272–7281.

[86] Cornilescu, G.; Marquardt, J. L.; Ottiger, M.; Bax, A. *Journal of the American Chemical Society* **1998**, *120*, 6836–6837.

[87] Lange, O. F.; Lakomek, N.-A.; Farés, C.; Schröder, G. F.; Walter, K. F. A.; Becker, S.; Meiler, J.; Grubmüller, H.; Griesinger, C.; de Groot, B. L. *Science (New York, N.Y.)* **2008**, *320*, 1471–5.

[88] Huang, J.-r.; Grzesiek, S. *Journal of the American Chemical Society* **2009**, *132*, 694–705.

[89] Lakomek, N.-A.; Lange, O.; Walter, K.; Fares, C.; Egger, D.; Lunkenheimer, P.; Meiler, J.; Grubmüller, H.; Becker, S.; de Groot, B. L.; et al. *Biochemical Society Transactions* **2008**, *36*, 1433–1437.

[90] Wlodarski, T.; Zagrovic, B. *Proceedings of the National Academy of Sciences* **2009**, *106*, 19346–19351.

[91] Montalvao, R. W.; De Simone, A.; Vendruscolo, M. *Journal of Biomolecular NMR* **2012**, *53*, 281–292.

[92] Brünger, A. T.; Adams, P. D.; Clore, G. M.; DeLano, W. L.; Gros, P.; Grosse-Kunstleve, R. W.; Jiang, J.-S.; Kuszewski, J.; Nilges, M.; Pannu, N. S.; et al. *Acta Crystallographica Section D: Biological Crystallography* **1998**, *54*, 905–921.

[93] PyMOL: The PyMOL Molecular Graphics System, Version 1.7.4.4 Edu, Schrödinger, LLC.